



In silico analysis of carbon stabilisation by plant and soil microbes for different weather scenarios

Mona Giraud^{*,1,2}, Ahmet Kürşad Sircan^{*,3}, Thilo Streck³, Daniel Leitner¹, Guillaume Lobet⁴, Holger Pagel^{*,1,2}, and Andrea Schnepf^{*,1,2}

*These authors contributed equally to this work

¹Institute of Bio- and Geosciences (IBG-3), Forschungszentrum Jülich, 52428, Jülich, Germany

²Institute of Crop Science and Resource Conservation, University of Bonn, 53115 Bonn, Germany

³University of Hohenheim, Institute of Soil Science and Land Evaluation, Department of Biogeophysics, Germany

⁴Earth and Life Institute, Université catholique de Louvain, Belgium

Correspondence: Mona Giraud (m.giraud@fz-juelich.de)

Abstract. A plant's development is strongly linked to the water and carbon (C) flows in the soil-plant-atmosphere continuum. Ongoing climate shifts will alter the water and C cycles and affect plant phenotypes. Comprehensive models that simulate mechanistically and dynamically the feedback loops between water and C fluxes in the soil-plant system are useful tools to evaluate the sustainability of genotype-environment-management combinations that do not yet exist. In this study, we present the equations and implementation of a rhizosphere-soil model within the CPlantBox framework, a functional-structural plant model that represents plant processes and plant-soil interactions. The multi-scale plant-rhizosphere-soil coupling scheme previously used for CPlantBox was likewise updated, among others to include an implicit time-stepping. The model was implemented to simulate the effect of dry spells occurring at different plant development stages, and for different soil biokinetic parametrisations of microbial dynamics in soil. We could observe diverging results according to the date of occurrence of the dry spells and soil parametrisations. For instance, an earlier dry spell led to a lower cumulative plant C release, while later dry spells led to higher C input to the soil. For more reactive microbial communities, this higher C input caused a strong increase in CO₂ emissions, while, for the same weather scenario, we observed a lasting stabilisation of soil C with less reactive communities. This model can be used to gain insight into C and water flows at the plant scale, and the influence of soil-plant interactions on C cycling in soil.

1 Introduction

Understanding the dynamics driving the water and carbon (C) balances in the soil-plant-atmosphere continuum is key to predict, mitigate, and adapt agroecosystems to climate change (Silva and Lambers, 2021; George et al., 2024). While water plays an important role as a resource and as an intra- and inter-domain signalling carrier (De Swaef et al., 2022), C compounds can serve as an essential energy source or a biomass building block (Lynch et al., 2021; George et al., 2024).



Plants link the water and C balances in the soil and atmosphere via plant-related processes, such as coupled stomatal regulation-photosynthesis-transpiration, C and water transport and storage in plant tissues, C usage (growth, maintenance, exudation) root-soil water exchanges and root C release (De Swaef et al., 2022; Lacoïnte and Minchin, 2019; Silva and Lambers, 2021). The plant's capacity to capture, transport and release water (resp. C) across domains (e.g., C fixation leading to rhizodeposit hotspots distribution (Landl et al., 2021a)) or within one domain (e.g., hydraulic lift, (Lynch et al., 2021)) is also strongly defined by the topology of its shoot (de la Fuente Cantó et al., 2020) and root system (Galindo-Castañeda et al., 2023; George et al., 2024; de la Fuente Cantó et al., 2020)—e.g., lateral root branching density, number of root tips (Lynch, 2021; Galindo-Castañeda et al., 2023). Likewise, plant anatomical characteristics (e.g., number and nature of the concentric root cells, number and size of the phloem and xylem vessels) strongly affect the flow within the plant (Lynch et al., 2021) and the plant-soil exchanges (Galindo-Castañeda et al., 2023; Lynch et al., 2021).

The quantity and quality of the C released by the plant influence the transfer of nutrients and energy to the soil (de la Fuente Cantó et al., 2020) and thus microbial activity (Schnepf et al., 2022; Galindo-Castañeda et al., 2023, 2022; de la Fuente Cantó et al., 2020) directly as energy and biomass input and indirectly by changing the properties of the soil (Schnepf et al., 2022; de la Fuente Cantó et al., 2020; George et al., 2024). Root water uptake changes the soil moisture (Ruiz et al., 2021), which eventually triggers drought stress responses of soil microbial communities (Bardgett and Caruso, 2020). Plant-soil feedbacks drive inter and intra-specific plant interactions (Putten et al., 2013) (e.g., competition for soil resources). Plants can also exert direct feedback effects on themselves (e.g., aboveground-belowground feedback) which will influence their fitness. Those feedbacks depend on soil organic matter (SOM) content and texture, which determine soil water holding capacity and hence moisture availability under drought (Bardgett and Caruso, 2020; George et al., 2024).

Plant-soil exchanges lead to the creation of the rhizosphere, an area of soil around the root with biotic (rhizodeposition, microbial communities) and abiotic (structure, water content) characteristics distinctive from the bulk soil (George et al., 2024; de la Fuente Cantó et al., 2020). The hydraulic conductance of the rhizosphere is the primary constraint for plant water transport, especially in water-limited environments (De Swaef et al., 2022; Khare et al., 2022; Roose et al., 2016), leading to abiotic stress and stomatal closure (George et al., 2024; Damour et al., 2010) or better drought resilience in case of favorable abiotic conditions (Lynch et al., 2021).

The rhizosphere is also the most important hotspot of microbial activity on the planet (George et al., 2024; Lynch et al., 2021). Soil microbes control SOM decomposition and CO₂ release (Pagel et al., 2020) and regulate soil C allocation to the different organic and mineral pools. Rhizosphere microbes are relevant to soil C cycling as the activation-deactivation processes allow for rapid responses to the input of C and energy provided by rhizodeposits (George et al., 2024). Soil microbes are therefore a significant sink of photoassimilates, influencing root C release, root-to-shoot C allocation and overall plant growth (Lynch et al., 2021).



55 Due to the tight coupling of water and C cycling between soil, microbes and plant, it becomes relevant to design integrated
plant-microbiome traits adapted for specific soils to promote resource capture by plants and ensure the resilience of plant-soil
systems to environmental stressors (Galindo-Castañeda et al., 2022; de la Fuente Cantó et al., 2020; Silva and Lambers, 2021).
A thorough understanding of interactions between soil-microbes-plant (Galindo-Castañeda et al., 2022; Bardgett et al., 2013;
Roose et al., 2016; George et al., 2024; Gaudio et al., 2021) that can lead to intra- and inter-specific competition (for light,
60 water and nutrients), complementarity (spatio-temporal and niche processes) and facilitation (improving access to resources)
is therefore essential to inform breeding choices (De Swaef et al., 2022; Gaudio et al., 2021).

Mechanistic biogeochemical modelling facilitates the analysis of complex systems (Schnepf et al., 2022; Putten et al., 2013).
Especially Functional Structural Plant Models (FSPMs) link the plant structure with its function and simulate processes at the
65 plant level (Schnepf et al., 2022; Ruiz et al., 2021). Coupling an FSPM with a soil model in a multiscale modelling framework
leverages the strengths of different models and increase model accuracy (Schnepf et al., 2022; Roose et al., 2016; Gaudio
et al., 2021). Small-scale models provide effective properties and predict emerging behaviour at higher scales, while models at
coarser scales provide the initial and boundary conditions to the small scale models (Schnepf et al., 2022).

70 Although many studies looked at water and flow of (usually one) nutrient (especially phosphorus) in soil and rhizosphere
(Mai et al., 2019; Ruiz et al., 2021; Roose et al., 2016), few focused on both water and C (Ruiz et al., 2021) and accounted for
physiochemical processes (Pot et al., 2022). Moreover, many of the spatially explicit rhizosphere models ignore microorganisms
(Roose et al., 2016) although the increasing resolution of those models make a detailed characterisation of the soil biochemistry
more relevant (Roose et al., 2016; Lynch et al., 2021). FSPMs simulating C (Rees et al., 2020, 2023) and water flow were also
75 developed (Lacointe and Minchin, 2019; Giraud et al., 2023) but simulating neither the soil C nor water flows (Lacointe and
Minchin, 2019; Rees et al., 2020, 2023) or only the water flow (Giraud et al., 2023).

This study aimed to set up and implement a fully integrated plant-soil-microbiome model that accounts for root-microbiome
interactions directly and enables the in-depth analysis of drought responses of C cycling in plant-soil systems. We present
an extended version of the FSPM CPlantBox (Giraud et al., 2023). CPlantBox is a 3D functional structural full plant model
80 and was used to model several processes across the plant, single root, and pore scales (Mai et al., 2019; Landl et al., 2021a;
Giraud et al., 2023). Root system simulations were also implemented to evaluate the effect of root system structure on the
root-soil exchange of water (Khare et al., 2022), C (Landl et al., 2021a), or water and phosphorous (Mai et al., 2019). We
coupled CPlantBox with TraiRhizo (Sircan et al., 2025), a 1D axisymmetric soil model based. TraiRhizo offers a unique
balance between complexity and precision for the C and microbial dynamic and a simplified representation of the soil structure
85 (see review of Pot et al. (2022) for an evaluation of the analogous SpatC (Pagel et al., 2020) against other soil models). For this
study, TraiRhizo was adapted and re-implemented in DuMu^x (Koch et al., 2021) for a faster and more adaptable simulation
setup. The two models were coupled using an updated version of the multiscale setup of Mai et al. (2019) to obtain higher
accuracy and stability.



In the first part of the paper, we present the equations of the model, with emphasis on the soil processes. We then present the
90 scheme for the coupling of the different domains and modules. In the second section of the paper, we implement the model to
evaluate how short dry spells at different stages of the plant's development affect the soil C balance and, in particular, the C
stabilisation according to the biokinetic characteristics of the microbial community. In the last section of the paper, we discuss
the output of the coupled model against experimental and *in silico* results, and we compare our framework against other existing
simulation tools.

95 2 Material and methods

2.1 Overview of the multiscale framework

2.1.1 Individual models

For the plant domain, we use the FSPM CPlantBox, as presented by Giraud et al. (2023). In CPlantBox, the plant is represented
as a series of connected 1-dimensional segments, making a branched network of nodes in a 3-dimensional space (Fig. 1(a)).
100 CPlantBox simulates the plant water flow using the analytical solution of (Meunier et al., 2017), and the coupled the stomatal
regulation (Leuning, 1995) and FvCB-photosynthesis (Farquhar et al., 1980) models. The plant C balance is evaluated with a
numerical solver (Lacointe and Minchin, 2019), which yields the semi-mechanistic plant growth rate.

For the soil domain, Sircan et al. (2025) developed a 1-dimensional axisymmetric soil model that computes the C transport and
microbial dynamics according to a set C release rate from a root segment. Their model was re-implemented within the existing
105 soil framework of the FSPM (Mai et al., 2019) and adapted to take into account variations of water content. It was expanded
to represent the 3-dimensional macroscale (Fig. 2) (Khare et al., 2022; Mai et al., 2019; Koch et al., 2021). The macroscale
model is made of 3-dimensional sub-control volumes (i.e., voxels), while the microscale model is comprised of axisymmetric
1D sub-control volumes (i.e., segments). A list of the symbols of the soil models, their units and meanings can be found in
appendix A. The explicitly represented soil C pools are: low molecular weight organic compounds (dissolved and sorbed),
110 high molecular weight organic compounds, copiotrophic and oligotrophic microorganisms with active and dormant metabolic
states, emitted CO₂ due to microbial respiration. In the following section, we give an overview of the spatial and temporal
coupling of these models within a multiscale framework.

The hydraulic conductance of the soil-root interface is the primary constraint for plant water transport when the soil is dry.
Achieving realistic results requires, therefore, high spatial resolution near the soil-root interface, leading to computationally
115 expensive simulations (Roose et al., 2016; Khare et al., 2022). To balance computing speed and model accuracy, we therefore
coupled the models presented in this section in a multiscale framework where the spatial resolution is set according to the
distance from the soil-root interface.



2.1.2 Spatial coupling

Figs. 1 and 2 give a graphical representation of the spatial coupling method, adapted from the approach presented by Mai et al. (2019) and Khare et al. (2022). Each root segment below-ground is allocated to a macroscale voxel, selected according to the location of the segment centre when it was first created. For each root segment, we initialise a microscale model that computes the water flow, C transport, and microbial dynamics based on the plant-soil water and C exchanges prescribed by the root segment. Other than in Sircan et al. (2025), in which the plant-soil exchange was prescribed as boundary conditions at the root-soil interface, the net releases of water and C in this coupled model come from the simulation outputs of the FSPM, driven by inner plant flows and processes, such as photosynthesis, transpiration, and growth (Giraud et al., 2023). The volume of the macroscale voxel is divided between the microscale domains it contains. Therefore, the maximum possible volume of a single microscale domain is the volume of the containing voxel. The total perirhizal volume around a root system (bulk soil) corresponds to the total volume of all the microscale domains. It is also equal to the sum of the volumes of all macroscale voxels containing at least one root segment. Therefore, the bulk soil volume depends on the root system structure and on the user-defined resolution at the macroscale rather than an *a priori* evaluation of the rhizosphere volume. The microbial reactions and adsorption are computed at the voxel scale for voxels that do not contain root segments. The biochemical reactions are computed at the microscale for voxels containing at least one segment. The resulting variation rates are represented at the macroscale as a sink term. The flow of water and transport of solutes between the voxels is computed at the macroscale and given as sink term to the microscale segments. Moreover, we scale the size of the microscale segments, meaning that the segments near the root surface are smaller than the ones further away. The macroscale domain is divided into subdomains whose concentrations and flows are computed in parallel while the microscale domains are distributed between processes run in parallel. The plant processes are not simulated in parallel.

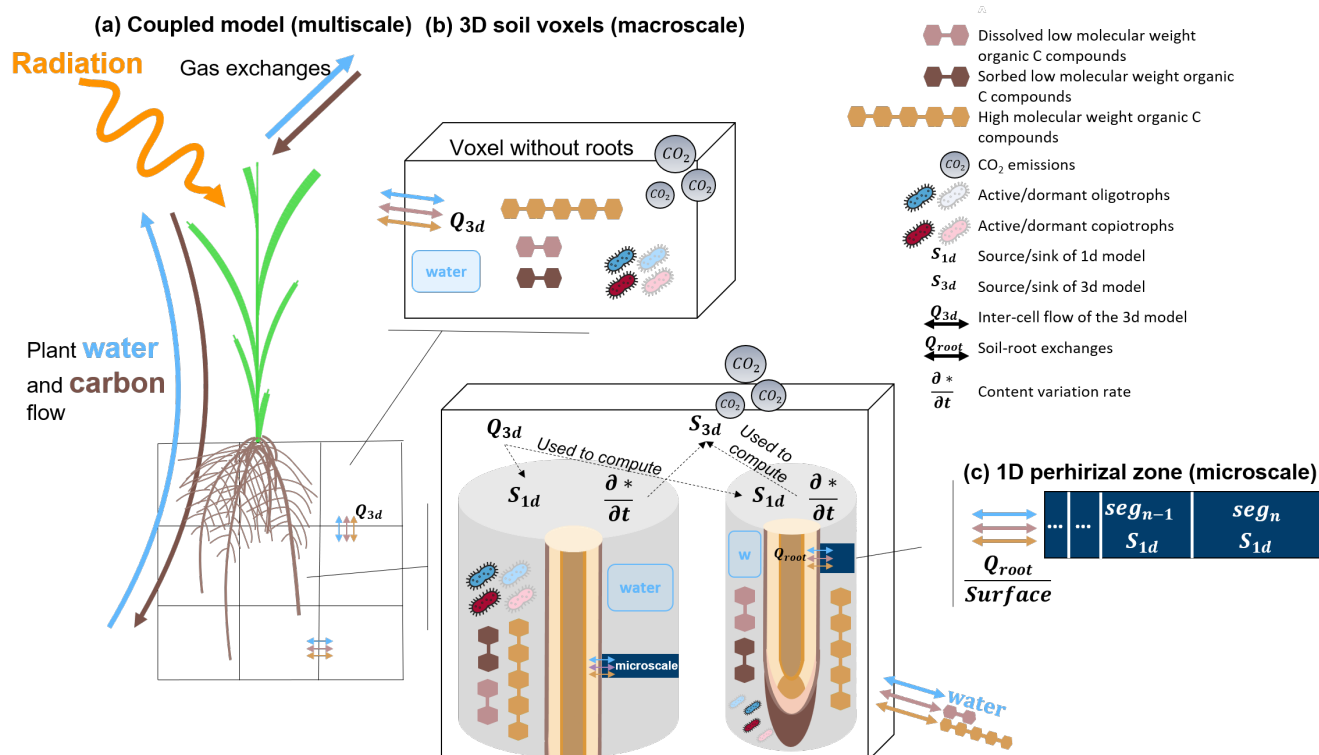


Figure 1. Representation of the multiscale coupling with (a) the whole multiscale model, (b) example of 3D macroscale soil voxels, (c) example of a 1D microscale model. The 3D soil model (black grid) is made up of 3D voxels (transparent rectangles with black borders). The 1D model is represented using the dark blue line in the 3D voxels. It lies between a root segment and the end of the implicitly-represented perirhizal zone (grey hollow cylinder).

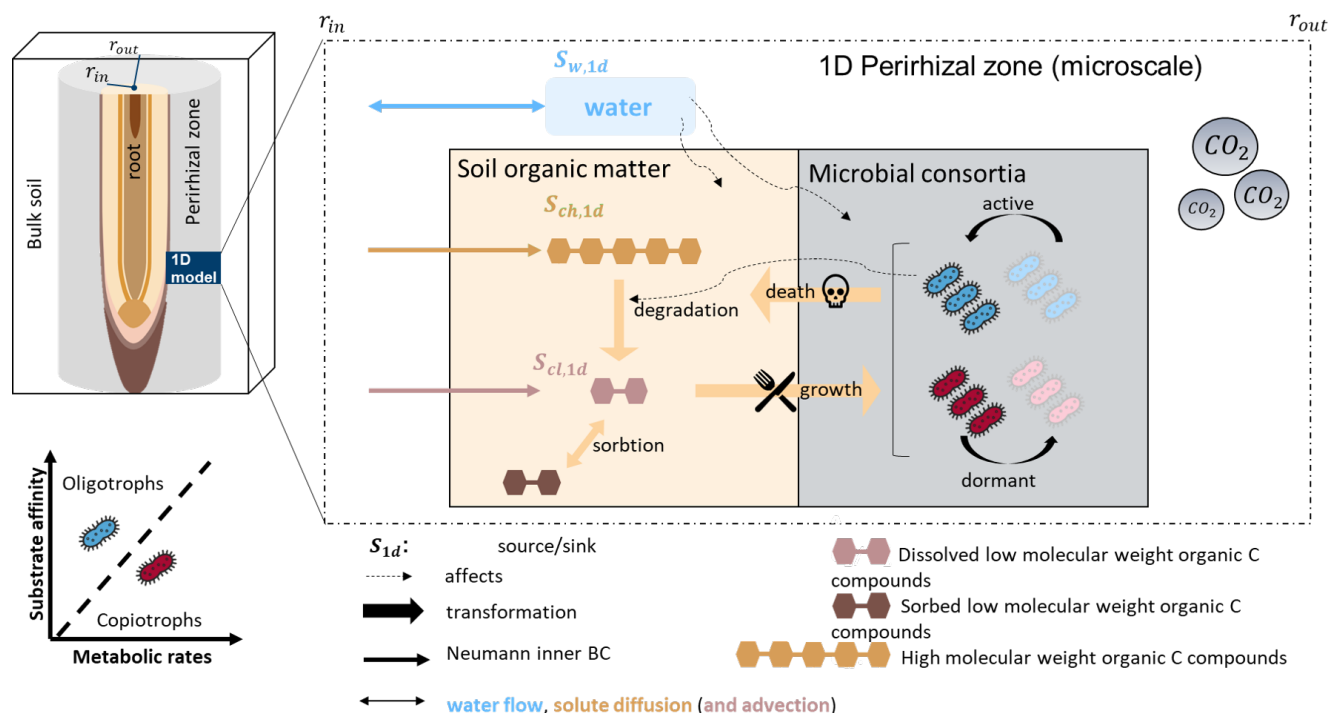


Figure 2. Representation of the updated microscale model (Sircan et al., 2025) reimplemented within the multiscale framework (Mai et al., 2019; Koch et al., 2021). The model represents the soil domain around the root (perirhizal zone). Eight carbon pools are represented: carbon from organic compounds with a low molecular weight (dissolved and sorbed), organic compounds with a high molecular weight, active and dormant copiotrophs and oligotrophs, emitted microbial CO_2 . Water flow and content are also represented. The graphic was adapted from Sircan et al. (2025).

Fig. 3 gives a representation of the hard-coded direct interactions between the atmospheric conditions and the C and water pools represented in the plant and soil. For instance, for a set soil water content, high transpiration leads to a lower plant water potential and, thus, to a lower growth. In contrast, growth leads to a larger root system and leaf surface, allowing for higher transpiration. It is the interactions between those processes that drive the water and C balances of the overall system.

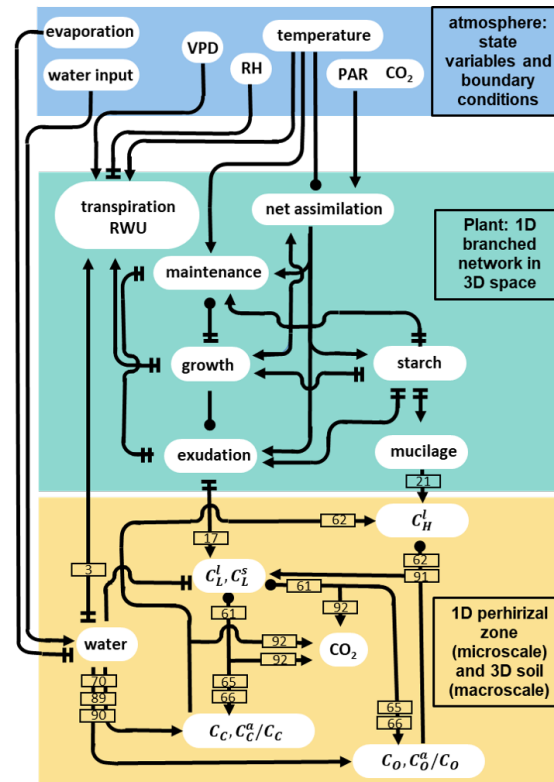


Figure 3. Graphical representation of the direct interactions represented between the different carbon and water pools plant model (green rectangle), soil models (yellow rectangle) and the atmospheric conditions given as input (blue rectangle). The lines ending with an arrow represent a positive effect, two perpendicular lines represent a negative effect, and a circle represents both a positive and negative effect (the net effect depends on the simulated conditions). The numbers in the rectangles give the indexes of the equations describing the corresponding process. The equations affecting the plant domain are defined in Giraud et al. (2023). The atmospheric conditions are represented by user-defined state variables and boundary conditions, e.g. vapour pressure deficit (VPD), relative humidity (RH), and incoming photosynthetically active radiations (PAR). Soil carbon pool data include the concentration of carbon from low molecular weight organic compounds in the soil and water phase (resp. C_L^s , C_L^l), high molecular weight organic compounds in the water phase (C_H^l), total or active copiotrophs (resp. C_C , C_C^a) and oligotrophs (resp. C_O , C_O^a).

2.1.3 Temporal coupling

The modules of the plant and soil models are implemented sequentially. The order of the implementation is presented in Fig. 4. Each "outer" loop (encompassing all the modules) represents one time-step. Within each time step, two nested fixed-point iterations are implemented:

1. the "first fixed point iteration" contains the interactions between the [a] soil water flow and solute transport (for the microscale and macroscale domains) and [b] plant water flow and stomatal regulation.



2. the "second (inner) fixed point iteration" links the steady state plant water flow and stomatal regulation. This iteration loop was presented in Giraud et al. (2023) and will not be detailed further here.

150

These two nested iteration loops allow for a higher computing speed. Indeed, the inner fixed point iteration for the stomatal opening can necessitate several hundred iterations before convergence (especially in the case of water-induced stomatal closing). While the FcVB-stomatal regulation module can compute these iterations quickly, the code section evaluating the water flow at the macro- and microscale is much slower. Moreover, in the first iterations of the FcVB-stomatal computation, strong over- or under-estimation of the transpiration may occur, especially in case of sharp changes in environmental conditions. Using these inputs directly for soil flow computation could lead to non-convergence errors. Processes in the C and water cycles can operate on different timescales (Gaudio et al., 2021). Specifically, the speed of plant growth and phloem transport tends to be slower than the plant and soil water flow. When running a simulation, it may consequently be necessary to use a smaller time step within the fixed-point iteration. Thus, we set up an adaptive operator splitting between the outer time step and the first fixed-point iteration, with an automatic adaptation of the fixed-point iteration time step. Moreover, we used an implicit time stepping within the fixed-point iteration, which means that the output of the previous loop is used as initial and boundary conditions for the next loop of the iteration. This implicit time stepping is more stable than the explicit alternative and allows us to use larger time steps. Currently, the plant sucrose flow and growth are outside the iteration loop. Indeed, adding these modules to the fixed-point iteration would significantly slow the simulation. Also, for time steps $< 1 h$, changes in plant shape and sucrose transport remain limited.

165

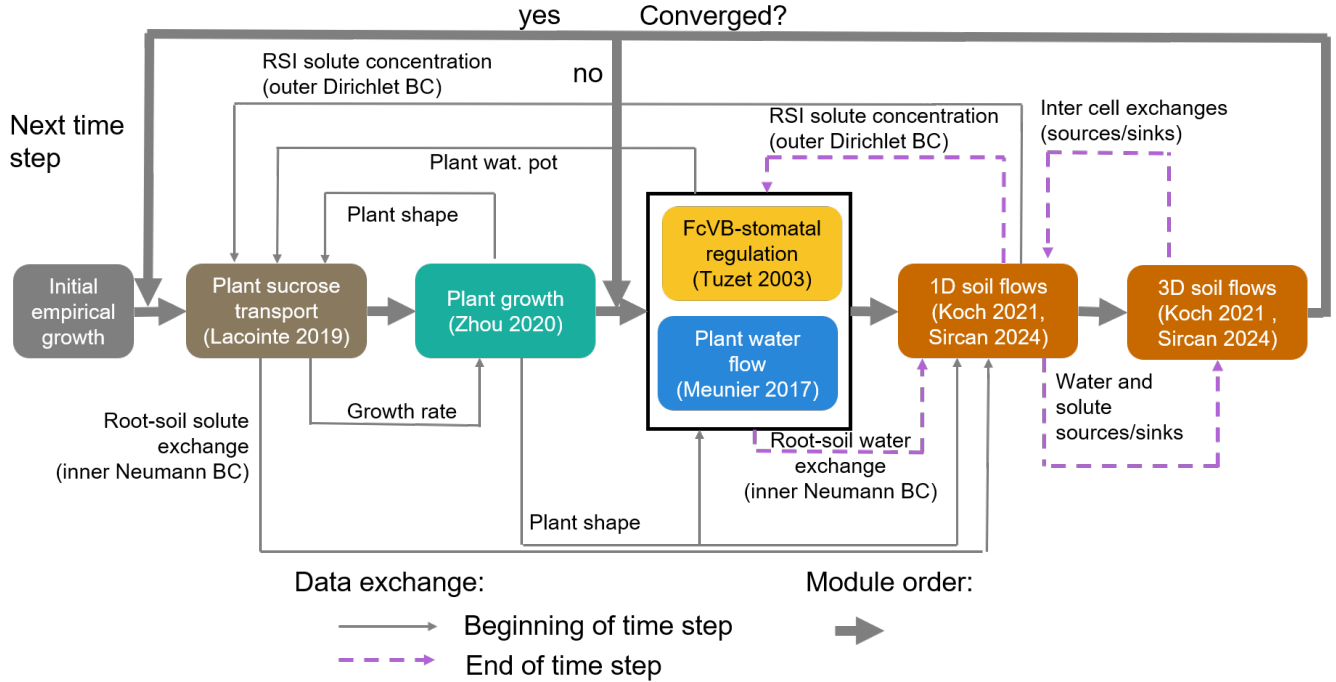


Figure 4. Representation of the time loop, as well as the implementation order and exchange of data between the modules. The loop including the soil flows (orange rectangles) corresponds to the outer iteration loop. The black rectangle outline containing the plant water flow (blue rectangle) and stomatal regulation (yellow rectangle) corresponds to the inner iteration loop. The plant sucrose transport and balance (brown rectangle) and growth (green rectangle) are not included in the iteration loop. Adapted from Giraud et al. (2023).

2.2 Governing Equations

These sections present the method used to simulate water and carbon turnover within the plant and the soil. Each section is divided between the plant-specific and soil-specific equations. For the soil part, the common equations for both the macro- and microscale are presented, followed by equations specific to each domain. The soil volume (volume of the solid and pores) is written in $cm^3\ scv$ (sub-control volume). The amounts of solutes and microbes are given in units of equivalent carbon ($mol\ C$). As the equations describing the microbial reactions remain similar to those set up by Sircan et al. (2025), these ordinary differential equations are included in appendix D.

2.2.1 Plant water flow

The plant water model is described in Giraud et al. (2023). Briefly, we compute the plant xylem water flow as:

$$-K_{ax,x} \frac{\partial^2 \psi_{h,x}}{\partial^2 \xi} = -p_{seg} \times q_{w,plant-out} \text{ for } \Omega \setminus \partial\Omega, \quad (1)$$

$$\frac{\partial \psi_{h,x}}{\partial \xi} = 0 \text{ for } \partial\Omega \text{ (all organ end-nodes)} \quad (2)$$



$K_{ax,x}$ ($cm^4 hPa^{-1} d^{-1}$) is the xylem intrinsic axial conductance and ξ (cm) is the local axial coordinate of the plant. p_{seg} (cm) is the perimeter of the plant exchange zone, Ω the domain considered (here the plant), and $\partial\Omega$, the domain's boundary (here: the tip or end-node of each organ). We assume a no-flux boundary condition here as the plant-exterior water exchanges occur along the segments.

The net water sink is given by the lateral water flow ($q_{w,plant-out}$ in $cm d^{-1}$), which corresponds to the xylem-soil ($q_{w,root-soil}$) or xylem-atmosphere ($q_{w,leaf-air}$) water exchange:

$$q_{w,plant-out} = \begin{cases} q_{w,root-soil} = \min(K_{lat,x}, K_{sri})(\psi_{h,x} - \psi_{m,1DS}) & , \text{ if root} \\ q_{w,leaf-air} = K_{lat,min}(\psi_{h,x} - \psi_{h,ox}) & , \text{ if leaf blade} \end{cases} \quad (3)$$

With $K_{lat,x}$ ($cm hPa^{-1} d^{-1}$) the lateral hydraulic conductivity of the root cortex (for roots) or of the vascular bundle-sheath (for leaves). K_{sri} ($cm hPa^{-1} d^{-1}$) is the equivalent lateral hydraulic conductivity and $\psi_{m,1DS}$ (hPa) is the soil matric potential at the inner boundary of the corresponding 1D microscale soil domain (root-soil interface). $\psi_{h,ox}$ (hPa) is the water potential in the outer-xylem compartment, computed by the FvCB-stomatal regulation module. Note that, as changes in plant water storage are neglected, root water uptake equals transpiration at any given time step: $\sum_i^{segs} p_i q_{w,root-soil,i} = \sum_i^{nr} p_i q_{w,leaf-air,i}$, with p_i (cm) the perimeter of the segment i within the set $segs$.

K_{sri} is computed from the soil and plant data:

$$K_{sri} = \begin{cases} \frac{K_{sat} \kappa_m(S_{sat})}{\Delta r_{root-1DS}} & \text{if } q_{w,root-soil} \leq 0 \\ \frac{K_{sat}}{\Delta r_{root-1DS}} & \text{else} \end{cases}, \quad (4)$$

$$K_{sat} = \frac{\kappa}{\mu_w} \quad (5)$$

With K_{sat} ($cm hPa^{-1} d^{-1}$) the soil saturated hydraulic conductivity, μ_w ($hPa d$) the viscosity of the soil water solution, assumed equal to that of pure water at $20^\circ C$. κ (cm^2) is the intrinsic permeability of the soil and κ_m ($-$) the relative conductivity loss, dependent on the soil water saturation (S_{sat} , $-$). $\Delta r_{root-1DS}$ (cm) is the distance in radial coordinate between the root surface and the centre of the inner segment of the microscale domain. Net root water release ($q_{w,root-soil} > 0$) is only limited by K_{sat} in the soil, while net root water uptake ($q_{w,root-soil} < 0$) is also limited by κ_m .

2.2.2 Soil water flow

The variation in volumetric soil water content (θ in $cm^3 water/cm^3 scv$) is defined according to the Richards equations (Richards, 1931):

$$\frac{\partial \theta}{\partial t} = \nabla \cdot (K(S_{sat})(\nabla \psi_{m,XDS} - \nabla \psi_{g,XDS})) + S_\theta \quad (6)$$

With $K(S_{sat})$ ($cm^2 hPa^{-1} d^{-1}$) the unsaturated hydraulic conductivity (hereafter written as K for simplicity), $\nabla \psi_{m,XDS}$ and $\nabla \psi_{g,XDS}$ (hPa/cm) are the gradients of matric and gravitational water potentials in either the macroscale (ψ_{3DS}) or microscale (ψ_{1DS}) domain, respectively.



S_θ (cm^3 water cm^{-3} scv d^{-1}) is the net source of water in the domain. ∇ is the nabla operator, either for the 1D axisymmetric (radial derivative $\frac{\partial}{\partial r}$) or for the 3D domain ($\frac{\partial}{\partial x} + \frac{\partial}{\partial y} + \frac{\partial}{\partial z}$). We moreover have:

$$\theta = \phi S_{sat} \quad (7)$$

with ϕ (cm^3 pore/ cm^3 scv) the soil porosity (assumed constant). for simplicity, we assume that $\phi = \theta_s$, with θ_s (cm^3 water/ cm^3 scv) the θ value at saturation. θ_r (cm^3 water/ cm^3 scv) is the lowest possible θ value (residual water content). The hydraulic conductivity is defined using the pore size distribution model of Mualem (1976) and the water retention function is computed according to van Genuchten (1980):

$$S_{sat} = \left(\frac{1}{1 + (\alpha \psi_{c,XDS})^n} \right)^{1-1/n} \quad (8)$$

$$\psi_{c,XDS} = \psi_{n,XDS} - \psi_{m,XDS} \quad (9)$$

$$K = \kappa_m(S_{sat})K_{sat} \quad (10)$$

$$\kappa_m(S_{sat}) = S_{sat}^{l_{soil}} \times [1 - (1 - (S_{sat})^{n/(n-1)})^{1-1/n}]^2 \quad (11)$$

ψ_n (hPa) is the reference pressure, set to 1000 hPa, and ψ_c (hPa) is the capillary pressure. α (cm^{-1}) is related to the inverse of the air entry suction, n (–) is a shape parameter, l_{soil} (–) is the soil tortuosity. The implementation of Eq. (6) for the macroscale 3D soil and microscale 1D soil are given respectively in appendices B1 and B2.

2.2.3 Plant carbon transport

The plant sucrose model used for this study is based on the one presented by Giraud et al. (2023). The model was adapted to simulate mucilage release. The variation of sucrose-carbon concentration in the sieve tube (C_L^{st} in $mol C cm^{-3} st d^{-1}$, with cm^3 st the sieve tube volume) is computed from Eq. (12):

$$\begin{aligned} \frac{\partial C_L^{st}}{\partial t} + \frac{\partial}{\partial \xi} \left(C_L^{st} \times K_{ax,st} (RT_{seg} \frac{\partial C_L^{st}}{\partial \xi} + \frac{\partial \psi_{h,x}}{\partial \xi} + \frac{\partial \psi_{g,x}}{\partial \xi}) \right) \\ - S_{exud,st} - S_{starch,st} - S_{other,st} = 0 \\ \text{for } \Omega \setminus \partial\Omega, t > t_0, \end{aligned} \quad (12)$$

$$K_{ax,st} (RT_{seg} \frac{\partial C_L^{st}}{\partial \xi} + \frac{\partial \psi_{h,x}}{\partial \xi} + \frac{\partial \psi_{g,x}}{\partial \xi}) = 0 \quad \text{for } \partial\Omega \quad (13)$$

$$C_L^{st} = C_{L,0}^{st} \quad \text{for } t = t_0, \quad (14)$$

With R ($hPa cm^3 K^{-1} mol^{-1}$) the ideal gas constant, $K_{ax,st}$ ($cm^4 hPa^{-1} d^{-1}$) the sieve tube axial intrinsic conductance, T_{seg} (K) the temperature of the plant segment. $S_{exud,st}$ ($mol cm^{-3} st d^{-1}$) is the loss of C_L^{st} by exudation of low molecular weight organic carbon compounds, S_{starch} ($mol cm^{-3} st d^{-1}$) is the loss or gain of C_L^{st} by starch synthesis or degradation, $S_{other,st}$ ($mol cm^{-3} st d^{-1}$) represents other net sinks of C_L^{st} -like gain by assimilation and inflow from the mesophyll



compartment.

- 235 We assume that the exudation of low molecular weight organic carbon occurs via a passive diffusion (Rakshit et al., 2021; Ma et al., 2022), represented by a mass transfer approach:

$$S_{exud,st} = q_{exud} \frac{2\pi r_{in} L}{V_{st}} \quad (15)$$

$$q_{exud} = K_{lat,st} (C_L^{st} - C_L^l) \quad (16)$$

- With $K_{lat,st}$ ($cm\ d^{-1}$) is the lateral sieve tube conductivity for sucrose, V_{st} ($cm^3\ st$) is the sieve tube volume. We assume
240 that exudation occurs mainly near the root tip (Rakshit et al., 2021; Badri and Vivanco, 2009; Neumann and Römheld, 2009). Therefore, $K_{lat,st} > 0$ only for the last segment of growing roots. C_L^l ($mol\ C/cm^3\ water$) corresponds to the concentration of dissolved low molecular weight organic carbon in the soil water at the root-soil interface. It is obtained from the inner segment of the microscale soil domain assigned to the root segment. We assume that the mucilage is made from starch (*starch*, in $mol\ C/cm^3$) before being released via an active process (Rougier, 1981; Nguyen, 2009; Kutschera-Mitter et al., 1998). The
245 production and release processes are represented in the following equations:

$$\frac{\partial starch}{\partial t} = S_{starch,st} - S_{mucil,st} \quad (17)$$

$$S_{starch,st} = k_{targ,starch} (C_L^{st} - C_{L,targ}^{st}) \quad (18)$$

$$S_{mucil,st} = q_{mucil} \frac{2\pi r_{in} L_i}{V_{st}} \quad (19)$$

$$q_{mucil} = k_{mucil} starch \quad (20)$$

- 250 With $k_{targ,starch}$ ($1/d$) and k_{mucil} (cm/d) parameters controlling respectively the synthesis and decay rate of starch and the release of mucilage. $C_{L,targ}^{st}$ defines the target C_L^{st} and thus the threshold between starch synthesis and desynthesis. As in Hirschberg et al. (1998), the release of mucilage is represented via a simple first-order kinetic. We then obtain S_{mucil} ($mol\ cm^{-3}\ st\ d^{-1}$), the release rate of mucilage. $k_{mucil} > 0$ only at the tip (in our model: the last segment) of growing roots. Both q_{exud} and q_{mucil} ($mol\ cm^{-2}\ d^{-1}$) can then be used by the microscale soil domains (see Eq. (C13), Eq. (C17)).

255 2.2.4 Soil carbon transport

The changes in solute concentration are computed using the advection-diffusion-reaction equation—see Ahusborde et al. (2015) and Helmig (1997, Eq 3.100):

$$\frac{\partial \theta C_X^l}{\partial t} - \nabla \cdot (C_X^l \mathbf{u}_X) - \nabla \cdot (D_X(\theta, \phi) \nabla C_X^l) - S_X (-S_{1DS-3DS,X}) = 0 \quad (21)$$

$$S_{ads,X} + S_{microbe,X} = S_X \quad (22)$$

- 260 C_X^l ($mol/cm^3\ water$) is either the concentration of carbon from dissolved low molecular weight organic compounds (C_L^l) or high molecular weight organic compounds (C_H^l) in the soil liquid solution. S_X ($mol\ C\ cm^{-3}\ scv\ d^{-1}$) is the net source of C_X^l , and it encompasses the adsorption of C_X^l ($S_{ads,X}$, $mol\ C\ cm^{-3}\ scv\ d^{-1}$, see section 2.2.5) and the changes caused by microbial reactions ($S_{microbe,X}$, $mol\ C\ cm^{-3}\ scv\ d^{-1}$, see appendix D and Eq. (C1)). $S_{1DS-3DS,X}$ is an additional source term only used at the microscale and presented in Eq. (C7). \mathbf{u}_X is the advective flux.



265 $D_X(\theta, \phi)$, the effective dispersion in the porous medium (caused by molecular diffusion and hydrodynamic dispersion), is obtained from Millington and Quirk (1961), as implemented by Koch et al. (2021):

$$D_X(\theta, \phi) = D_{Xw} \frac{\theta^{\frac{10}{3}}}{\phi^2} \quad (23)$$

With D_{Xw} (cm^2/d) the diffusion coefficient of the carbon compound in water. Low molecular weight organic C compounds can be modelled as true solutes and are thus subject to convection. High molecular weight carbon compounds correspond to the
270 plant mucilage releases, a gel-like substance when hydrated (Ma et al., 2022; Kutschera-Mitter et al., 1998). To simulate the rheology of mucilage slime, we adopt a simplified approach with a null advective flux (u_H) and a lower diffusion coefficient ($D_{H,w} < D_{L,w}$). The implementation of Eq. (21) for the macroscale 3D soil and microscale 1D soil are given respectively in appendices C1 and C2.

2.2.5 Adsorption

275 We describe in this section the adsorption of low molecular weight organic C compounds (C_L) from the liquid phase (C_L^l) onto the solid phase (C_L^s). As Sircan et al. (2025), we describe the adsorption as linear. However, instead of equilibrium sorption, we used linear first-order kinetics. This was necessary in order to obtain the same result at the micro- and the macroscale. Moreover, not assuming instantaneous equilibrium allows us to set lower time steps during the simulations. We further assume that only the low molecular weight organic substances can be sorbed. Adsorption was implemented according to Ahrens et al.
280 (2020):

$$\frac{\partial C_L^s}{\partial t} = k_{ads} C_L^l (C_{L,max}^s - C_L^s) - k_{des} C_L^s \quad (24)$$

$$C_{L,max}^s = C_{L,max}^l = \rho_b \frac{k_{clsm} k_{clay+<20\mu\text{msilt}}}{M_{mass,C}} \quad (25)$$

with k_{ads} ($23265.14 \text{ cm}^3 \text{ scv mol}^{-1} \text{ C d}^{-1}$) and k_{des} (4.47 d^{-1}) the adsorption and desorption rates, defined according to the values given by Ahrens et al. (2020). $C_{L,max}^s$ ($\text{mol C cm}^3 \text{ scv}$) is the maximal concentration of adsorbed C_L^s , ρ_b
285 ($1.51 \text{ g mineral soil/cm}^3 \text{ scv}$) is the soil bulk density, $M_{mass,C}$ ($12.011 \text{ g C mol}^{-1} \text{ C}$) is the molar mass of carbon, $k_{clay+<20\mu\text{msilt}}$ (0.45–, Wang et al. (2018)) is the fraction of clay and silt smaller than $20 \mu\text{m}$. k_{csm} (–) is an empirical factor defined according to the make up of the clay minerals in the soil. According to Jiang et al. (2014), the Selhausen soil (used to calibrate the model) is dominated by illites, a 2 : 1 mineral. Consequently, $k_{csm} = 0.079$ (Ahrens et al., 2020). This yields $C_{L,max}^s = 4.5e^{-3} \text{ mol C cm}^{-3} \text{ scv}$. From the adsorption dynamic, we get the adsorption net sink for dissolved low
290 molecular weight organic carbon: $S_{ads,L} = -\frac{\partial C_L^s}{\partial t}$, used in Eq. (22). As high molecular weight organic carbon compounds represent the mucilage gel, no adsorption is represented: $S_{ads,H} = 0$.

2.2.6 Plant growth and perirhizal zone

We simulate dynamic plants that grow according to input parameters (representing plants genetically determined characteristics) and to their water and sucrose status (see Giraud et al. (2023)). This leads to changes in root segment lengths and to the creation



295 of new root segments. The method used to define the shape, water and solute content of new or growing microscale domains is presented below.

Currently, each root segment (and associated microscale domain) is allocated to the soil voxel containing its centre when the segment is first created, even if one or both segment extremities are out of the voxel. In order for the output to be realistic, it is therefore important for the maximum root segment size to be lower or near the length of a soil voxel. Moreover, for the current
300 setup, root segments will remain in the same soil voxel even if the centre of an existing segment (because of segment elongation) moves to another voxel. We assume that these simplifications will have a limited influence on the results if the resolution is high enough. After simulating plant growth for the time step N , we obtain the new lengths (L , cm) and radius (r_{in} , cm) of the roots, which are, respectively, the lengths and inner boundary of the microscale domains. From these shape data, we recompute the outer radial boundary of the 1D domains (r_{out} , cm) according to the volume of the soil voxels ($V_{3DS,scv}$) and the number
305 of microscale domains contained within (nr). For the microscale domain k in the voxel i :

$$r_{out,k}^N = \sqrt{\frac{r_{in,k}^2 L_k^N}{\sum_j^{nr_{i,N}} r_{in,j}^2 L_j^N} \frac{V_{3DS}}{\pi L_k^N} + r_{in,k}^2} \quad (26)$$

Consequently, creation of new roots or changes in L and r_{in} of existing roots in a voxel can lead to changes in the perirhizal zone volume allocated to an individual microscale soil domain. From the soil point of view, a higher density of roots in the voxel leads to smaller perirhizal zones for each of the root segments contained in it. The description of the method used to
310 update the amounts of water and carbon in the microscale models as they are created and change shape is presented in the appendix E. In brief, the gradient of existing 1D domains with decreasing volume is preserved. We then compute the volume of newly freed soil for each voxel. From the amount of water and carbon lost by the 1D models, we obtain the mean water content and carbon concentration in the freed space. This volume (and corresponding water and solute contents) is distributed between the new and expanding microscale domains to respect the results of Eq. (26).

315 2.3 Model application: The effect of dry spells on soil carbon and microbial dynamics near a growing plant

The implementation setup for the coupled model follows the one used in Giraud et al. (2023), with Van Genuchten parameters measured from one testing site of the Research Center Jülich, located in Selhausen (50.8659 N, 6.4471 E). We simulated the growth of a C3 monocot under a control scenario (hereafter called *baseline*) and compared it with dry spells at two plant development stages. Both dry spells were represented by a period of one week without rainfall: 11 to 18 days and 18 to 25
320 days after sowing, hereafter called *earlyDry* and *lateDry*. The virtual plants were obtained by running the plant model up to day 10 (after sowing) using a mean empirical growth rate (neither dependent on the carbon- nor water-flow) and without simulation of the water and carbon fluxes. From the 10th day onward, we simulated the carbon and water fluxes and of the carbon- and water-limited growth, as well as the soil carbon dynamic. The plants all grew under the *baseline* conditions with a static soil (constant mean $\psi_{m,soil} = -100$ cm at hydraulic equilibrium), except during the dry spells: day of growth 11 to 18
325 for *earlyDry*, and 18 to 25 for *lateDry*). At the start of the dry spells, the mean soil water potential was lowered to -450 cm and warmer and drier atmospheric conditions were simulated. After the dry spells, the *baseline* environmental and static soil

water conditions were used. We used a no-flux boundary condition for the macroscale soil. Fig. 5 summarises the timeline of the three scenarios.

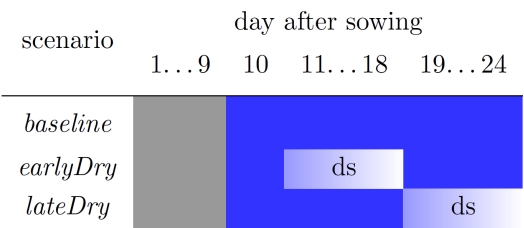


Figure 5. Timeline of the simulations. The grey (resp. blue) cells indicate the empirical (resp. semi-mechanistic) growth period and "ds" the implementation of the dynamic soil. The blue gradient during the dynamic soil simulation represents the decreasing soil water content. The sharp shift from dark to light (resp. light to dark) blue at the beginning (resp. end) of the dry spells represents the implementation of the *dry spell* (resp. *baseline*) atmospheric and initial (resp. constant) soil variables. Figure taken from Giraud et al. (2023)

For the plant model, the calibration of Giraud et al. (2023) was adapted to better follow our assumptions regarding the plant mucilage and carbon dynamic (e.g., preferential carbon usage for growth over exudation), and to address the divergences between the outputs of Giraud et al. (2023) and experimental observation (light dry spells caused carbon rather than water scarcity). Changes were also made to the lateral conductivity ($k_{lat,x}$, $cm\ hPa^{-1}\ d^{-1}$) in the mature root zone: the constant value was computed according to Bramley et al. (2007, Fig. 4.15) and set to 1.5% of $k_{lat,x}$ within the immature root zone, see appendix H for a more detailed description.

The selection of the biokinetic parameter sets is given in appendix I. Briefly, Sircan et al. (2025) computed 1650 parameter sets respecting parameter and process constraints defined according to a literature review. Those sets were divided into three groups according to the resulting C_L^l radial profile for the microscale domains. 33 sets were selected randomly from each group and a simulation was run for four days. We then selected three parameter sets giving diverging results. Table 1 presents the characteristics of the selected sets. The first set, thereafter called *highCO2*, led to a high CO_2 production in spite of a low microbial development. The second set, thereafter called *highMB*, led to the highest microbial development. The third set, thereafter called *lowMUptake*, led to the highest soil solute concentration (low microbial solute uptake).



Table 1. Qualitative summary of the characteristics of the three selected biokinetic parameter sets (*highCO₂*, *highMB*, *lowMUptake*). O: oligotrophs, C: copiotrophs, (de)act.: activation and deactivation, VS: compared against. The evaluation has the following order (representing the low-to-high gradient): – < . < + < ++

denomination	fitness		act. VS deact.		(de)act. VS growth + decay		O VS C		CO ₂ losses
	O	C	O	C	O	C	(de)act.	fitness	
<i>highCO₂</i>	+	–	.	.	+	+	.	+	++
<i>highMB</i>	+	.	+	+	++	.	–	+	+
<i>lowMUptake</i>	–	.	–	–	.	.	.	–	–

2.4 Analysis of the outputs

The data were treated and visualised with Python3.10 (Van Rossum and Drake Jr, 1995).

2.4.1 Scale definition for model evaluation

To take advantage of the multiscale setup, we evaluated the model outputs at four different scales: macroscale, bulk soil, perirhizal_{trunc}, microscale. We define the macroscale as the soil voxels (Fig. 1(b)) that contain at least one root at the end of the simulations in any of the scenarios. This soil space is therefore constant and equal for all the simulations. We define the bulk soil as the macroscale data of voxels containing at least one root at each time step, potentially different for each simulation. For the perirhizal_{trunc} analysis, we aggregated the mean concentrations for each microscale domain truncated at a specified distance from the root surface, denoted as $\Delta r_{analysis}$. The value of $\Delta r_{analysis}$ was pragmatically set to 0.06 cm. It corresponds to the minimum distance between the inner and outer boundaries of the microscale domains obtained during the simulation. By setting a consistent distance between the inner and outer boundaries of the truncated domains, we obtained a partial uniformity between the domains that reduced variations that could arise from differences in soil allocation to each domain (see Eq. (26)). Moreover, using these truncated 1D models allowed us to evaluate a soil area nearer to the root surface, for comparison with the bulk soil scale. At the microscale, we evaluated the data for each segment of the 1D models (Fig. 1(c)) individually.

2.4.2 Vertical concentration profiles

To evaluate the vertical concentration profiles, we computed the total soil volume, water volume, and C content (for each C pool) for each depth at the bulk soil scale. This allowed us to determine the corresponding mean C concentration and water content around the root systems. Additionally, we present the minimum and maximum C concentrations (for each C pool) and water content values at each soil depth to capture the lateral variability.



2.4.3 Complementary cumulative volume distributions

We created complementary cumulative volume distribution plots of the concentration at the perirhizal_{trunc} scale. In these plots, the x-axis represents different concentration values. The y-axis shows the absolute or relative volume of the selected perirhizal zone (up to 0.06 cm from the root surface) with concentrations equal to or greater than the corresponding x-axis value. This representation provides insight into the spatial variability and distribution of concentrations within the specified zone. Additionally, these graphs allow us to evaluate how much of the perirhizal zone volume exceeds certain concentration levels, such as hotspot thresholds.

2.4.4 Relative change of soil carbon distribution

To evaluate the change in plant-soil C turnover for the different weather scenarios and biokinetic parameter sets, we categorised C into four pools: solutes (dissolved and sorbed low molecular weight organic C and high molecular weight organic C), microbes (including total oligotrophic and copiotrophic C), active microbes (including active oligotrophic and copiotrophic C), and emitted CO₂ (microbial respiration). We evaluated the C content at the macroscale for each of these pools at each time step and normalised the values for *earlyDry* and *lateDry* under each biokinetic parameter set according to the corresponding baseline scenario: $(C_{X,spell} - C_{X,baseline})/C_{X,baseline}$, with X the name of the C pool.

2.4.5 Soil organic carbon hotspots

One important effect of plant C releases is the resulting changes in soil organic C (SOC). Using the study of Poeplau and Don (2023), we set three SOC thresholds defined according to the $SOC/SOC_{expected}$ ratio: 0.65, 0.83, 1.16. $SOC_{expected}$ ($mol\ C\ cm^3\ scv$) is the average expected SOC according to the soil clay content. Following the method of Poeplau and Don (2023) and the Selhausen clay content data of Wang et al. (2018), we set $SOC_{expected} = \frac{\rho_b}{1000M_C}(0.0288k_{clay} + 13.674) = 2.36e^{-3}\ mol\ C\ cm^3\ scv$, with k_{clay} the soil clay content in $g\ kg^{-1}$, ρ_b ($g/cm^3\ scv$) the soil bulk density, M_C ($g\ C/mol\ C$) the C molar mass. The 1/1000 factor is used to go from $g\ kg^{-1}$ to $g\ g^{-1}$.

A first evaluation of the outputs showed that our simulated values were almost always in the lowest SOC class and significantly below the mean Selhausen SOC reported by Wang et al. (2018). For the hotspot analysis, we therefore added an SOC_{slow} class representing the very slow decomposing SOC, assumed to be constant over the study period. We set $SOC_{slow} = SOC_{theoric} - SOC_{simulated,init}$, with $SOC_{simulated,init}$ the total SOC explicitly simulated in our model (solute and microbial pools) at the beginning of the simulation, and $SOC_{theoric}$ the value from Wang et al. (2018). We then set the variable $SOC = SOC_{simulated} + SOC_{slow}$, computed at the microscale. This is the value used to compare with the SOC thresholds given by Poeplau and Don (2023). We use a stacked area graph to represent the SOC hotspots, as soil above the higher thresholds is also above the lower thresholds. As presented by Landl et al. (2021a), we computed the volume-normalised hotspot volume to obtain a metric for the efficiency of the rhizodeposition.



2.4.6 Radial concentration profiles

Finally, for the microscale, we presented C concentration data for all segments of the 1D domains on one scatter plot per weather scenario and parameter set, giving, on the x-axis, the radial coordinate of the segment centers according to the root surface.

3 Results

3.1 Three-dimensional simulation of microbial carbon dynamics in the soil-plant system

The integrated plant-soil-microbiome model extends the FSPM model of Giraud et al. (2023)) by implementing microbial carbon (C) dynamics in soil. Consequently, the extended FSPM model now provides 3D simulations of plant architecture, water and C dynamics in the plant and the soil, and microbial dynamics in the soil, including the rhizosphere. While this study focuses on C cycling and microbial dynamics at the root-soil interface, more detailed simulation results regarding water and C flow in a plant for the three considered weather scenarios are given in Giraud et al. (2023). Fig. 6 shows a typical simulation after 24.5d of plant growth (midday) for a biokinetic parameterisation that results in high microbial CO₂ production (*highCO2*) under the *baseline* scenario. The simulation highlights an increasing concentration of dissolved low molecular weight organic C (C_L^l) and active copiotrophs (C_C^a) in response to root exudation in the upper part of the root system, near its centre.

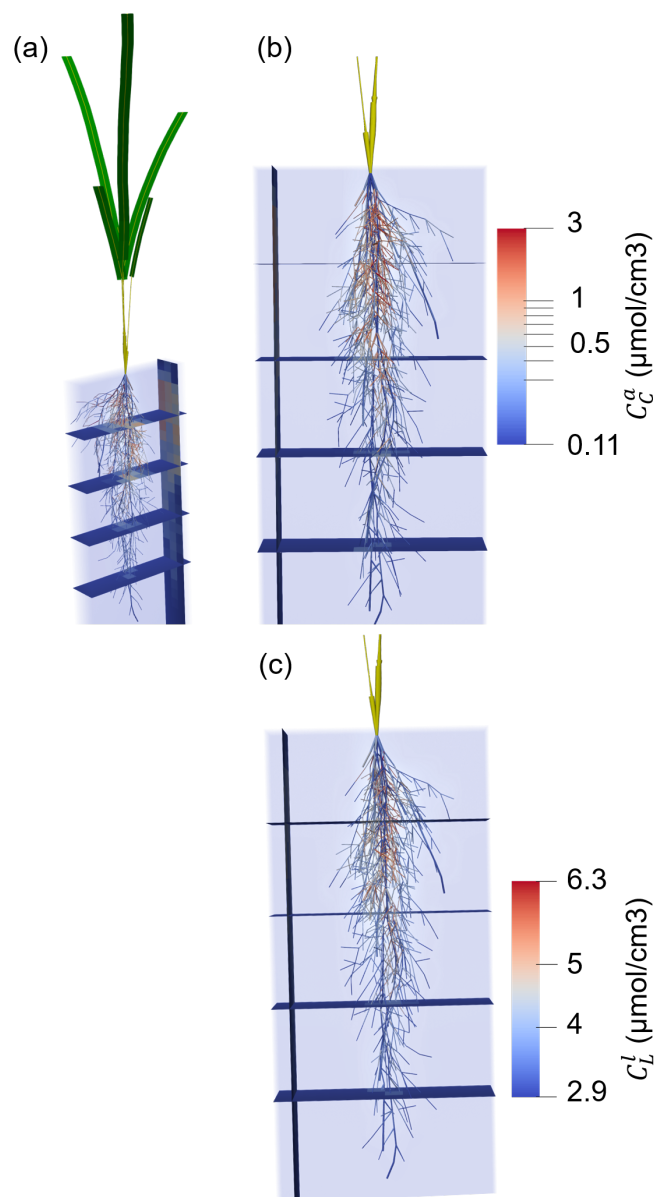


Figure 6. 3D representation of the plant and soil domains for microbial biokinetic parameterisation *highCO2* under the *baseline* scenario at 24.5d of growth, with (A) the whole plant, (B, C) zoom on the root system. (A, B) present the concentration of active copiotrophic biomass C (C_C^a) and (C) that of dissolved low molecular weight organic C (C_L^l). The soil colours give the concentration in the bulk soil. The root colours give the concentration at the soil-root interface. Unified colours were given to the aboveground roots, shoot segments and leaf blades.



3.2 Plant processes

Fig. 7.A presents the plant xylem mean water potential (ψ_x , cm) for each biokinetic parameterisation and weather scenario. The simulation results reflect the diurnal dynamics of ψ_x in response to the truncated sinusoidal curve used to describe the atmospheric conditions (light input, air relative humidity and temperature). These boundary conditions affected the plant stomatal regulation and, thus, the C assimilation and transpiration rate. We observed an increase of ψ_x over time for *baseline* as the leaf:root ratio decreased. With drought, ψ_x rapidly decreased at the beginning of the dry spells and recovered after its end in response to changes in soil water content and mean air relative humidity during the dry spells (see (Giraud et al., 2023, Table 1)). Towards the end of the simulation with *earlyDry*, ψ_x converged to the values of *baseline*, indicating a full recovery of the plant water uptake capacity. As a consequence of the lower leaf:root ratio, ψ_x was lower at the beginning of the dry spells for *earlyDry* (11th day) than for *lateDry* (18th day). However, in comparison to *earlyDry*, the higher plant transpiration under *lateDry* with higher total leaf and root surface area led to a quicker decrease in soil water content. This mechanism induced lower ψ_x in the *lateDry* compared to the *earlyDry* scenario from the third day after the start of the dry spells onward (13th and 20th day).

Fig. 7.B shows the cumulative amount of C used for growth (and growth respiration) during the simulation. The diurnal cycle of ψ_x affected the plant growth. During the day, the transpiration-induced lower ψ_x limited plant growth compared to the night, where increased ψ_x permitted faster, albeit still water-limited, C assimilation and biomass production. The required C was taken from the starch reserves built up during the day. We can also observe trends over the simulation. Unlike younger plants, older plants could maintain growth during the diurnal period outside of the dry spells. During the dry spells, growth occurred only at night and at a severely reduced rate. On the last three nights of the late dry spell, we observed no night-growth due to lower plant night ψ_x .

Plant maintenance respiration increased during the spells due to the higher air temperatures. In the *earlyDry* scenario, plant growth was severely limited compared to *baseline*, resulting in a lower plant maintenance respiration rate after the dry spell ended (18th day). For *lateDry*, we saw a lower maintenance respiration rate from the fourth day of the spell. The total cumulative respiration (growth and maintenance related) at the end of the simulation was highest for the *baseline* scenario. It was about 29% lower for *earlyDry* and 18% lower for *lateDry*. The biokinetic parameterisation had no significant effect on the plant water processes or growth and maintenance.

Figs 7.C and D present the cumulative amount of C used for (respectively) passive exudation and active mucilage release during the simulation. The plant water balance affected the exudation rate. During the simulation, exudation occurred only under limited C use for growth in response to low ψ_x . Although the mucilage release was not always maintained at night (e.g., at the end of the *earlyDry* simulation), this process was less affected by the diurnal cycle than the exudation. This led to qualitative changes in the type of C released by the plant throughout the day. In comparison to *baseline* the early dry spell led to a lower total exudation at the end of the simulation: -32%, -35%, and -37% for *highCO2*, *highMB*, and *lowMUuptake*, respectively. Conversely, the late dry spell resulted in higher exudation compared to *baseline*: +29% for *highCO2* and *highMB*, +26% for *lowMUuptake*. Thus, the dry spells triggered both positive and negative effects on exudation. On the one hand, more



C became available for exudation with decreasing plant growth. On the other hand, the lower ψ_x led to a closing of the stomata, causing a lower assimilation rate per unit of leaf area.

Lower plant growth also led to lower leaf and total root surface area compared to *baseline*, which limited exudation. The effect of the simulated spells on total exudation was, therefore, dependent on the stage of plant growth at the start of the spell. After the end of the early dry spell (days 18-23), the daily plant exudation for *earlyDry* was higher than for *baseline*, partially reducing the exudation gap between the two. The total mucilage release under *earlyDry* at the end of the simulation was close to that under *baseline*: -11% , -2% , and $+6\%$ for parameter sets *highCO2*, *highMB*, and *lowMUptake*, respectively. In contrast, mucilage release reached $+139\%$ for *highCO2* and *highMB* and $+170\%$ for *lowMUptake* under *lateDry*. We found an effect of the biokinetic parameterisation on exudation and mucilage release. The *highCO2* and *highMB* parameterisation, associated with high microbial C usage rates resulted in lower concentrations of dissolved low molecular weight organic C (C_L^l mol C/cm⁻³). This lower C_L^l increased passive exudation. The higher exudation was then compensated by the plant starch reserves (in the mesophyll and around the plant transport tissues) and did not affect the plant growth or maintenance. As the mucilage release rate is a function of the plant starch content, higher exudation induced lower mucilage release. These differences in exudation and mucilage release appeared only after the onset of the dry spells. The release rates between the biokinetic parameterisations for *earlyDry* became similar again from the third day after the end of the dry spell onward. The highest exudation rate per unit of root surface for a single segment was obtained at 11 day 5hrs with *baseline* and *lateDry* (0.153 mmol C cm⁻² d), at 10 day 21hrs for *highCO2* and *lowMUptake* with *earlyDry* (0.145 mmol C cm⁻² d), and at 12 day 8hrs for *highMB* with *earlyDry* (0.148 mmol C cm⁻² d).

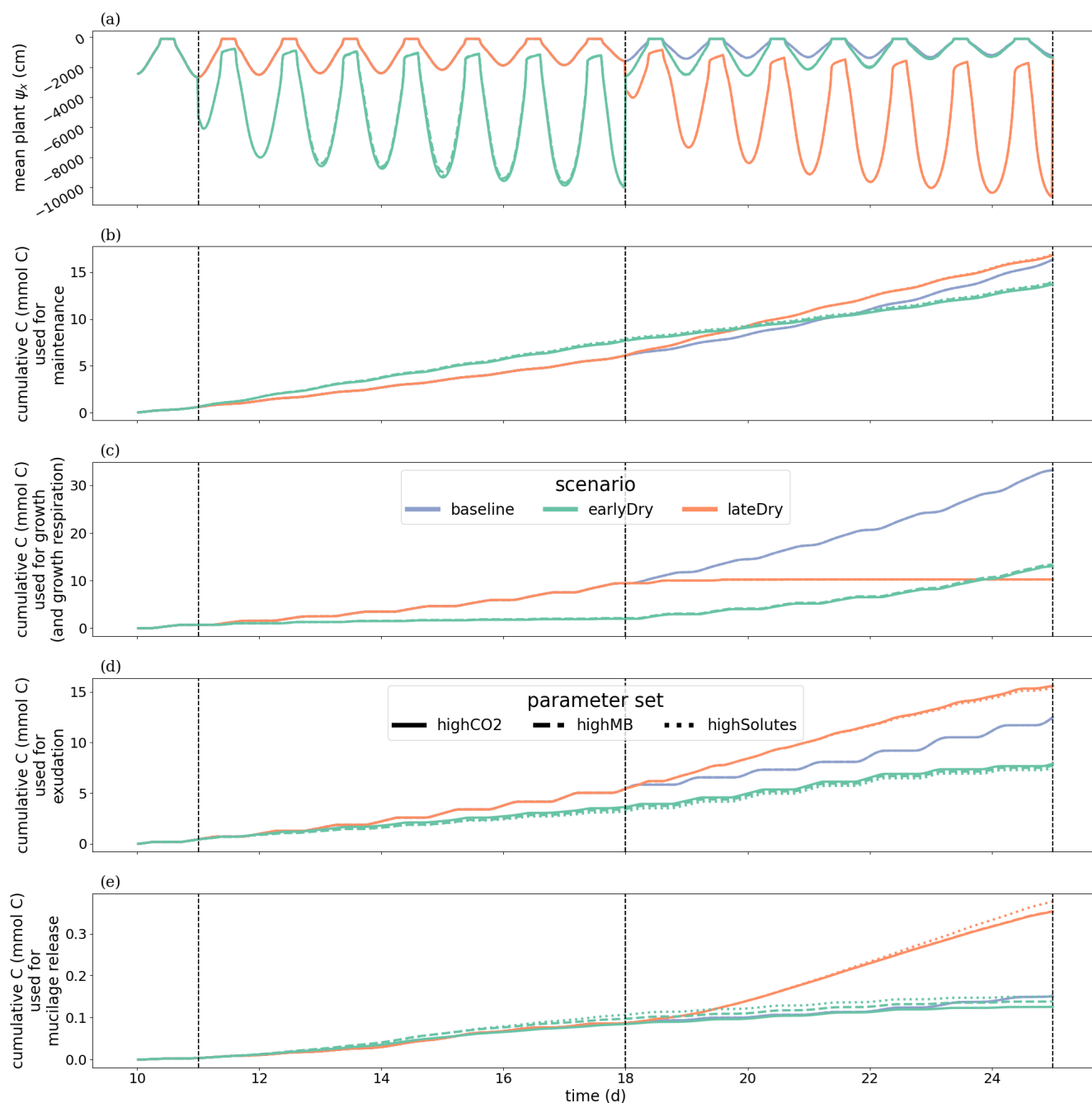


Figure 7. Dynamics of Plant water- and carbon-related metrics:

(A) the mean plant xylem water potential (ψ), (B) cumulative carbon growth and growth respiration, (C) exudation, (D) mucilage release. Line colours indicate the weather scenarios: baseline (blue) against an early (green) and late (red) dry spell. Line types represent different biokinetic parameter sets. The vertical dotted lines show the beginning and end of the early (day 11 to 18) and late (day 18 to 25) dry spells. Please note that the scales of the y-axis differ in each subplot.



3.3 Vertical concentration profiles

Fig. 8 presents the vertical concentration profiles of organic C, microbial pools and produced CO₂ from microbial respiration at the end of the simulation for the bulk soil scale. The root system structure affected the concentration profiles. The peaks of organic C between 0 cm and 13 cm of depth corresponded with the location of the highest root length density (Fig. 8(a), (b), (c) and Fig. J1). A second peak of maximum C concentration was observed at the bottom of the profile close to the tips of primary roots. That second peak is especially strong for *lateDry* due to lower root growth, i.e., very few root segments reached 20 cm, such that the mean C concentration equals the maximum concentration. Conversely, the higher lateral dispersion of the roots in the upper soil layers led to a stronger lateral variability in the concentration profile (larger min-max ranges). Stronger plant growth under *baseline* resulted in perirhizal zones and rhizodeposition at lower depths such that the C accumulation at the root tips was much less pronounced compared to the dry spell scenarios.

The biokinetic parameterisation strongly influenced the C concentration profiles (Fig. 8(e)-(j)). With *highCO2*, solute and microbial C concentrations (C_L^l , C_L^s , C_H^l , C_C , C_O) were lowest. The *highMB* parameterisation also led to low solute concentrations but triggered increased microbial C due to higher microbial C consumption. With *lowMUptake*, solute concentrations were highest because of low microbial C uptake. These results are consistent with the observations obtained during the model conditioning (see appendix I).

Although the weather scenarios had a less pronounced effect on the concentration profiles than the biokinetic parameterisation, the dry spells induced distinct effects. Under *earlyDry*, the concentration profiles were close to that of *baseline* (e.g., C_C , Fig. 8(e)), or between *baseline* and *lateDry* (e.g., C_H^l , Fig. 8(b)). This shows the resilience soil C cycling to the early dry spell. In particular, despite the lower total exudation, the concentration of C_L^l for *earlyDry* is close to that of the *baseline* due to the increased exudation rate during the second half of the simulation (Fig. 8(a)). Under *lateDry*, we observed higher C_H^l . This can be attributed to higher plant mucilage release for this scenario (Fig. 8(b)). The highest C_C^a and C_O^a values at the last time step are obtained with *baseline* (Fig. 8(g), (h)). The differences in the microbes' activation can partly be explained by the water content remaining at the high default value (−100 cm) during the whole simulation under *baseline*. C uptake by copiotrophs was higher (high C_C , and microbially respired C as CO₂ but lower C_L^l) under *lateDry* for *highCO2* and *highMB* (Fig. 8(d), (e)). This results can be linked to the higher total exudation and lower water content, making the C resources more readily available to the microbes. However, for *lowMUptake*, the higher C uptake by copiotrophs occurred under *baseline*. Thus, water was relatively more limiting than C supply for copiotrophic growth with *lowMUptake* (compared with *highCO2* and *highMB*) because of a lower maximum uptake rate. For that same reason, maximum C_O for each parameter set is very slightly higher (< +0.7%) under *baseline*.

Due to the short simulation time, C_O (Fig. 8(f)) showed no significant growth at the bulk soil scale (< 3% of growth), but the dry spells weakly affected the proportion of active and dormant oligotrophs (Fig. 8(h), (j)).

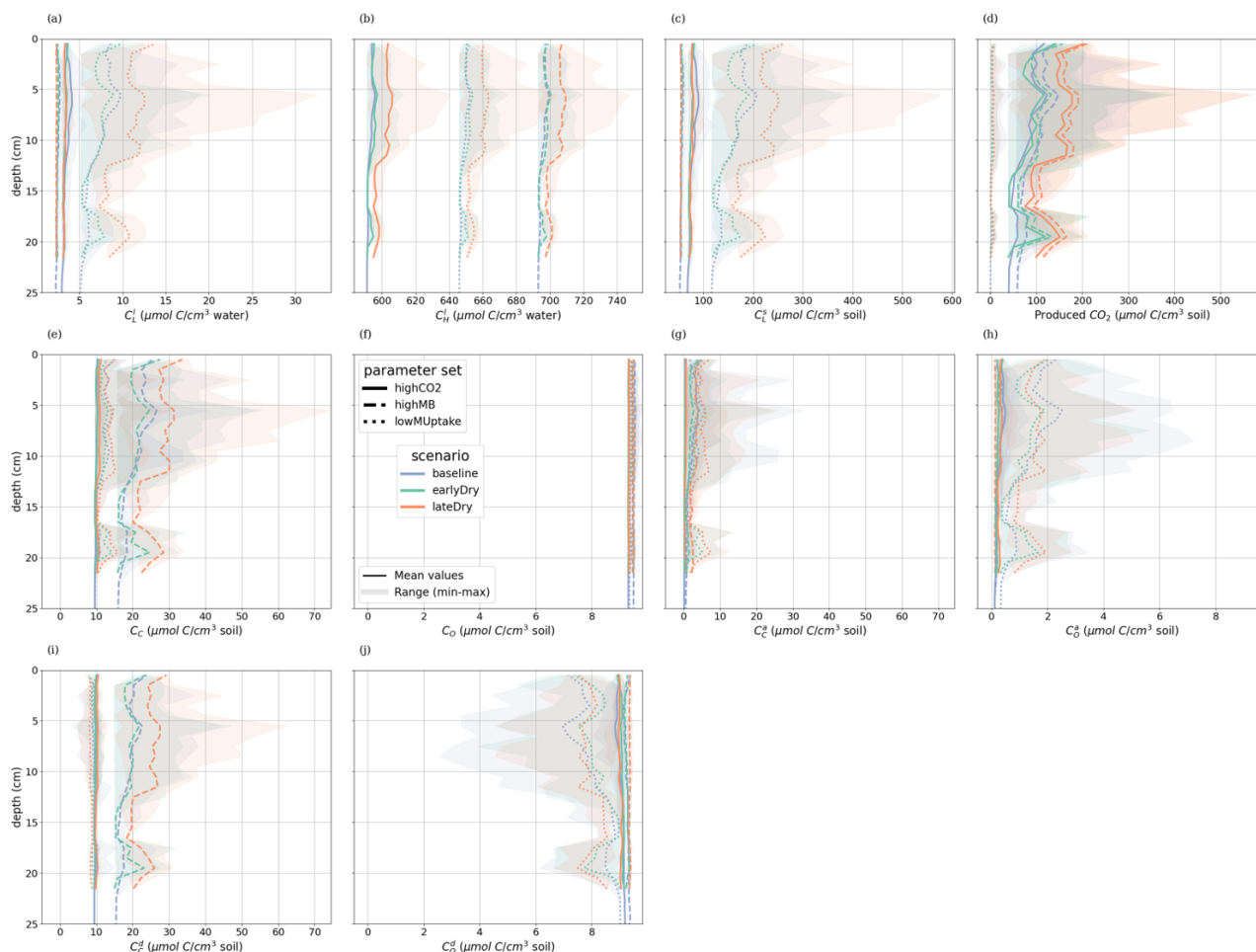


Figure 8. Mean bulk soil concentrations of the soil carbon with depth

(a) dissolved and (c) sorbed (C_L^s) low-molecular-weight organic molecules, (b) high-molecular-weight organic molecules (C_H^i), (d) produced CO_2 , (e, g, i) total (C_C), active (C_C^a) and dormant (C_C^d) copiotrophs, (f, h, j) total (C_O), active (C_O^a) and dormant (C_O^d) oligotrophs. Line colours indicate the weather scenarios: baseline (blue) against an early (green) and late (red) dry spell. Line types represent different biokinetic parameter sets. The semi-transparent bands give the range between the minimum and maximum concentration in soil voxels with at least one root segment at each depth.

3.4 Complementary cumulative volume distributions

Fig. 9 shows the perirhizal_{trunc} volume with a concentration inferior or equal to the value on the x-axis. The description and motivation of the evaluation method for this figure are given in section 2.4.4. A video presenting this graphic for each time step is available in the supplementary documents ("Video S1"). Root exudation and mucilage release triggered concentration peaks of solutes and microbial C in the perirhizal_{trunc} volume (Fig. 9). Particularly copiotrophs were strongly stimulated reaching high abundances up to $580 \mu\text{mol}/\text{cm}^3$ soil for lateDry with highMB. Both dry spells led to strongly reduced total



perirhizal_{trunc} volumes at the end of the simulation of 42% for *earlyDry* and 34% for *lateDry* in relation to *baseline*. As a consequence, maximum C_H^l and C_C^l concentrations were lowest with *baseline* because the released plant C triggering
500 copiotrophic growth was distributed in a larger volume.

While *lateDry* with *highCO2* and *highMB* caused the highest CO_2 , C_C and C_C^d peaks at the bulk soil scale (see respectively Fig. 8(d), (e), (i)), for the perirhizal_{trunc} zone the highest values for these parameter sets were obtained with *earlyDry* (Fig. 9(c), (d), (f)). The simulated copiotroph growth during the dry spell occurred earlier under *earlyDry*, creating a larger pool of C_C^d ready to be re-activated and grow during periods of high exudation. As the growth rate is a function of the current C_C^a , high
505 C_C^d early in the simulation favoured the overall growth in those hotspots.

Parameterizing the model with *highMB* under *lateDry* caused an especially high C_C over most of the perirhizal_{trunc} volume with an increase of active and a strong build-up of dormant copiotrophs (Fig. 9(d), (e), (f)). Conversely, although *highMB* under *lateDry* also led to a slight increase in the total and dormant oligotrophic concentrations (Fig. 9(g), (i)), it resulted in a decrease in the amount of active oligotrophs (Fig. 9(h)). This simulated pattern indicates a pronounced competition between
510 oligotrophs and copiotrophs for this scenario-parameter set combination. Indeed, the C_O^a values started decreasing strongly during the second half of the late dry spell, when the exudation rate became also lower.

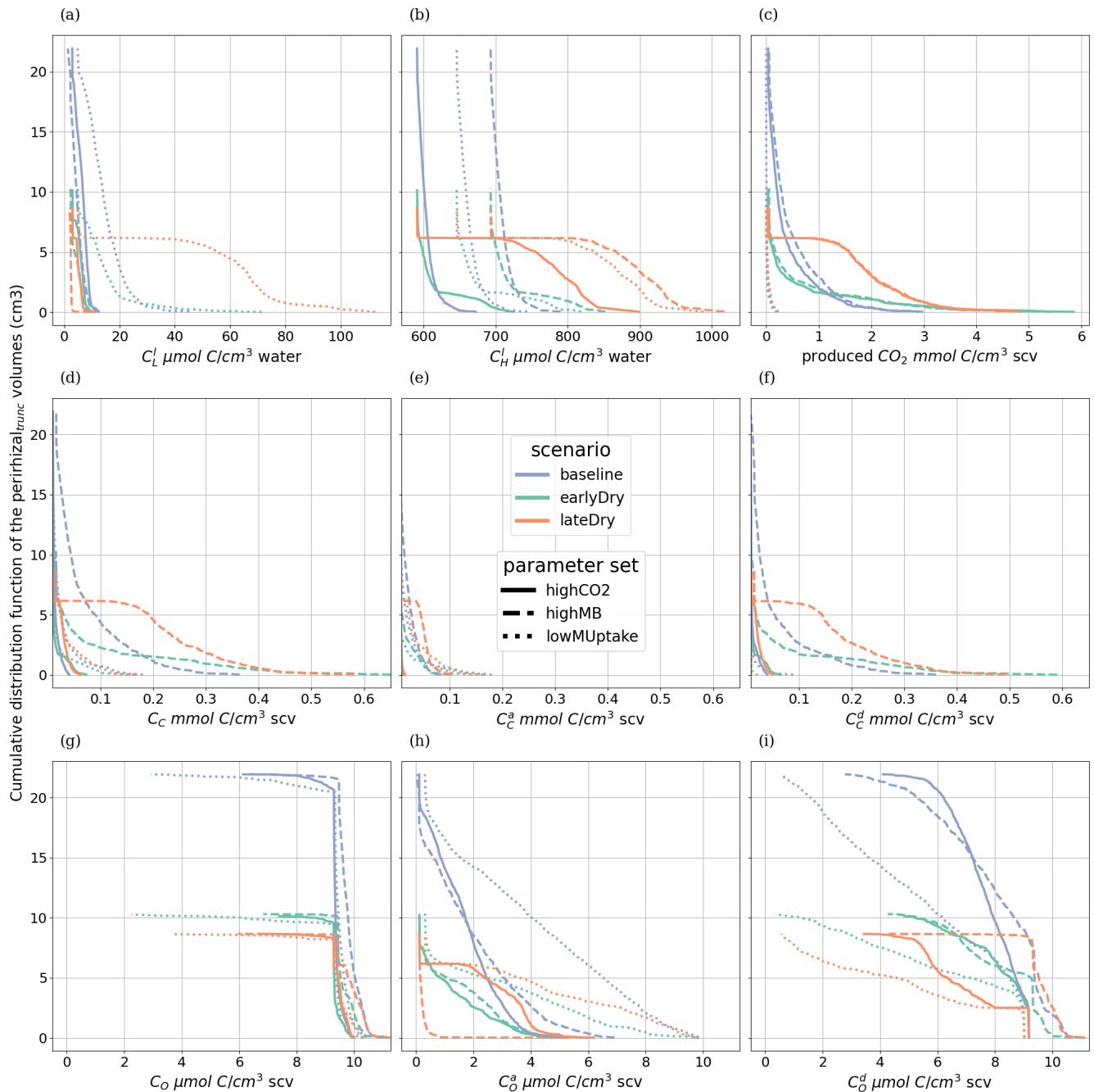


Figure 9. Perirhizal zone volume according to the minimal concentration of organic carbon in the truncated perirhizal zones, for (a) carbon of low-weight dissolved organic molecules (C_L^l), and (b) carbon of high-weight organic molecules in the water phase (C_H^l), (c) emitted CO_2 , (d) total (C_C) (e) active (C_C^a) (f) dormant (C_C^d) copiotrophs in the soil phase, (g) total (C_O) (h) active (C_O^a) (i) dormant (C_O^d) oligotrophs in the soil phase. The line colors give the weather **scenario**: baseline (blue) against an early (green) and late (red) dry spell. The line types represent the different biokinetic parameterisation. Subplots d, e, f and g, h, i have the same scale on the x-axis.



3.5 Carbon pool distribution

515 We wished to evaluate the changes in C turnover within the plant-soil system, according to the weather scenarios and for the different biokinetic parameter sets. Consequently, Fig. 10 gives the relative changes of C content in different C pools, compared with the *baseline* scenarios. The relative increases of activated microbes-C and solutes-C (Figs. 10.B and 10(c)) correspond to the night periods, when less C was exudated with *baseline* compared with the other scenarios. These periods also corresponded to higher soil matric potentials, diminishing the negative effects of the low soil θ on microbial activation during the dry spells.

520 This relatively higher activated microbes-C pool was observed for the *highMB* and *highCO2* parameter sets with *lateDry*, although the values were lower than for *baseline* at the last time step. The *lateDry* scenario led consequently to a redistribution of C in the microbial and emitted CO₂ pools. Therefore, in spite of the higher total exudation, the solutes-C pool is lower compared with the corresponding *baseline* scenarios. On the contrary, for *lowMUptake*, the *lateDry* scenario led to a higher accumulation of C within the solutes pools (Fig. 10(d)). We can also note that, while we have converging relative solutes-C

525 values between *earlyDry* and *lateDry* for *highMB* and *highCO2* by the end of the simulations, the values for *lowMUptake* are diverging. For all *earlyDry* scenarios, we observe that less C enters the soil domain, leading to relatively lower values compared with *baseline* for all pools by the end of the simulations. We also found a small relative uptick of activated microbes-C for the *highMB* and *highCO2* parameter sets after the spell (Fig. 10(b)), linked with the increased soil water content and plant exudation (Fig. 7).

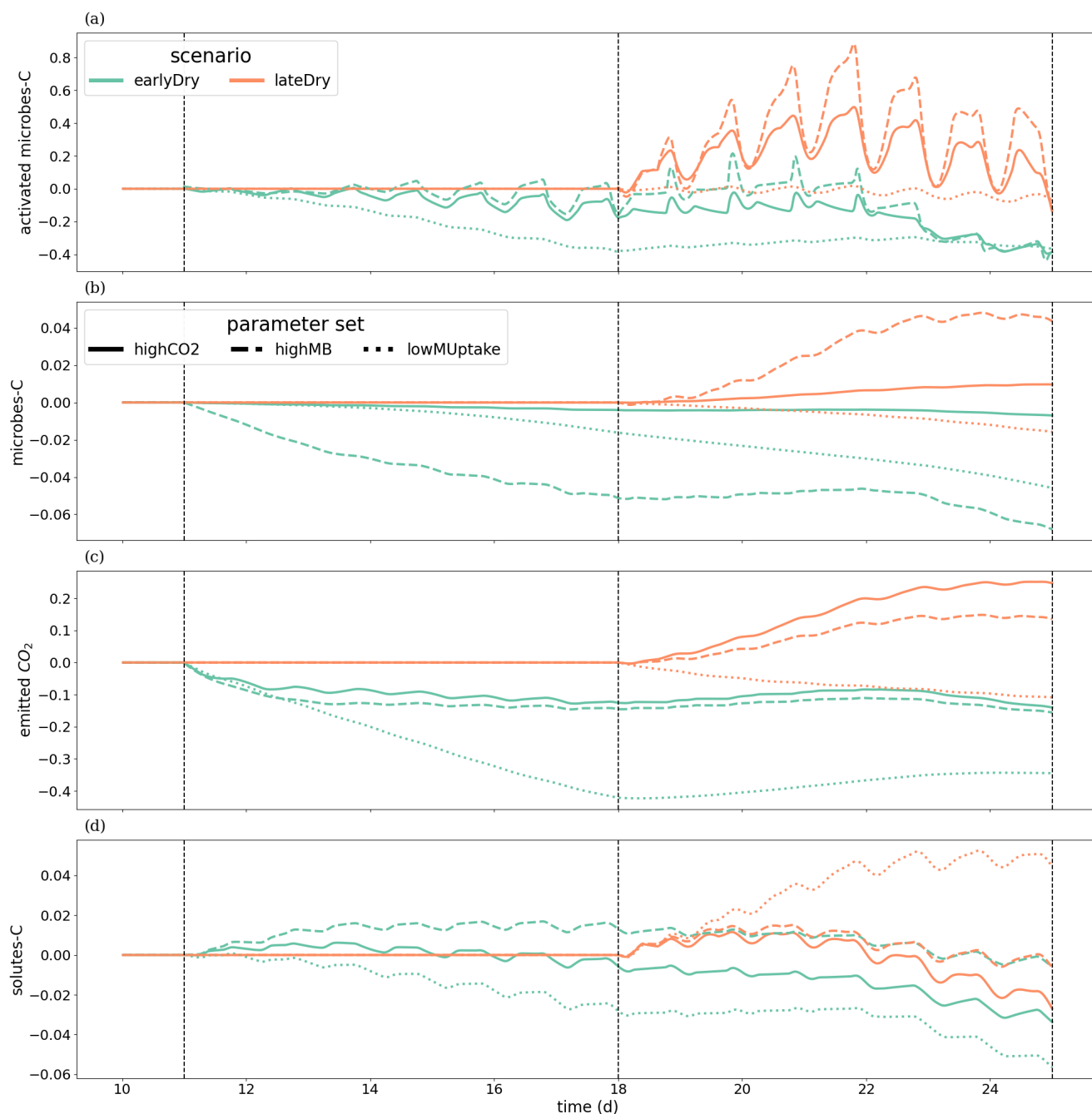


Figure 10. Relative change of root-released carbon use in response to drought scenarios according to the biokinetic parameters at the macroscale.

The panels present the difference of C between each drought treatment and the baseline in relation to the baseline C usage for (a) microbes-C, (b) activated microbes-C, (c) CO₂ emitted by microbes, (d) soil solutes-C. The line types represent the different biokinetic parameterisation. The dotted lines show the beginning and end of the early (day 11 to 18) and late (day 18 to 25) dry spells. Please note that the scales of the y-axis differ in each subplot.



530 3.6 SOC hotspots

To evaluate the root systems' exudation efficiency, Fig. 11 presents the relative volumes of the SOC hotspots (see definition in 2.4.5) in the bulk soil. We observed distinct characteristics over the whole simulation for each biokinetic parameterisation. For *highCO2*, the absolute hotspot volume remained low and decreased with growth (after an initial increase during the dry spells). For *highMB*, the total absolute hotspot volume ($SOC \geq 0.65SOC_{expected}$) peaked in the first half of the simulation before
535 becoming stable under *baseline*. With this biokinetic parameterisation, we observed the portion the relative hotspot volume within the highest class ($SOC \geq 1.16SOC_{expected}$): 8%, 32%, and 29% of the hotspot volume belonged to the highest class under, respectively, *baseline*, *earlyDry*, and *lateDry*. Because of the low microbial activity, we observed the highest relative SOC hotspot volume for *lowMUptake* for all weather scenario: $2.9e-2$, $2.8e-2$, and 0.11 under *baseline*, *earlyDry*, and *lateDry*.

540 Outside of the dry spell, diurnal cycling in the hotspot volume followed the plant C releases during the day and soil C mineralisation without replenishment at night. This dynamic is especially strong with *highCO2* as the hotspot volume is (almost) back to 0 at the end of the day periods. The dry spells buffered the diurnal cycle for all scenarios as the exudation became more stable. Moreover, the biggest hotspot volume and intensity were obtained with the *lateDry* spell, following the higher exudation and mucilage release. *earlyDry* did not lead to a higher total hotspot volume (with $SOC \geq 0.65SOC_{expected}$)
545 for the *highMB* and *lowMUptake* parameterisation at day 25 of growth. However, a bigger portion of the SOC hotspot belonged to the higher hotspot classes ($\geq 0.83SOC_{expected}$ or $\geq 1.16SOC_{expected}$).

For *highCO2* and *highMB*, we observed an increase in hotspot volume during the first half of the dry spells, followed by a decrease during the second half. This can be partly explained by the decrease in daily plant C releases during the second half of the spell. The decreasing SOC hotspot volume in the second half of the spells was also due to the activation and growth of the
550 microbial communities and C utilization after the first strong influx of plant C releases, followed by partial dormancy. Upon the next influx of C (the following day), the microbes reactivated and used the C more quickly. For *lowMUptake*, characterised by its lower microbial activity, we observed a continuous increase in hotspot volume throughout the spells.

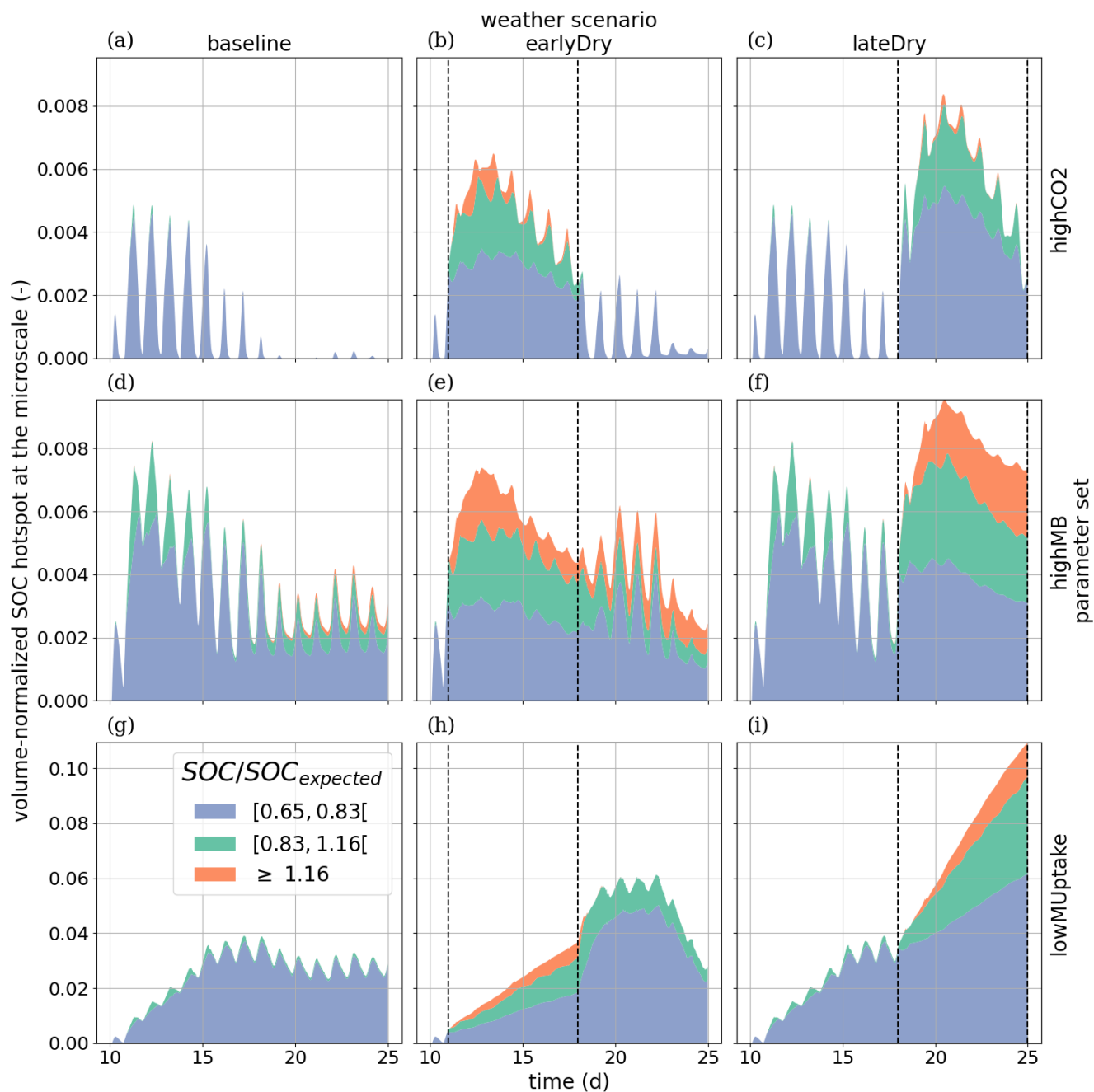


Figure 11. Relative SOC hotspot volume in the perirhizal zone according to time for the three $SOC/SOC_{expected}$ classes. The classes' ranges were defined according to Poeplau and Don (2023). The dotted lines show the beginning and end of the early (day 11 to 18) and late (day 18 to 25) dry spells. The third row is on a scale different from the first and second rows.



3.7 Radial carbon concentration profiles

To analyse how plant-soil system responses to drought affect the carbon stabilisation in the perirhizal zone, Fig. 12 shows the connection between the extent of the microscale domains and dissolved low-weight organic molecules concentrations C_L^l at the end of the simulation. Just as for the bulk soil and perirhizal_{trunc} scales, the highest C_L^l were obtained under *lateDry* for *lowMUptake* and under *baseline* for *highCO2* and *highMB* (see Fig. K1). For *lowMUptake*, microscale domains with shorter outer radii (segment index eight, which is nearer to the root surface) had higher radial concentrations. These shorter outer radii were caused by several microscale domains sharing a single macroscale voxel. Therefore, the higher concentrations underline the additive effect on the C_L^l profile due to proximity to the perirhizal zone, which can indicate an overlap of the rhizospheres. This proximity effect was less noticeable for *highCO2* and *highMB*, where we observed concentration profiles less dependent on the extent of the microscale domain. Indeed, with those biokinetic parameter sets, the microbial C uptake was highest and reacted fastest to high influxes of dissolved low molecular weight organic carbon. Therefore, the C_L^l was closer to an asymptote at the outer boundaries of the 1D domain. These steeper gradients can cause a the rhizosphere extent to be smaller, limiting the rhizosphere overlaps. The effect of rapid microbial C uptake with *highMB* is also visible in Fig. 12(d) and E, where some concentration profiles show lower C_L^l values closer to the root surface, where the concentration of C_C is highest (see Fig. K). The C_L^l radial profiles are strongly linked to the C_C profiles, as presented in appendix K.

The supplementary video "Video S2" shows C_L^l and the corresponding C_C^a/C_C ratios at each time step. We found a high microbial growth during the first pulse of added C followed by a transition to dormancy due to reduced C availability. Microbes remained mostly dormant until reactivated by the next C input pulse while also slowly dying. Reactivation of the microbes during the periods of high C_L^l led to a rapid consumption of the carbon in dissolved low-weight organic molecules near the root surface. As a result, C_L^l became lower than it initially was once the C input pulse diminished—at night (e.g., day 24.69 of growth) and during the second half of the dry spells. We can also observe how, during the dry spells, C_L^l were higher than for the other two scenarios due to lower water content, favouring microbial C uptake.

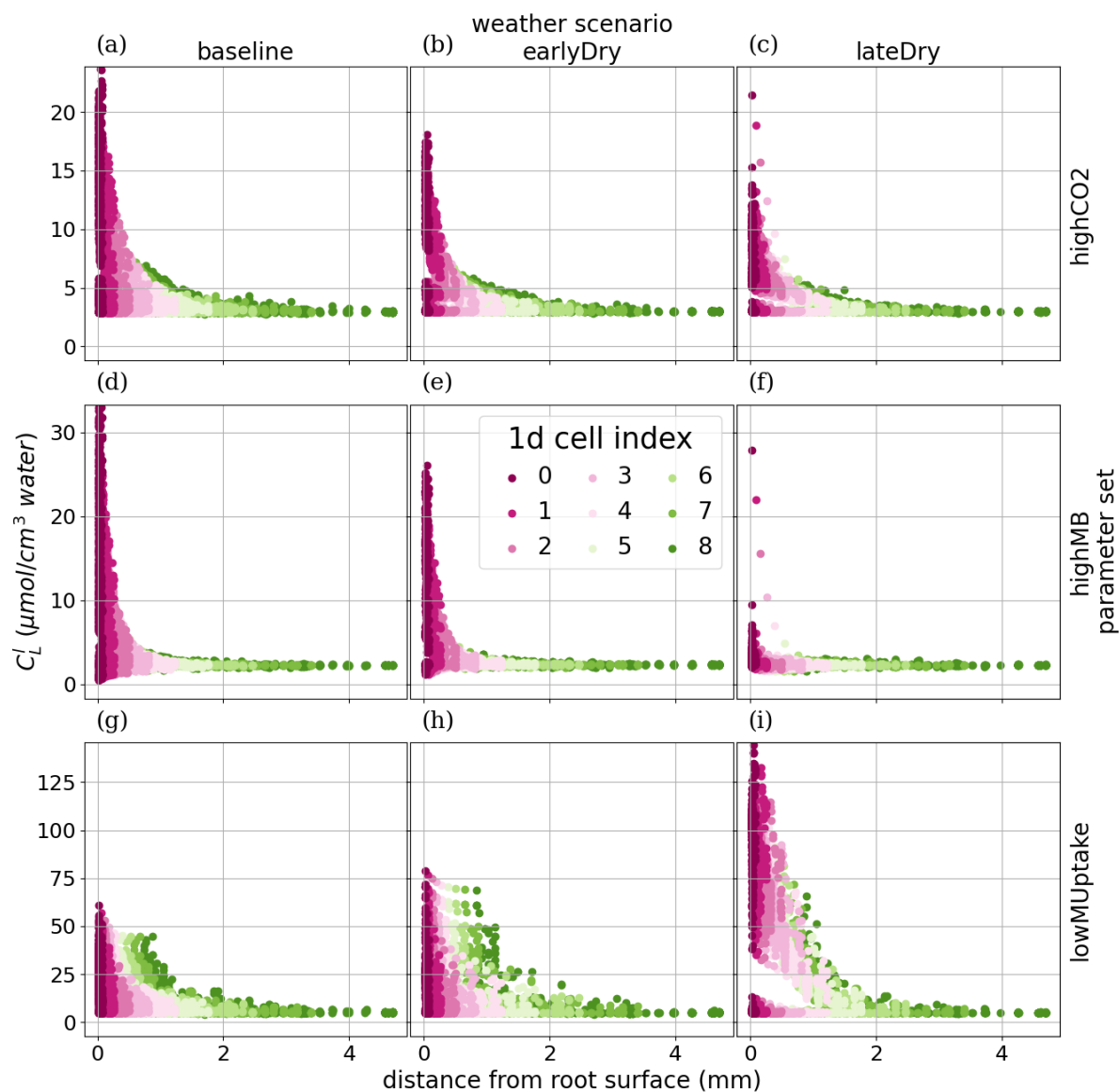


Figure 12. radial concentration profile of carbon from low molecular weight organic compounds at the end of the simulation for each plant perirhizal zone. r (mm) corresponds to the distance to the root surface. The colour gives the segment index of the 1D domain. Each column corresponds to a specific weather scenario and each row corresponds to a specific biokinetic parameterisation.



4 Discussion

4.1 Model setup

Several models have been developed to simulate the root-influenced spatiotemporal distribution of carbon (C) turnover and microbial activity (Pot et al., 2022; Sircan et al., 2025), the exudation from a growing 3D root system (Rees et al., 2023), or the exudation and water uptake by a static plant, based on the C and water balance within the plant and soil (Lacointe and Minchin, 2019; Zhou et al., 2020). Rees et al. (2020) coupled *RhizoDep* with other models on the *OpenAlea* platform to represent the root-soil C and nitrogen exchanges for a growing wheat plant, driven by its inner nitrogen and C balances. Regarding plant-soil coupling for solute flow using FSPMs, several modelling studies have represented the soil as a dynamic environment with water and solute uptake (generally phosphorus) or C releases from a static or growing root system (Ruiz et al., 2021; Schröder et al., 2014; Jorda Guerra et al., 2021; Gérard et al., 2017; Mai et al., 2019; Heppell et al., 2016; Landl et al., 2021a; Schwartz et al., 2016). Braghiere et al. (2020) set up a 3D FSPM accounting for shoot-root-soil interactions for water and C using model coupling. However, their framework did not account for either C flow and microbial reactions in the soil or inner plant water and C balance. Some coupled models also represented inner plant water flow (Schröder et al., 2014; Mai et al., 2019; Schwartz et al., 2016), or root-shoot interactions (Heppell et al., 2016; Braghiere et al., 2020), and Mai et al. (2019) used a sequential implementation of the multi-scale setup. Our framework stands out by coupling of a dynamic whole plant model with a dynamic soil model for both water and C flows (Ruiz et al., 2021; Rees et al., 2018; Schnepf et al., 2022), including biochemical and physical reactions (such as adsorption and the interactions with microbial communities) in the soil domain. The multi-scale framework is a further advantage of this fully open-source setup (Ruiz et al., 2021), increasing the resolution in the soil areas near the root-soil interface to balance accuracy and computing speed. Moreover, the use of fixed-point iteration with implicit time stepping allowed for larger time steps, increasing therefore not only the model accuracy but also its speed for specific scenarios. However, as the simulation of the water flow was the main bottleneck for model convergence, application of the model to more sandy soil will lead to shorter time steps and, therefore, longer computation time. There remains potential for further optimization the code in order to increase its computing speed. Expanding the framework presented by Schnepf et al. (2018b), this coupled model remains flexible, allowing the user to implement only the modules relevant to their research question. The high number of functions represented lead to a high number of parameters. However, several structural plant or root system parameter sets have been established for different species. Moreover analysis of the structural root system module were conducted by Schnepf et al. (2018a) and Morandage et al. (2022). For the soil biokinetics, Sircan et al. (2025) defined a parameter space that fulfills biogeochemical constraints identified from a literature study. They also conducted a sensitivity analysis of the outputs. A user-friendly implementation of the CPlantBox calibration method of Morandage et al. (2021) is currently being developed. Finally, this implementation of TraiRhizo in DuMu^x within CPlantBox sets the building blocks for the simulation of new processes, taking into account solutes such as phosphorus and nitrogen, and the biological, chemical or physical reactions they are subject to.



4.2 Plant processes

In this implementation of the model, we simulated a simplified plant C dynamic compared with the one described in the literature, while still being able to re-create qualitative plant dynamic. Simulation results indicate that plant expansion growth is strongly influenced by changes in water potential during the diurnal cycle and drought periods, consistent with processes described in previous studies (Verbančič et al., 2018; Barillot et al., 2020; Coussement et al., 2018; De Swaef et al., 2022). However, it is hypothesised that cell wall biosynthesis (biosynthetic growth) predominantly occurs during the day using photoassimilates, while being much more limited at night when it relies on starch reserves (Verbančič et al., 2018). Although our simulations did not explicitly separate biosynthetic growth from expansion growth, the parametrization of the plant C module allowed us to qualitatively reproduce these dynamics. For this simulation, the virtual plant's starch pool can be interpreted as representing both actual starch reserves and newly synthesised wall material, thereby enabling expansion growth to occur at night. To achieve robust results and better recreate typical C dynamics across a wider range of parameter sets, it could be beneficial to explicitly represent biosynthetic growth in future models. Following the analyses of Verbančič et al. (2018) and Barillot et al. (2020), high biosynthetic growth requires higher C supply but results in the creation of new cells more flexible and capable of expanding under lower turgor pressure. This higher amount of cells with high cell wall flexibility can help maintain plant growth in case of drought (Blum, 2017). Another mechanism supporting growth under low turgor pressure is osmotic adjustment, which has been identified as a critical process during drought conditions (Blum, 2017; Coussement et al., 2018). Not including this process in our model could explain the high growth limitation caused by drought observed in our simulation.

Regarding the plant's C release, exudation was found to be positively correlated with plant growth (Přikryl and Vančura, 1980; Canarini et al., 2019). In our study, we assumed that exudation occurs only at the growing root tip, making the two correlated on the diurnal- and weekly-scales for a specific weather scenario. However, lower growth allowed more C to be available for exudation, making the two anti-correlated on the hourly scale (day vs. night dynamics) and when comparing dryer against wetter scenarios. Moreover, in experimental studies, a decrease of rhizodeposits was also observed at night (Kuzyakov and Cheng, 2004). This dynamic was particularly strong in our simulations, as we observed no exudation in the middle of the night outside of the dry spell periods. However, we could still recreate qualitative observations made in other studies. Indeed, plants to regulate internal C concentrations and adjust C allocation for growth and maintenance under fluctuating environmental conditions by modulating starch storage (Tixier et al., 2023; Bazot et al., 2005) and C release rates (Prescott et al., 2020; Canarini et al., 2019). The upper range of our exudation rates per unit of root surface ($\approx 0.16 \text{ mmol C cm}^{-2} \text{ d}$) was superior to the averaged rates given in the experimental study of Kravchenko et al. (2004) ($0.018 \text{ mmol C cm}^{-2} \text{ d}$) or Trofymow et al. (1987) ($0.01 \text{ mmol C cm}^{-2} \text{ d}$, as presented by Darrah (1991)). However, we could find similar values in the study of Personeni et al. (2007, Fig3A), due in part to its higher temporal resolution: $\approx 0.68 \text{ mmol C cm}^{-2} \text{ d}$ under high light input and assuming an exuding root tip of 1 cm . The modelling study of Thorpe et al. (2011) for a dwarf bean plant yielded $\approx 0.69 \text{ mmol C cm}^{-2} \text{ d}$, assuming and exuding root tip of 1 cm with radius of 0.02 cm . Moreover, microbial C uptake acted as a C sink and could affect the exudation rate (Canarini et al., 2019). We also observed a change in the type of organic C



released by the plant (in our model, exudation-to-mucilage release ratio) under dry spell (Bazot et al., 2005; Hartmann et al., 2020). In spite of those changes, mucilage remained between 1-10% of exudation, consistent with the observations of Nguyen (2009), and exudation represented between 3-40% of assimilated C (Dilkes et al., 2004; Lynch and Whipps, 1990).

645 Regarding the plant water balance, the outputs of the model differ from that presented by Giraud et al. (2023), in part because of the implementation of the multiscale setup with fixed-point iteration, in part because of the update of the plant parameters, as described in section 2.3.

4.3 Distribution of soil carbon

4.3.1 Spatial and temporal distribution of microbial functional groups

650 Regarding the spatial resolution, we observed a smooth gradient of low-weight dissolved organic molecules-C (C_L^l) along the radial axis for the different biokinetic parametrisation. This suggests that our resolution for the microscale domains is sufficient to represent the C flow in the 1D soil models. For simulations of solutes with low diffusion rates (e.g. phosphorus) and a lower advection (low plant water uptake rate), the root's uptake rate would become strongly dependent on the size of the 1D segment at the root-soil interface. A study could be conducted to evaluate the minimum number of segments necessary

655 to accurately represent the selected soil processes according to the range of expected advection and diffusion rates of solutes under specific scenarios. The output of the simulations showed diverging results according to the studied scales (macroscale, bulk soil, perirhizal_{trunc} and microscale). For instance, compared with the bulk soil scale, the perirhizal_{trunc} scale showed a higher influence of the weather scenarios on the soil C balance. Moreover, the microscale showed a high gradient of the C concentration along the radial coordinate of the 1D domains that could not be represented via the perirhizal_{trunc} scale.

660 These scale-dependent results underline the advantage of using a multi-scale simulation and having a higher precision at the root-soil interface, following the observations of Mai et al. (2019). Moreover, the model showed a strong horizontal and vertical variability in the concentrations, making a 3D evaluation relevant before, for instance, aggregating the results to a 2D or 1D sink term to be used by higher-scales models. As mentioned in the first implementation of the multiscale framework (Mai et al., 2019), the low resolution near the root soil interface (at the *mm* scale) raises the issue of including lower-scale

665 processes, such as the influence of pore size on the water and C balance (Kuppe et al., 2022). As in the study of Landl et al. (2021a), the interactions between the 1D and 3D soil models also allowed us to represent the additive effect of perirhizal zone proximity, which led to higher solute concentration under specific biokinetic parameterisation (*lowMUptake*) and favored C hotspot formation from plant releases. Landl et al. (2021a) also evaluated the influence of root traits on the soil's normalised hotspot volume. Our study complements those findings and shows that root and microbial traits have to be evaluated together,

670 as high concentration of soil organic C can be reached for different exudation rates according to the traits of the microbial community.

Other characteristics of the microbial activity were studied with our model. With the biokinetic parameter sets *highCO2* and *highMB*, we observed a diurnal dynamic of high microbial growth under higher exudation (daytime), leading to a high



675 consumption of C for microbial growth and maintenance. This was followed by microbial dormancy (high dormant-to-total
microbe ratio at nighttime). This dynamic has been observed in the literature and can be described as a "starving-survival
lifestyle", where microbes enter dormancy in a low-nutrient environment and quickly react to new inputs of resources (Hobbie
and Hobbie, 2013). We found a specific reaction to resource scarcity for the parameter set *highMB* with *lateDry*. For this
simulation, we found an especially high copiotroph growth and a high ratio of dormant oligotrophs. This diverging results
680 between the two communities are indicative of a possible intra-microbial competition. This follows over studies where plant
exudation and root growth affected microbial composition (de la Fuente Cantó et al., 2020; Bonkowski et al., 2021). Biokinetic
parameter sets describing more active microbes (*highCO2* and *highMB*) were also linked to a higher usage of soil solutes in case
of higher exudation, when compared with the *baseline* scenarios. This higher usage rate led to a form of "rhizosphere priming
effect" (Bonkowski et al., 2021; Kuzyakov and Cheng, 2004) where the root exudation caused an increase in mineralisation of
685 the pre-existing soil organic matter, leading ultimately to a relatively lower amount of C in the solute pool compared with the
baseline. A more precise evaluation of a possible rhizosphere priming effect could be conducted with this setup, by dividing
each C pool between the C originating from the plant additions and the C already present in the system at the beginning of the
simulation. Our simulation of the microbial dynamic and competition was however limited by not accounting for other stresses
than C and water scarcity, such as nitrogen, phosphorus (Drake et al., 2013; Brown et al., 2022), or oxygen (Wiesenbauer
et al., 2024) scarcity. Likewise, the diurnal aspect of microbial activity would also be better represented by accounting for
690 soil temperature (Kuzyakov and Cheng, 2004). However, over the time period of this study (two weeks), we assumed the
soil temperature varied little. Regarding the spatial distribution of the microbes, the prescribed exudation near the plant root
tips also led to a higher microbial growth in those areas, resulting in a vertical distribution similar to the one observed by
McDougall and Rovira (1970). At the microscale, simulations also resulted in very high concentrations of copiotrophs near the
695 root surface. Although high copiotrophic concentration near the root surface following exudation is expected (Bonkowski et al.,
2021), representing microbial motility (Kuppe et al., 2022; Schnepf et al., 2022) would help smooth these concentration peaks.
Representing motility could also potentially lead to a better representation of the priming effect as the microbes (especially
from mature roots) might diffuse and consume C in areas further away from the root-soil interface (Dupuy and Silk, 2016).

700 4.3.2 Effect of dry spells on carbon stabilisation

The biokinetic parameterisation strongly influenced the effects of the weather scenarios on soil C balance. For more active
biokinetic parameter sets (*highCO2* and *highMB*), the microbial growth was limited by C resources. The higher plant C releases
lateDry had therefore a positive effect on the microbial community. On the contrary, for non-C limited microbial communities
(*lowMUptake* parameter set), the water stress of *lateDry* affected negatively the microbial growth. These opposite reactions
705 influenced how the soil domain was impacted by the short dry spells (see below). The microbial dynamic will have an even
stronger impact on the simulated water and C balance once soil-to-plant feedback mechanisms are implemented, such as
nutrient uptake (de la Fuente Cantó et al., 2020) and organic C-dependent soil hydraulic parameters (Landl et al., 2021b; de la
Fuente Cantó et al., 2020).



Our *earlyDry* and *lateDry* weather scenarios led to a short decrease in soil water content, creating a wetting-drying cycle.

710 According to the meta-analysis of Borken and Matzner (2009), these wetting drying cycles should lead, under specific environmental conditions and microbial communities, to lower microbial respiration during the spells, followed by a respiration pulse once the soil is rewetted. These pulses may or may not compensate for the earlier CO₂ emission decrease (Borken and Matzner, 2009). In our simulation, the early dry spell always led to a decrease in overall emitted microbial CO₂ at the macroscale when compared with the *baseline* scenarios. We then observed in the week following the end of the spell a slight uptick in emitted

715 CO₂ compared with the baseline, which did not compensate the lower earlier emissions. For the later dry spells with *highCO2* and *highMB* parametrisation, the emission pulses occurred during the spells. Indeed, while the drying led to a lower portion of microbes being dormant, the soil water content often remained too high to cause high microbial death or deactivation, especially for soil zones further away from the roots (macroscale). The lower water stress was, therefore, partly compensated by the higher C_L^I . We did not simulate an increase of plant and microbial necromass to be used by the soil microbes at the

720 end of the spell (increasing thus the respiration once the soil is rewetted). Another explanation for the divergence is that we do not represent the easier access to "previously protected organic matter" caused by sudden soil rewetting. Moreover, we represented short dry spells (seven days) while longer spells (two weeks) may be necessary to see stronger effects on the microbial community (Borken and Matzner, 2009). The higher C mineralisation during the drying phase of the later dry spell could also be linked to the method used to represent microbial sensitivity to water stress. Indeed, for simplicity, we did not

725 represent the direct effect of soil water content on the potential microbial death (k_{max}). Moreover, we used the same value to calibrate the sensitivity of copiotrophs and oligotrophs to water stress, although oligotrophs could be assumed to be more resistant to low soil water content. Finally, the water scarcity parameters could be recalibrated using experimental data.

We could reproduce qualitatively processes measured by Deng et al. (2021) for the C balance under limited water resources. Indeed, we observed a decrease in root biomass during the dry spells, with, under some scenarios, an increased exudation.

730 The lower root growth then led to lower plant respiration, while the higher concentration of dissolved organic C under the late dry spell (with *highCO2* and *highMB*) led to a higher microbial respiration by the end of the simulation. Contrary to Deng et al. (2021), we did not observe a decrease in total soil organic C. They linked this decrease to a lower soil C addition from plant residue, which is not represented in our model. Under *earlyDry*, we could observe (limited) differences in concentration compared with the *baseline* seven days after the end of the dry spells, underlining the resilience of the simulated environment,

735 especially for the soil zones nearer the roots. The *lateDry* scenario led to the lowest plant growth but to a higher *SOC* hotspot volume, indicating a more resource-efficient root system exudation. We had, therefore, a trade-off in the C usage strategy.

5 Conclusions

In this paper, we presented the equations and implementation of a coupled model representing the carbon (C) and water flow in the soil-rhizosphere-plant continuum, influenced by the atmospheric conditions via plant transpiration and photosynthesis.

740 This new framework takes into account the effect of the water content variation on the C flow and microbial reactions. Moreover, the multiscale implementation allowed us to evaluate more precisely the water and C flow and reactions at the



soil-plant interface, quantifying the feedback effect of the plant on the soil processes. Thanks to the outputs of the model, we could observe the evolution of variables difficult to measure experimentally at the rhizosphere scale with non-destructive measurements, such as exudation and soil respiration. In our simulation, the effect of dry spells on the soil C balance depended on the time dynamic of the exudation and the characteristics of the microbial community, underlying the site-specific aspect of agricultural practices' effects on the C balance. For instance, compared with the baseline scenarios, dry spells could lead to an increase of C mineralisation with active microbial communities (C-limited) against lower mineralisation for less active microbial communities (water-limited). Adding nutrient (such as nitrogen) flows in the coupled model would be an important extension to represent more accurately the feedback effect of the soil C balance on the plants' development.

6 Code availability

. For this study, we used the plant model CPlantBox (Schnepf et al., 2025b) and the corresponding soil module (Schnepf et al., 2025a). The full setup is available at: [Giraud2025_CarbonStabilisation](#)

7 Video supplement

. A video presenting this graphic for each time step is available in the supplementary documents ("Video S1"). The supplementary video "Video S2" shows C_L^l and the corresponding C_C^a/C_C ratios at each time step.



Appendix A: List of the parameters and variables

Table A1. Represented carbon pools

Output variables	Definition	Unit
C_L^l/C_L^s	Concentration of carbon from compounds with low molecular weight (in the liquid/solid phase)	$mol\ C\ cm^{-3}\ water\ /\$ $mol\ C\ cm^{-3}\ scv$
C_H^l	Concentration of carbon from compounds with high molecular weight	$mol\ C\ cm^{-3}\ water$
$C_O\ (C_O^a, C_O^d)$	Concentration of oligotrophs (active, dormant)	$mol\ C\ cm^{-3}\ scv$
$C_C\ (C_C^a, C_C^d)$	Concentration of copiotrophs (active, dormant)	$mol\ C\ cm^{-3}\ scv$
CO_2	Unit of emitted CO_2 per volume of soil	$mol\ C\ cm^{-3}\ scv$

Appendix B: Soil water flow

In the sections below, we present the implementation of the equations given in section 2.2.2 to the 1D axisymmetric and 3D soil domains.

760 B1 3D soil model

For the 3D macroscale soil model, the sink term of Eq. (6) $S_\theta = S_{w,root-3DS}$ ($cm^3\ water\ cm^{-3}\ scv\ d^{-1}$), the water uptake or release by the roots:

$$S_{w,root-3DS,init} = \frac{1}{V_{3DS,scv}} \sum_{i=1}^{nr} \frac{\partial \theta_i V_{1DS,scv,i}}{\partial t} \quad (B1)$$

$$S_{w,root-3DS} = \text{Lim}(S_{w,root-3DS,init}) \quad (B2)$$

765 where nr (–) is the number of root segments in the soil control space of volume $V_{3DS,scv}$ ($cm^3\ scv$), the i subscript is the identification of the i^{th} root, $V_{1DS,scv,i}$ ($cm^3\ scv$) is the volume of the perirhizal zone i and θ_i its water content. Instead of using $q_{w,root-soil}$ (see Eq. (3)) like Mai et al. (2019), in this study $S_{w,root-3DS}$ is obtained from $\frac{\partial \theta_i V_{1DS,scv,i}}{\partial t}$. This helps avoid computation errors when simulating the macro-soil flows and diminishes the divergence between the macro- and microscale models. Indeed, the plant-prescribed $q_{w,root-soil}$ was already potentially limited during the computation of



Table A2. TraiRhizo input parameters. When the source is not given, the parameter values are taken from the sets defined by Sircan et al. (2025) and selected in section I. HMW: high molecular weight organic carbon compound.

Symbol	Definition (and source)	Value per selected parameter set			Unit
		<i>highCO2</i>	<i>highMB</i>	<i>lowMUptake</i>	
a	Sharpness parameter for the switch function from active to dormancy	0.1			—
$C_{H,init}^l$	Initial concentration of high molecular weight organic carbon concentration	$5.94e^{-4}$	$6.94e^{-4}$	$6.47e^{-4}$	$mol\ C\ cm^{-3}$ <i>water</i>
$C_{L,init}^l$	Initial dissolved low molecular weight organic carbon	$4.71e^{-6}$	$5.15e^{-6}$	$5.1e^{-6}$	$mol\ C\ cm^{-3}$ <i>water</i>
$C_{L,max}^s$	Maximum sorption capacity	$8.9e^{-4}$			$mol\ C\ cm^{-3}$ <i>scv</i>
$C_{thres,C}$	Threshold C_L^l for microbial (de)activation	$1.42e^{-5}$	$9.90e^{-6}$	$2.19e^{-5}$	$mol\ C$
$C_{thres,O}$		$8.58e^{-6}$	$7.71e^{-6}$	$9.76e^{-6}$	$cm^{-3}\ water$
D_{HW}	Diffusion coefficient of high molecular weight organic carbon	$3.456e^{-3}$			$cm^2\ d^{-1}$
D_{LW}	Diffusion coefficient of dissolved low molecular weight organic carbon	2.07	0.92	1.45	$cm^2\ d^{-1}$
k_{ads}	Adsorption rate	$2.7e^{-7}$			$cm^3\ scv$ $mol\ C^{-1}\ d^{-1}$
$k_{d,C}$	Deactivation rate coefficient	2.73	1.49	1.37	d^{-1}
$k_{d,O}$		0.24	4.04	0.11	
k_{des}	Desorption rate	$5e^{-5}$			d^{-1}
$k_{C,S}$	Substrate affinity to dissolved low molecular weight organic C	$4.93e^4$	$1.50e^5$	$7.72e^4$	$mol\ C$
$k_{O,S}$		$1.02e^6$	$1.16e^7$	$9.55e^4$	$cm^{-3}\ scv$
K_L	Half-saturation coefficients of enzymes targeting HMW	$1.98e^{-6}$	$1.02e^{-7}$	$6.23e^{-4}$	$mol\ C\ cm^{-3}$ <i>scv</i>
$k_{max,C}$	Maximum maintenance rate coefficient	$7.07e^{-3}$	$1.38e^{-3}$	$1.46e^{-3}$	d^{-1}
$k_{max,O}$		$2.30e^{-4}$	$6.57e^{-4}$	$1.14e^{-3}$	
$k_{r,C}$	Reactivation rate coefficient	86.3	95.9	54.3	d^{-1}
$k_{r,O}$		1.17	54.9	0.181	
$v_{max,depoly}$	Maximum reaction rate of enzymes targeting HMW	0.108	$1.31e^{-2}$	$1.69e^{-3}$	d^{-1}



Table A2. Continued

Symbol	Definition (and source)	Value per selected parameter set			Unit
		<i>highCO2</i>	<i>highMB</i>	<i>lowMUptake</i>	
Y	Maintenance yield	0.372	$2.54e^{-2}$	0.397	—
Y_C	Growth yield on dissolved low molecular weight organic carbon	$1.08e^{-2}$	0.108	0.422	—
Y_O		$2.43e^{-2}$	0.142	0.896	
α	Empirical parameter determining the curvature of Eq.D10 (Moyano et al., 2013)	1.47			—
β_C	Reduction factor of maintenance requirements in dormant state	$1.64e^{-3}$	$5.13e^{-3}$	$1.09e^{-4}$	—
β_O		0.592	$9.32e^{-2}$	$3.31e^{-2}$	
$\mu_{max,C}$	Maximum growth rate coefficient	0.83	1.42	0.25	d^{-1}
$\mu_{max,O}$		$1.03e^{-2}$	$3.56e^{-2}$	$1.26e^{-2}$	
ρ_L	Proportion of high molecular weight organic carbon formed from dead microbial biomass due to maintenance	$2.16e^{-2}$	0.579	$1.51e^{-2}$	—
ρ_b	Soil bulk density	1.51			$g \text{ mineral soil } cm^{-3} \text{ scv}$
τ	$\tau = \frac{\psi_{m,soil,D2A}}{\psi_{m,soil,A2D}}$, with $\psi_{m,soil,D2A}$ the threshold soil matric potential for microbial activation (Wang et al., 2021)	0.39			—
$\psi_{m,soil,A2D}$	Threshold soil matric potential for microbial deactivation (Wang et al., 2021)	4600			hPa
$\psi_{m,soil,opt}$	Threshold soil matric potential above which water is not limiting for microbial activity (Moyano et al., 2013)	−30			hPa
$\psi_{m,soil,th}$	Threshold soil matric potential below which microbial activity ceases (Moyano et al., 2013)	−158000			hPa
ω_{DA}	Empirical exponent for Eqs.D29,D30 (Wang et al., 2021)	3.38			—



770 $\frac{\partial \theta_i V_{1DS,scv,i}}{\partial t}$ according to $\psi_{x,crit}$ (see Eq. (B12)). We then set a second limitation on the net sink (resp. source) using the maximum potentially available water (resp. space) in the voxel–equal to the water (resp. space) volume at the beginning of the time step and to the maximum amount of water that could be gained (resp. lost) according to the inter-voxel flow at the last time step. The driving equation for the water flow is defined thus at the macroscale (Mai et al., 2019; Koch et al., 2021):

$$\frac{\partial \theta}{\partial t} = K_{sat} \nabla \cdot (\kappa_m (\nabla \psi_{m,3DS} - \nabla \psi_{g,3DS})) + S_{w,root-3DS} \quad \text{for } \Omega \setminus \partial\Omega, t > t_0 \quad (B3)$$

$$775 \quad S_{w,root-3DS} = S_{w,root-3DS,0} \quad \text{at } t = t_0 \quad (B4)$$

A boundary condition completes the model and can represent, for instance, the net gain or loss of water resulting from rainfall and soil evaporation.

B2 1D axisymmetric soil models

Because of the small radii of the microscale domains, we assume that the gravitational gradient along the radial coordinate
780 is negligible compared with the matric potential gradient: $abs(\frac{\partial \psi_{g,1DS}}{\partial r}) \ll abs(\frac{\partial \psi_{m,1DS}}{\partial r})$. We thus get (Debnath, 2005, Eq. 1.10.4):

$$\frac{\partial \theta}{\partial t} = \frac{1}{r} \frac{\partial}{\partial r} (r K_{sat} \kappa_m \frac{\partial \psi_{m,1DS}}{\partial r}) + \frac{1}{r} S_{w,3DS-1DS} \quad (B5)$$

with r (cm) the radial coordinate along the axisymmetric domain, where $r = 0$ corresponds to the center of root segment associated with the microscale soil domain. $r \in [r_{in}, r_{out}]$, with r_{in} (cm) the inner boundary of the domain, corresponding to
785 the root radius, and r_{out} (cm) the outer boundary of the 1D domain.

The water flow at the inner boundary of 1D domain corresponds to $q_{root-soil}$ (see Eq. (3)). $S_{w,3DS-1DS}$ is obtained from the bulk soil water flow. For the segment i in the voxel k :

$$S_{w,1DS-3DS,i} = - \frac{Q_{w,1DS-3DS,i}}{V_{1DS,scv,i}} \quad (B6)$$

$$Q_{w,1DS-3DS,i} = - Q_{w,3DS-3DS,k} \cdot W_w(i, k) \quad (B7)$$

$$790 \quad W_w(i, k) = \begin{cases} \frac{(\theta_s - \theta_i) V_{1DS,scv,i} + Q_{w,root-soil,i} dt}{\sum_j^n (\theta_s - \theta_j) V_{1DS,scv,j} + Q_{w,root-soil,j} dt} & \text{if } Q_{w,3DS-3DS,k} > 0 \\ \frac{(\theta_i - \theta_r) V_{1DS,scv,i} - Q_{w,root-soil,i} dt}{\sum_j^{nr} (\theta_j - \theta_r) V_{1DS,scv,j} - Q_{w,root-soil,j} dt} & \text{else} \end{cases} \quad (B8)$$

$$V_{1DS,scv,i} = \pi (r_{out,i}^2 - r_{in,i}^2) L_{r,i} \quad (B9)$$

$$Q_{w,root-soil,i} = q_{w,root-soil,i} 2\pi r_{in,i} L_i \quad (B10)$$

$Q_{w,3DS-3DS,k}$ (cm³ water d⁻¹) corresponds to the net water change in the sub-control volume caused by the exchange with neighbouring voxels. The second element on the right-hand side of Eq. (B7), $W_w(-)$ is a weighting factor dividing the
795 net water flow between the microscale domains of the macroscale voxel k . W_w is computed from the maximal potentially



available water (resp. space), which is the sum of [a] the net root water release (resp. uptake) over the evaluated period, and [b] the water (resp. air) volume available at the beginning of the evaluated period. In Eq. (B6), the volume of the microscale domain ($V_{1DS,scv}$, cm^3 scv) is used to convert the net water sink from cm^3 $water$ d^{-1} to cm^3 $water$ cm^{-3} scv d^{-1} . $S_{w,1DS-3DS,i}$ is then divided between the 1D segments of the microscale domains using the same weighting method. We obtain the following driving equation for the microscale soil domains (Mai et al., 2019; Koch et al., 2021):

$$r \frac{\partial \theta}{\partial t} = \frac{\partial}{\partial r} (r K_{sat} \kappa_m \frac{\partial \psi_{m,1DS}}{\partial r}) + r S_{w,1DS-3DS} \quad \text{for } r \in]r_{in}, r_{out}[, t > t_0 \quad (B11)$$

$$K_{sat} \kappa_m \frac{\partial \psi_{m,1DS}}{\partial r} = \max(q_{w,root-soil}, K_{sat} \kappa_m \frac{(\psi_{crit,x} - \psi_{m,1DS})}{\Delta r_{root-1DS}}) \quad \text{at } r = r_{in} \quad (B12)$$

$$K_{sat} \kappa_m \frac{\partial \psi_{m,1DS}}{\partial r} = 0 \quad \text{at } r = r_{out} \quad (B13)$$

$$S_{w,3DS-1DS} = S_{w,3DS-1DS,0} \quad \text{at } t = t_0 \quad (B14)$$

with $\psi_{crit,x}$ (hPa) the critical (minimum) xylem water potential. Therefore, if both $\psi_{m,soil}$ and $q_{w,root-soil}$ are low, the realised net water uptake might be more limited than prescribed via $q_{w,root-soil}$.

Appendix C: Soil carbon transport

In the sections below, we present the implementation of the equations given in section 2.2.4 to the 1D axisymmetric and 3D soil domains.

C1 3D soil model

For the 3D macroscale soil domain, S_X can be computed in two ways:

1. If there are no roots in the voxel i ($len(nr_i) = 0$), S_X corresponds to the sources computed at the voxel scale ($S_{X,3DS}$, mol cm^{-3} scv d^{-1}).
2. If there is at least one root in the voxel, S_X corresponds to the sources computed at the microscale ($S_{X,1DS}$, mol cm^{-3} scv d^{-1}).

This method is represented by the following equations:

$$S_X = \begin{cases} \frac{1}{V_{3DS}} \sum_{i=1}^{nr_k} V_{1DS} S_{X,1DS} & \text{if } len(nr_k) > 0 \\ S_{X,3DS} & \text{else} \end{cases} \quad (C1)$$

This allows us to achieve similar results at the micro- and macroscales and to profit from the higher resolution of the microscale models, leading to more accurate results in the soil voxels containing roots. $S_{X,1DS}$ is computed similarly to $S_{w,root-3DS}$ (see Eq. (B1)), by computing the mean C variation rate and limiting the sink according to the C potentially available in the voxel. The driving equation for dissolved low molecular weight organic C is (Mai et al., 2019):



$$\frac{\partial \theta C_L^l}{\partial t} - K_{sat} \nabla \cdot (\kappa_m C_L^l (\nabla \psi_m - \nabla \psi_g)) \quad (C2)$$

$$-\nabla \cdot (D_L(\theta, \phi) \nabla C_L^l) - S_L = 0 \text{ for } \Omega \setminus \partial\Omega, t > t_0,$$

$$C_L^l = C_{L,0}^l, \text{ at } t = t_0 \quad (C3)$$

825 For high molecular weight organic C compounds, we have:

$$\frac{\partial \theta C_H^l}{\partial t} - \nabla \cdot (D_H(\theta, \phi) \nabla C_H^l) - S_H = 0 \quad (C4)$$

$$\text{for } \Omega \setminus \partial\Omega, t > t_0,$$

$$C_H^l = C_{H,0}^l, \text{ at } t = t_0 \quad (C5)$$

For both equation sets, the boundary conditions can be used to represent an input of organic matter in the soil.

830

C2 1D axisymmetric soil models

For 1D axisymmetric microscale soil domains, we get (Mai et al., 2019):

$$\frac{\partial \theta C_X^l}{\partial t} = -\frac{1}{r} \frac{\partial}{\partial r} r C_X^l u_X + \frac{1}{r} \frac{\partial}{\partial r} r (D_X(\theta, \phi) \frac{\partial C_X^l}{\partial r}) + S_X + S_{1DS-3DS,X} \quad (C6)$$

$S_{1DS-3DS,X}$ represents the net source of solutes from inter-voxel exchanges at the macroscale. For the segment i in the

835 voxel k :

$$S_{1DS-3DS,X,i} = -\frac{Q_{X,1DS-3DS,i}}{V_{1DS,scv,i}} \quad (C7)$$

$$Q_{X,1DS-3DS,i} = -Q_{X,3DS-3DS,k} W_X(i, k) \quad (C8)$$

$$W_X(i, k) = \begin{cases} \frac{m_{X,pot,i}}{\sum_j^n m_{X,pot,j}} & \text{if } Q_{X,3DS-3DS,k} < 0 \\ \frac{1/\max(m_{X,pot,i}, \epsilon)}{(\sum_j^n 1/\max(m_{X,pot,j}, \epsilon))} & \text{else} \end{cases} \quad (C9)$$

$$m_{X,pot,i} = \theta_i V_{1DS,scv,i} C_{X,i}^l + Q_{X,root-soil,i} dt \quad (C10)$$

$$840 \quad Q_{X,root-soil,i} = 2\pi r_{in,i} L_i \cdot \begin{cases} q_{exud,i} & \text{if } X \text{ is } C_L^l \\ q_{mucil,i} & \text{if } X \text{ is } C_H^l \end{cases} \quad (C11)$$

$m_{X,pot}$ ($mol\ C$) is the potentially available solute content. $Q_{X,3DS-3DS,k}$ ($mol\ C/d$) corresponds to the net solute transport into the sub-control volume from other soil voxels. The second element of Eq. (C8) is a weighting factor dependent on the solute content of the microscale domains in the voxel. $V_{1DS,scv,i}$ is used to convert the net solute transport from $mol\ d^{-1}$ to $mol\ cm^{-3}\ d^{-1}$. For solutes we could have $m_{X,pot} = 0$, we, therefore, set a minimum value of $\epsilon \approx 0$ when using $C_{X,pot}^q^{-1}$ to

845 avoid a division by 0. The same method is used to divide the net sinks between the 1D segments of the microscale domain.



Eq. (C6) for dissolved low molecular weight organic C gives:

$$\begin{aligned} r \frac{\partial \theta C_L^l}{\partial t} - \frac{\partial}{\partial r} (r C_L^l K_{sat} \kappa_m(S_w) \frac{\partial \psi_m}{\partial r}) \\ - \frac{\partial}{\partial r} r (D_L(\theta, \phi) \frac{\partial C_L^l}{\partial r}) \\ - r (S_L + S_{1DS-3DS,L}) = 0 \text{ for } \Omega \setminus \partial\Omega, t > t_0, \end{aligned} \quad (C12)$$

$$850 \quad K_{sat} \frac{\partial}{\partial r} \left(\kappa_m C_L^l \frac{\partial \psi_m}{\partial r} \right) + \frac{\partial}{\partial r} (D_L(\theta, \phi) \frac{\partial C_L^l}{\partial r}) = q_{exud,1DS-root} \text{ for } r = r_{in}, \quad (C13)$$

$$K_{sat} \frac{\partial}{\partial r} \left(\kappa_m C_L^l \frac{\partial \psi_m}{\partial r} \right) + \frac{\partial}{\partial r} (D_L(\theta, \phi) \frac{\partial C_L^l}{\partial r}) = 0 \text{ for } r = r_{out}, \quad (C14)$$

$$C_L^l = C_{L,0}^l, \text{ at } t = t_0 \quad (C15)$$

855 Eq. (C6) for high molecular weight organic C compounds gives:

$$\begin{aligned} r \frac{\partial \theta C_H^l}{\partial t} - \frac{\partial}{\partial r} r (D_H(\theta, \phi) \frac{\partial C_H^l}{\partial r}) \\ - r (S_H + S_{1DS-3DS,H}) = 0 \text{ for } \Omega \setminus \partial\Omega, t > t_0, \end{aligned} \quad (C16)$$

$$\frac{\partial}{\partial r} (D_H(\theta, \phi) \frac{\partial C_H^l}{\partial r}) = q_{mucil,1DS-root} \text{ for } r = r_{in}, \quad (C17)$$

$$\frac{\partial}{\partial r} (D_H(\theta, \phi) \frac{\partial C_H^l}{\partial r}) = 0 \text{ for } r = r_{out}, \quad (C18)$$

$$860 \quad C_H^l = C_{H,0}^l, \text{ at } t = t_0 \quad (C19)$$

The solute transport at the inner boundary of the domain corresponds to the exchange with the root (q_{exud} or q_{mucil} , see Eq. (16), (20)).

Appendix D: Soil reactions and microbial pools

865 Microorganisms can be modeled as a system of ordinary differential equations in time, (Pot et al., 2022), representing the to SOC mineralisation and CO₂ release caused by microbes (Pagel et al., 2020). We can describe the microbial behaviour by looking at community-level microbial traits (Bardgett and Caruso, 2020): recent studies indicate that soil bacterial communities are dominated by relatively few taxa with strong environmental preferences. Therefore a focus on the functional traits of dominant taxa can improve our understanding.

870 The equations in this section were adapted from the ones setup by Sircan et al. (2025). They present the microbe-driven soil reactions. The microbial community is divided in two main groups: oligotrophs (slower development and higher substrate affinity) and copiotrophs (quicker development and lower substrate affinity). The main differences with the equations presented by Sircan et al. (2025) are the explicit representation of the soil water content and its influence on microbial processes, and the non-instantaneous C sorption. We present below the list of reactions which sum up to $S_{microbe,X}$ for the organic C



concentration of dissolved low molecular weight concentration (C_L^l) and high molecular weight compounds (C_H^l), as well
875 as the connected microbial pools:

$$S_{microbe,L} = S_{depoly} + (1 - p_L)S_{decay} - S_{growth,L} - S_{Muptake,L} \quad (D1)$$

$$S_{microbe,H} = -S_{depoly} + p_L S_{decay} \quad (D2)$$

with S_{depoly} the depolymerisation rate of high molecular weight organic C compounds, S_{decay} the solute gain from microbial decay, $S_{growth,S}$ the dissolved low molecular weight organic C uptake for microbial growth, and $S_{Muptake,L}$ the dissolved
880 low molecular weight organic C uptake for maintenance (all in $mol\ C\ C^{-3}\ scv\ d^{-1}$). p_L (mol/mol) is the proportion of high molecular weight organic C compounds to total C compounds formed from dead microbial biomass due to maintenance.

The reaction rates are dependent on the concentration of microbial pools. Like Pagel et al. (2020), we define four microbial pools in the solid, described by their C concentration in the soil phase C_Z^Y ($mol\ C\ microbes/cm^3\ scv$). Y stands either for a (active microbes) or d (dormant microbes). Z stands for O (oligotrophes) or C (copiotrophes).

885 We define their respective variation thus:

$$\frac{\partial C_O^a}{\partial t} = S_{growth,O} - S_{deact,O} + S_{react,O} - \frac{1}{Y_M} S_{Mdecay,O}^a \quad (D3)$$

$$\frac{\partial C_O^d}{\partial t} = S_{deact,O} - S_{react,O} - \frac{1}{Y_M} S_{Mdecay,O}^d \quad (D4)$$

$$\frac{\partial C_C^a}{\partial t} = S_{growth,C} - S_{deact,C} + S_{react,C} - \frac{1}{Y_M} S_{Mdecay,C}^a \quad (D5)$$

$$\frac{\partial C_C^d}{\partial t} = S_{deact,C} - S_{react,C} - \frac{1}{Y_M} S_{Mdecay,C}^d \quad (D6)$$

890 $S_{growth,Z}$ corresponds to the growth of C_Z^a , $S_{decay,Z}^Y$ corresponds to the decay of $C_Z^{Y,s}$, $S_{deact,Z}$ represents the switch of C_Z^a to C_Z^d and $S_{react,Z}$ represents the switch of C_Z^d to C_Z^a . $S_{Mdecay,Z}^Y$ represents the loss of $C_Z^{Y,s}$ C because of maintenance. All rates are in $mol\ C\ cm^{-3}\ scv\ d^{-1}$. Y_M (–) is the maintenance yield. The growth reaction rates are defined thus:

$$S_{growth,L} = \frac{1}{Y_O} S_{growth,O} + \frac{1}{Y_C} S_{growth,C} \quad (D7)$$

$$S_{growth,O} = f_A(\psi_{m,soil}) \frac{\mu_{max,O} C_L^l k_{O,L}}{\mu_{max,O} + C_L^l k_{O,L}} C_O^a \quad (D8)$$

$$895 \quad S_{growth,C} = f_A(\psi_{m,soil}) \frac{\mu_{max,C} C_L^l k_{C,L}}{\mu_{max,C} + C_L^l k_{C,L}} C_C^a \quad (D9)$$

$$f_A(\psi_{m,soil}) = \begin{cases} 1, & \psi_{m,soil} > \psi_{m,soil,opt} \\ 1 - \left(\frac{\log_{10}(\psi_{m,soil}/\psi_{m,soil,opt})}{\log_{10}(\psi_{m,soil,th}/\psi_{m,soil,opt})} \right)^\alpha, & \psi_{m,soil} \in [\psi_{m,soil,th}, \psi_{m,soil,opt}] \\ 0, & \psi_{m,soil} < \psi_{m,soil,th} \end{cases} \quad (D10)$$

With Y_Z (–) the growth yield of C_Z . $\mu_{max,Z}$ ($1/d$) is the maximum growth rate of C_Z^a . $k_{O,L}$ ($cm^3\ scv\ d\ mol^{-1}\ C$) is the C_Z^a affinity to C_L^l . $f_A(\psi_{m,soil})$ (–) defines the water limitation on the access of the microorganisms and enzymes to the solutes



(Moyano et al., 2013). The maintenance decay rates are defined thus:

$$900 \quad S_{Mdecay} = S_{Mdecay,O}^a + S_{Mdecay,O}^d + S_{Mdecay,C}^a + S_{Mdecay,C}^d \quad (D11)$$

$$S_{Mdecay,O}^a = k_{max,O} \overline{C_O^a} - S_{Muption,L,O}^a \quad (D12)$$

$$S_{Mdecay,O}^d = k_{max,O} \beta_O C_O^d - S_{Muption,L,O}^d \quad (D13)$$

$$S_{Mdecay,C}^a = k_{max,C} \overline{C_C^a} - S_{Muption,L,C}^a \quad (D14)$$

$$S_{Mdecay,C}^d = k_{max,C} \beta_C C_C^d - S_{Muption,L,C}^d \quad (D15)$$

$$905 \quad \overline{C_O^a} = \max(0, C_O^a - C_{O,lim}^a) \quad (D16)$$

$$\overline{C_C^a} = \max(0, C_C^a - C_{C,lim}^a) \quad (D17)$$

$k_{max,Z}$ (1/d) is the maximum maintenance rate coefficient for C_Z . β_Z (–) is the reduction factor of maintenance requirements in dormant state for C_Z . $C_{Z,lim}^a$ (mol C/cm³ scv) corresponds to the minimal value of C_Z^a below which the microbial pool can only be subjected to growth. This limitation allows us to have a re-development of the pool even if we have no solute in
910 the soil for a period of time. We use consequently the limited $\overline{C_Z^a}$ (mol C/cm³ scv) value for all reaction rates except for $S_{growth,Z}$. The uptake rates are defined thus:

$$S_{uptake,L} = S_{uptake,L,O}^a + S_{uptake,L,O}^d + S_{uptake,L,C}^a + S_{uptake,L,C}^d \quad (D18)$$

$$S_{uptake,L,O}^a = f_A(\psi_{m,soil}) \frac{k_{max,O} C_L^l k_{O,L}}{k_{max,O} + C_L^l k_{O,L}} \overline{C_O^a} \quad (D19)$$

$$S_{uptake,L,O}^d = f_A(\psi_{m,soil}) \frac{k_{max,O} C_L^l k_{O,L}}{k_{max,O} + C_L^l k_{O,L}} \beta_O C_O^d \quad (D20)$$

$$915 \quad S_{uptake,L,C}^a = f_A(\psi_{m,soil}) \frac{k_{max,C} C_L^l k_{C,L}}{k_{max,C} + C_L^l k_{C,L}} \overline{C_C^a} \quad (D21)$$

$$S_{uptake,L,C}^d = f_A(\psi_{m,soil}) \frac{k_{max,C} C_L^l k_{C,L}}{k_{max,C} + C_L^l k_{C,L}} \beta_C C_C^d \quad (D22)$$



The deactivation and reactivation rates are defined thus:

$$S_{deact,O} = \max((1 - \phi_O), f_{A2D}(\psi_{m,soil}))k_{d,O}\overline{C_O^a} \quad (D23)$$

$$S_{deact,C} = \max((1 - \phi_C), f_{A2D}(\psi_{m,soil}))k_{d,C}\overline{C_C^a} \quad (D24)$$

$$920 \quad S_{react,O} = \min(\phi_O, f_{D2A}(\psi_{m,soil}))k_{r,O}C_O^d \quad (D25)$$

$$S_{react,C} = \min(\phi_C, f_{D2A}(\psi_{m,soil}))k_{r,C}C_C^d \quad (D26)$$

$$\phi_O = \frac{1}{e^{\frac{C_{thres,O}^l - C_L^l}{aC_{thres,O}^l}} + 1} \quad (D27)$$

$$\phi_C = \frac{1}{e^{\frac{C_{thres,C}^l - C_L^l}{aC_{thres,C}^l}} + 1} \quad (D28)$$

$$f_{A2D}(\psi_{m,soil}) = \frac{1}{1 + [\psi_{m,soil,A2D}/\psi_{m,soil}]^{\omega_{DA}}} \quad (D29)$$

$$925 \quad f_{D2A}(\psi_{m,soil}) = \frac{1}{1 + [\psi_{m,soil}/(\tau \psi_{m,soil,A2D})]^{\omega_{DA}}} \quad (D30)$$

with $k_{d,Z}$ and $k_{r,Z}$ (1/d) respectively the deactivation and reactivation rate coefficients for C_Z . $C_{thres,Z}^l$ (mol C/cm³ water) is the C_L^l threshold for ϕ_Z . ϕ_Z (–) is the switch function defining the effect of C_L^l on microbial dormancy ($S_{deact,Z}$ and $S_{react,Z}$), while f_{A2D} and f_{D2A} (–) define the effect of soil water content (see Wang et al. (2021)). The increase of the deactivation (resp. decrease of the activation) is defined by the most limiting resource between dissolved low molecular weight organic C and water. For instance, when water limiting for microbial activation, we will have $\min(\phi_Z, f_{D2A}(\psi_{m,soil})) = f_{D2A}(\psi_{m,soil})$ or $\max((1 - \phi_Z), f_{A2D}(\psi_{m,soil})) = f_{A2D}(\psi_{m,soil})$. Finally, we get the depolymerisation rate (Pagel et al., 2020):

$$S_{depoly} = f_A(\psi_{m,soil})v_{max,depoly}\frac{C_H^l}{K_L + C_H^l}\overline{C_O^a} \quad (D31)$$

With $v_{max,depoly}$ (1/d) is the maximum reaction rate of enzymes targeting high molecular weight organic C compounds, K_L (mol/cm³ water) half-saturation coefficients of enzymes targeting high molecular weight organic C compounds.

935 From the reactions defined above, we also get C_{co2} (mol C/cm³ scv), the amount of C released:

$$\frac{\partial C_{co2}}{\partial t} = \frac{1 - Y_O}{Y_O}S_{growth,O} + \frac{1 - Y_C}{Y_C}S_{growth,C} + \frac{1 - Y_M}{Y_M}S_{Mdecay} + S_{Muptake,L} \quad (D32)$$

Although we do compute the amount of C released, we do not simulate its transport in the domain.

Appendix E: Growth of existing 1D axisymmetric soil models

Once the 1D domain volumes at time step N have been computed (see Eq. (26)), the redistribution of the water and C between
940 the microscale domains of a voxel are done in 2 steps:

1. Compute the new water volume and solute content in the pre-existing microscale domains that have shrunk while trying to maintain the radial concentration gradients.



2. Compute the water volume and C content of the new microscale domains and of the pre-existing microscale domains that have grown. We define for each voxel a mean water content and C concentration from the leftover water volume, C content, and voxel space. There is no concentration gradient in the newly added microscale space.

We set m_X (mol) as the content of the C element X with the concentration C_X , and V_w (cm^3 water) the water volume.

E1 Shrinking 1D axisymmetric soil models

For perirhizal zone with a volume decrease between time step $N - 1$ and N , we adapt m_X in each soil voxel so that, for the segment k :

$$\text{ChangeRatio}S_k = \frac{m_{x,k}^N}{m_{X,k}^{N-1}}$$

$$\text{ChangeRatio}W_k = \frac{V_{w,k}^N}{V_{w,k}^{N-1}}$$

We set $\text{ChangeRatio}S$ and $\text{ChangeRatio}W$ so that the microscale domain will lose or gain water and solute according to the volume change. $\text{ChangeRatio}W$ is also adapted to keep $\theta \in [\theta_{\text{wiltingpoint}}, \theta_s]$. $\theta_{\text{wiltingpoint}}$ is the soil water content when $\psi = \psi_{\text{crit}}$ the critical plant water potential. Consequently:

$$\text{ChangeRatio}S_k = \min\left(\frac{V_{1DS,scv,k}^N}{V_{1DS,scv,k}^{N-1}}, 1\right) \quad (\text{E1})$$

$$\text{ChangeRatio}W_k = \max\left(\min\left(\text{ChangeRatio}S_k, \frac{\theta_s V_{1DS,scv,k}^N}{V_{w,k}^{N-1}}\right), \frac{\theta_{\text{wiltingpoint}} V_{1DS,scv,k}^N}{V_{w,k}^{N-1}}\right) \quad (\text{E2})$$

We also want to keep the radial concentration gradients:

$$\frac{\partial C_k^N}{\partial r} = \frac{\partial C_k^{N-1}}{\partial r} \quad (\text{E3})$$

$$\frac{\partial \theta_k^N}{\partial r} = \frac{\partial \theta_k^{N-1}}{\partial r} \quad (\text{E4})$$

For the discretised microscale domain made of n segments, this gives us a set of equations that can be solved analytically. In matricial form:

$$\mathcal{B} = Q^{-1}G \quad (\text{E5})$$



960 With Q a matrix of size $[n, n]$:

$$Q = \begin{bmatrix} -1 & 1 & 0 & \dots & 0 \\ 0 & -1 & 1 & \dots & 0 \\ 0 & \dots & \dots & \dots & 0 \\ 0 & \dots & \dots & -1 & 1 \\ V_{0,k}^N & V_{1,k}^N & \dots & V_{n-1,k}^N & V_{n-1,k}^N \end{bmatrix} \quad (E6)$$

And G an array of size n :

$$G = \begin{bmatrix} b_{r_{1,k}}^{N-1} - b_{r_{0,k}}^{N-1} \\ \dots \\ \dots \\ b_{r_{n,k}}^{N-1} - b_{r_{n-1,k}}^{N-1} \\ B_k^{N-1} \text{ChangeRatio}_k^N \end{bmatrix} \quad (E7)$$

965 B_k^N is the total amount of the solute or of water (in mol or cm^3) and b is the solute concentration or water content. The last lines of G and Q assure that we obtain the correct total solute and water amount, the other lines represent the wished for gradient between the new location of the segment centers. The value of $b_{r_{1,k}}^{N-1} - b_{r_{0,k}}^{N-1}$ give the changes of b (at $N - 1$) between the segment centers (distance at N). It is obtained by interpolation of the concentration gradients between the segments centers at the end of time step $N - 1$.

970 $ChangeRatioW_k$ and $ChangeRatioS_k$ ensure that the overall θ and m_k in the whole microscale domain remains within the needed range, but not for each segment. Consequently, when implementing the new water value for each microscale segment, we adapt the distribution of the water between the segments to have for each segment $\theta \in [\theta_{wiltingpoint}, \theta_s]$. Likewise, we ensure that $\min(m_k) \geq 0$.

This yields $C_{1DS}^{N,0,-1}$ and $\theta_{1DS}^{N,0,-1}$ to be used at the beginning of the next fixed point loop iteration, see section F.

E2 New and expanding 1D axisymmetric soil models

975 From the concentration of the existing microscale domains per voxel, we compute the mean θ_{new} and C_{new} , the water and concentration in the newly freed soil space. θ_{new} and C_{new} will define the initial conditions of the added volume in the expanding or new microscale domains. For this, we compute the total volume of the newly freed volume in the voxel ($V_{3DS,scv,leftover}^N, cm^3$):

$$V_{3DS,scv,i,leftover}^N = \sum_j^{nr_{shrunk,i}^N} L_{j,N} \pi (r_{out,j}^N{}^2 - r_{in,j}^2) \quad (E8)$$



980 with $nr_{shrunk,i}^N$ the sets of microscale domains in voxel i that have shrunk at time step N . We then get the content of water and C that are not in the old microscale domains of voxel i anymore:

$$V_{3DS,w,i,leftover}^N = \sum_j^{nr_{shrunk,i}^N} V_{1DS,w,j}^{N-1} - V_{1DS,w,j}^N \quad (E9)$$

$$m_{3DS,X,i,leftover}^N = \sum_j^{nr_{shrunk,i}^N} m_{1DS,X,j}^{N-1} - m_{1DS,X,j}^N \quad (E10)$$

We can then get θ_{new} and C_{new} :

$$985 \quad \theta_{k,new}^N = \begin{cases} \frac{V_{3DS,w,i,leftover}^N}{V_{3DS,scv,i,leftover}^N} & \text{if } len(nr_i^{N-1}) > 0 \\ \frac{V_{3DS,w,i}^{N-1}}{V_{3DS,scv,i}^{N-1}} & \text{else} \end{cases} \quad (E11)$$

$$C_{k,new}^{y,N} = \begin{cases} \frac{X_{i,leftover}^N}{V_{3DS,i,leftover}^N} & \text{if } len(nr_i^{N-1}) > 0 \\ \frac{X_i^{N-1}}{V_{3DS,i}^{N-1}} & \text{else} \end{cases} \quad (E12)$$

$$V_{3DS,i,leftover} = \begin{cases} V_{3DS,w,i,leftover} & \text{if } C^y = C^l \\ V_{3DS,scv,i,leftover} & \text{if } C^y = C^s \end{cases} \quad (E13)$$

$$V_{3DS,i} = \begin{cases} V_{3DS,w,i} & \text{if } C^y = C^l \\ V_{3DS,scv,i} & \text{if } C^y = C^s \end{cases} \quad (E14)$$

We can then add the C and water to the growing microscale domains (the C concentration is null for newly created domains):

$$990 \quad \theta_{1DS}^{N,0,-1} = \theta_{1DS}^{N-1} + \theta_{k,new}^N \Delta V_{1DS,scv,k} \quad (E15)$$

$$C_{1DS}^{N,0,-1} = C_{1DS}^{N-1} + C_{k,new}^N \Delta V_{1DS,scv,k} \quad (E16)$$

We then use the method presented in section E1 to obtain the θ and C_X value for each microscale segment respecting the new content and trying to maintain the old concentration gradients. This yields $C_{1DS}^{N,0,-1}$ and $\theta_{1DS}^{N,0,-1}$ to be used at the beginning of the next fixed point loop iteration, see section F.

995 Appendix F: Pseudo-code of the iterative computation loop

The three models (plant, 1D microscale soil, 3D macroscale soil) are coupled using an iterative approach based on the method Jorda Guerra et al. (2021). In the following section, we present the implementation of the equations defined above, in matricial form and for one time step N . Although the water and C balances are computed together, for clarity, the descriptions of their respective computation loops are presented separately.



1000 F1 Definition of matrices

For the section below, M represents a matrix of size $[ns, nr]$, with ns the number of soil voxels and nr the number of root segments belowground (equal to the number of microscale domains). Other variables include vectors of size nr with root, root-soil interface or microscale soil values (with respectively the subscripts $root, rsi, 1DS$). The root-soil interface corresponds to the 1D segment at the inner boundary of the microscale models. Vectors with the subscript $3DS$ give the macroscale soil values and are of size ns . $V_{V,w}$ (cm^3 water), θ , ψ , C_X and \mathbf{m}_x (mol C), K_{sri} (cm^2 hPa^{-1} d^{-1}) are vectors giving respectively the water volume, water content, water potential, component concentration, component content, and hydraulic conductivity at the soil-root interface. $V_{surf,out}$ (cm^2) is a vector of size nr and $V_{surf,out}[i] = 2\pi r_{out,i} L_{r,i}$, giving the surface at the outer boundary of the perirhizal zone i . Similarly, $V_{surf,in}[i] = 2\pi r_{in,i} L_{r,i}$ gives the surface at the inner boundary. $V_{V,scv,3DS}$ (resp. $V_{V,scv,1DS}$) is a vector of size ns (resp. nr) giving the volume of each voxel (resp. of each microscale domain). The source vector is obtained from $\mathbf{S} = SV_V$ and is thus in cm^3 water d^{-1} or in mol d^{-1} . M_c is a binary matrix. M_c is filled with 0 except for $M_c[i, j] = 1$, when the j^{th} root segment (and corresponding 1D soil domain) is in the i^{th} soil voxel. $V_{hasRoot}$ is a vector of size ns with 1 for the macroscale soil voxels with at least one root and 0 elsewhere. We set:

$$M_{surf,in} = M_c \circ V_{surf,in}$$

with \circ the hadamard product and $M_{surf,in}$ a matrix of size $[ns, nr]$ giving the inner surface of the microscale domain for each soil voxel. $Q_{w,3DS-3DS}$ (cm^3 water d^{-1}), and $Q_{X,3DS-3DS}$ (mol C d^{-1}) are vectors of size ns giving, for all the voxels containing at least one root, the changes in water or C (for a specific component) caused by exchanges with other voxels (i.e., not caused by input from a root or from biochemical reactions). $M_{weight,X}$ is the weight matrices used to divide voxel flows ($Q_{3DS-3DS}$) between the microscale domains in each voxel (see Eq. (B8),(C9))

1005

F2 Fixed point iteration for the water flow

The pseudo-code below presents the implementation of the fixed-point iteration loop for the water flow.



1010

$$(A) \quad L_{root}^N, M_c^N = \mathbf{Growth}(\text{Env}^N, \mathbf{C}_L^{st, N-1}, \psi_x^{N-1})$$

$$M_{surf, in}^N, V_{surf, in}^N, V_{surf, out}^N, \theta_{1DS}^{N, 0, -1}, \psi_{rsi}^{N, 0, -1} =$$

$$\mathbf{Distribute}(L_{root}^N, M_c^N, \theta_{1DS}^{N-1})$$

$$Q_{w, 3DS}^{N, 0, -1} = Q_{w, 3DS}^{N-1}, \theta_{3DS}^{N, 0, -1} = \theta_{3DS}^{N-1} \quad (F1)$$

for n in $\text{range}(\frac{\Delta t}{\delta t})$:

while $\text{any}(\text{err} \dots > \epsilon \dots)$, and $k < k_{max}$:

$$(B) \quad q_{w, root-soil}^{N, n, k}, \psi_x^{N, n, k} = \mathbf{FlowPhoto}(\text{Env}^{N, n}, \psi_{rsi}^{N, n, k-1}) \quad (F2)$$

1015

$$(C) \quad S_{w, 1DS-3DS}^{N, n, k} = -M_{weight, w}^{N, n, k, T} Q_{w, 3DS}^{N, n, k-1} \quad (F3)$$

$$K_{rsi}^{N, n, k}, \theta_{1DS}^{N, n, k}, q_{w, root-soil}^{N, n, k} = \mathbf{Flow}(V_{surf, in}^N q_{w, root-soil}^{N, n, k} \delta t,$$

$$S_{w, 1DS-3DS}^{N, n, k} \delta t, \theta_{1DS}^{N, n, k-1}, V_{V, scv, 1DS}^N) \quad (F4)$$

$$S_{w, 3DS}^{N, n, k} = M_{surf, in}^N q_{w, root-soil}^{N, n, k, limited} \quad (F5)$$

$$(D) \quad \theta_{3DS}^{N, n, k}, Q_{w, 3DS}^{N, n, k} = \mathbf{Flow}(S_{w, 3DS}^{N, n, k} \delta t, \theta_{3DS}^{N, n, k-1}, V_{V, scv, 3DS}^N) \quad (F6)$$

1020

$$(E) \quad \text{errW}_{1DS, 3DS, cumul}^{N, n, k} = \mathbf{Err}(M_c[\theta_{1DS}^{N, n, k} V_{V, scv, 1DS}^N -$$

$$[\theta_{3DS}^{N, n, k} V_{V, scv, 3DS}^N]) \quad (F7)$$

$$\text{errW}_{1DS, 3DS}^{N, n, k} = \text{errW}_{1DS, 3DS, cumul}^{N, n, k} - \text{errW}_{1DS, 3DS, cumul}^{N, n-1} \quad (F8)$$

$$\text{errW}_{k, k-1} = \mathbf{Err}(X^{N, n, k} - X^{N, n, k-1}) \quad (F9)$$

$$\text{errW}_{qroot} = \mathbf{Err}(q_{w, root-soil}^{N, n, k, limited} - q_{w, root-soil}^{N, n, k}) \quad (F10)$$

1025

$$\text{errW}_{mass1DS} = \mathbf{Err}(\theta_{1DS}^{N, n, k} V_{V, scv, 1DS}^N - [\theta_{1DS}^{N, n, IC} V_{V, scv, 1DS}^N +$$

$$(V_{surf, in}^N q_{w, root-soil}^{N, n, k} + S_{w, 1DS-3DS}^{N, n, k} S_{w, 1DS-1DS}^{N, n, k}) \Delta t]) \quad (F11)$$

$$\text{errW}_{mass3DS} = \mathbf{Err}(\sum_{segments} (\theta_{3DS}^{N, n, k} V_{V, scv, 3DS}^N - [\theta_{3DS}^0 V_{V, scv, 3DS}^N$$

$$+ \sum_j^N (M_{surf, in}^j q_{w, root-soil}^j \delta t^j)]) \quad (F12)$$

$$\text{assert } \text{err} \dots \leq \epsilon \dots \quad (F13)$$

1030

$$\psi_{rsi}^{N, n+1, -1} = \psi_{rsi}^{N, n, k}, \theta_{1DS}^{N, n+1, -1} = \theta_{1DS}^{N, n, k}$$

$$Q_{w, 3DS}^{N, n+1, -1} = Q_{w, 3DS}^{N, n, k}, \theta_{3DS}^{N, 0, -1} = \theta_{3DS}^{N-1} \quad (F14)$$

N (resp. Δt) is the step index (resp. time step) of the whole computation loop and n (resp. δt) is the step index (resp. time step) of the fixed point iteration. k is the iteration number of the fixed point iteration and k_{max} the maximum amount of iteration allowed. Env represents other environmental conditions, L_{root} (cm) is a vector which contains the length of each root segment (and thus microscale domain).

1035



The T superscript gives the transpose of a matrix. **Flow** represents a function computing the water flow and **FlowPhoto** the coupled plant water flow and photosynthesis. **Distribute** corresponds to the division of the voxel volume and water between the microscale domains according to the methods presented in section 2.2.6. $err_{1DS,3DS,cumul}$ gives the difference between the water content values computed at the micro- and macroscale and $err_{1DS,3DS}$ the difference added at the last time step. err_{root} is the difference between the root water uptake rates computed by the plant and the microscale soil. err_{mass} gives the mass balance error, $err_{k,k-1}$ the output differences between the last two iterations (non-convergence). **Err** is a function to sum and normalise the error. $err_{...}$ corresponds to each of the errors computed within the iteration loop, and $\epsilon_{...}$ is their respective maximum value allowed.

F3 Fixed point iteration for the solutes transport

The pseudo-code below presents the implementation of the fixed-point iteration loop for the C transport.



$$(A) \quad L_{root}^N, M_c^N, q_{X,root-soil}^N, C_{X,root}^{st,N} = \mathbf{Growth} \circ \mathbf{TransportReac}(\text{Env}^N, \sum_j^n (A_n^{N-1,j} \delta t^{N,j}), C_{X,rsi}^{N-1}) \quad (F15)$$

$$M_{surf,in}^N, V_{surf,in}^N, V_{surf,out}^N, C_{X,1DS}^{N,0,-1} = \mathbf{Distribute}(L_{root}^N, M_c^N, C_{X,1DS}^{N-1}) \quad (F16)$$

$$Q_{X,3DS}^{N,0,-1} = Q_{X,3DS}^{N-1}, C_{X,3DS}^{N,0,-1} = C_{X,1DS}^{N-1} \quad (F17)$$

for n in range($\frac{\Delta t}{\delta t}$):

while any($\text{err}_{...} > \epsilon_{...}$), and $k < k_{max}$:

$$(B) \quad q_{X,root-soil}^{N,n,k}, A_n^{N,n,k} = \mathbf{TransportPhoto}(\text{Env}^{N,n}, \psi_{rsi}^{N,n,k-1}) \quad (F18)$$

$$(C) \quad \mathbf{S}_{X,1DS-3DS}^{N,n,k} = -M_{weight,X}^{N,n,k,T} Q_{X,3DS}^{N,n,k-1} \quad (F19)$$

$$C_{X,1DS}^{N,n,k}, \mathbf{m}_{X,1DS}^{N,n,k} = \mathbf{TransportReac}(V_{surf,in}^N q_{X,root-soil}^N \delta t, \mathbf{S}_{X,1DS-3DS}^{N,n,k} \delta t, C_{X,1DS}^{N,n,k}, \theta_{1DS}^{N,n,k}) \quad (F20)$$

$$\mathbf{S}_{X,3DS}^{N,n,k} = M_c^N ((\mathbf{m}_{X,1DS}^{N,n,k} - \mathbf{m}_{X,1DS}^{N,n-1})/\delta t + \mathbf{S}_{X,1DS-3DS}^{N,n,k}) \quad (F21)$$

$$(D) \quad C_{X,3DS}^{N,n,k}, Q_{X,3DS}^{N,n,k} = V_{hasRoot} \mathbf{Transport}(\mathbf{S}_{X,3DS}^{N,n,k} \delta t, \mathbf{C}_{X,3DS}^{N,n-1}) + (1 - V_{hasRoot}) \mathbf{TransportReac}(\mathbf{C}_{X,3DS}^{N,n-1}) \quad (F22)$$

$$(E) \quad \text{errC}_{1DS,3DS,cumul} = \mathbf{Err}(M_c^N \mathbf{m}_{x1DS}^{N,k} - \mathbf{m}_{x3DS}^{N,k}) \quad (F23)$$

$$\text{errC}_{1DS,3DS}^{N,n,k} = \text{errC}_{1DS,3DS,cumul}^{N,n,k} - \text{errC}_{1DS,3DS,cumul}^{N,n-1} \quad (F24)$$

$$\text{errC}_{k,k-1} = \mathbf{Err}(X^{N,n,k} - X^{N,n,k-1}) \quad (F25)$$

$$\text{errC}_{mass1DS} = \mathbf{Err}(\sum_{comp}^{NComp} (\mathbf{m}_{X,1DS}^{N,k} - [\mathbf{m}_{X,1DS}^{N-1} + (V_{surf,in}^N q_{X,root-soil}^{N,k} + S_{x,1DS-1DS}^{N,k} + S_{x,1DS-3DS}^{N,k}) \Delta t])) \quad (F26)$$

$$\text{errC}_{mass3DS} = \mathbf{Err}(\sum_{segments} (\sum_{comp}^{NComp} (\mathbf{m}_{X,3DS}^N - [\mathbf{m}_{X,3DS}^0 + \sum_n^N M_{surf,in}^n q_{X,root-soil}^n \Delta t]))) \quad (F27)$$

$$\text{assert } \text{err}_{...} \leq \epsilon_{...} \quad (F28)$$

$$\mathbf{m}_{X,1DS}^{N,n+1,-1} = \mathbf{m}_{X,1DS}^{N,n,k}, C_{X,1DS}^{N,n+1,-1} = C_{X,1DS}^{N,n,k} \quad (F29)$$

$$Q_{X,3DS}^{N,n+1,-1} = Q_{X,3DS}^{N,n,k}, C_{X,3DS}^{N,n+1,-1} = C_{X,3DS}^{N,n,k} \quad (F30)$$

TransportReac represents the implementation of a function computing biochemical reactions and solute transport according to input variables. We need to sum all the components for the solute mass balance (err_{mass}). A_n is the net assimilation of



sucrose, thus $A_n \neq 0$ only for dissolved low molecular weight organic C (C_L^l and m_L). $Q_{X,3DS} \neq 0$ only for the C of dissolved low molecular weight organic compounds and high molecular weight organic compounds.

1075 Appendix G: Soil parameters and process constraints

The tables below present the parameter and process constraints defined for TraiRhizo by Sircan et al. (2025). Baseline soil corresponds to the soil outside the rhizosphere.

Table G1. Parameter constraints defined by Sircan et al. (2025)

	Constraint	Description/ Explanation
1	$\mu_{max,C} > \mu_{max,O}$	Maximum growth rate of copiotrophs is higher than maximum growth rate of oligotrophs.
2	$k_{O,S} > k_{C,S}$	Specific substrate affinity to small molecules for oligotrophs is higher than for copiotrophs.
3	$k_{max,C} > k_{max,O}$	Maximum maintenance rate coef. must be higher for copiotrophs than for oligotrophs.
4	$C_{thresh,C} > C_{thresh,O}$	Oligotrophs (K-strategists) are adapted to low carbon and nutrient availability.
5	$k_{max,i} < \mu_{max,i}$ $i \in \{O, C\}$	It is a logical constraint to ensure organisms "fit to survive".
6	$k_{r,i} \geq k_{d,i} \ i \in \{O, C\}$	Transition to dormant (or potentially active) state is typically slower than reactivation.
7	$k_{j,i} > \mu_{max,i}$ $i \in \{O, C\}, j \in \{r, d\}$	Changes of metabolic state are faster than growth, death, and changes in composition
8	$Y_O > Y_C$	Oligotrophs are slow growing at high yield, copiotrophs are fast-growing at low yield



Table G2. Process constraints adapted from the ones defined by Sircan et al. (2025). ^a: The lower bound of the constraints was decreased by 10% compared with the value defined by Sircan et al. (2025). ^b: The lower bound of the constraints was decreased by 10% compared with the value defined by Sircan et al. (2025).

	Constraint	Description/ Explanation
1	$3.33e^{-6} < (C_O + C_C)_R < 1e^{-4} \text{ mol cm}^{-3}$	The range for the concentration of microbial biomass in the rhizosphere from literature for different soil types, textures, experimental conditions.
2 ^a	$0.9 < \left(\frac{C_O + C_C}{C_O + C_C} \right)_R < 2.5$	Microbial biomass is higher in the rhizosphere than baseline soil and lower than a threshold value which is set up from literature.
3 ^b	$3.33e^{-4} < (C_L^l + C_H^l)_R < 1.33e^{-3} \times 1.1 \text{ mol cm}^{-3}$	The range for soil organic carbon in the rhizosphere for different soil types, textures, experimental conditions.
4 ^b	$0.66 < \left(\frac{C_L^l + C_H^l}{C_L^l + C_H^l} \right)_R < 2 \times 1.1$	The range for ratio of soil organic carbon in the rhizosphere to baseline soil for different soil types, textures, experimental conditions.
5	$6e^{-4} < \left(\frac{C_O^a + C_C^a}{C_O + C_C} \right)_R < 0.6$	The range for ratio of active microbial biomass to total microbial biomass for different soil types, textures, experimental conditions.
6	$C_{L,R}^l < 4.58e^{-5} \text{ mol cm}^{-3}$	Based on water extractable organic carbon measurements. Water extractable organic carbon should include dissolved organic carbon (DOC) together with some sorbed carbon mass therefore it must be higher than the DOC concentration.
7 ^a	$0.9C_{L,B}^l < C_{L,R}^l$	Based on water extractable organic carbon measurements.
8 ^a	$0.9C_{C,R} > C_{O,R}$	The rhizosphere is dominated by copiotrophs.
9	$\frac{C_{C,B}}{C_{O,B}} < \frac{C_{C,R}}{C_{O,R}}$	

Appendix H: Lateral root water conductivity in the mature root zone

The mature root area as well as the root water conductivity ($k_{lat,x}$, $\text{cm hPa}^{-1} \text{ d}^{-1}$) values for the immature zone are taken from Giraud et al. (2023). However, in that study, $k_{lat,x} = 0$ in the mature root area (more than 0.8 cm away from the root



tip). To obtain more realistic results, we used the work of Bramley et al. (2007) to evaluate the $\frac{k_{lat,x,mature}}{k_{lat,x,immature}}$ ratio. Bramley et al. (2007, Fig. 4.15) defines the surface-normalised root resistance $k_{tot,x}$ in $m\ s^{-1}\ MPa\ 10^{-8}$ over the length l (m) from the tip as: $k_{tot,x}(l) = (-83 \times l + 20.9) \times 1e-8$ and the mean root conductance (in $m^3\ s^{-1}\ MPa\ 10^{-11}$) as $K_{tot,x}(l) = (0.7 \times l + 2.4) \times 1e-11$. We can therefore obtain the side surface of the root segment (A in m) up to l cm from $A(l) = \frac{K_{tot,x}(l)}{k_{tot,x}(l)}$.
1085 Moreover, in their study, the root axial resistance was found to be negligible, and we get therefore $k_{lat,x}(l) = k_{tot,x}(l)$ and $K_{lat,x}(l) = K_{tot,x}(l)$. We assumed that the mean $k_{lat,x}$ over the assumed immature root zone could be defined as $k_{lat,x,immature} \approx k_{lat,x}(0.008)$. We then evaluated $K_{lat,x}$ between $l_1 = 0.07$ m from the tip and $l_2 = 0.18$ m from the tip, which were the range of distances used in their study. We then computed $\int_{l_1}^{l_2} A(l)dl$ and $\int_{l_1}^{l_2} K_{lat,x}(l)dl$. From this we could get $\int_{l_1}^{l_2} k_{lat,x}(l)dl = \frac{\int_{l_1}^{l_2} K_{lat,x}(l)dl}{\int_{l_1}^{l_2} A(l)dl}$. This yielded $\frac{k_{lat,x,mature}}{k_{lat,x,immature}} = \frac{\int_{l_1}^{l_2} k_{lat,x}(l)dl}{k_{lat,x}(0.008)} \times 100 = 1.45\% \approx 1.5\%$. We consequently set
1090 $k_{lat,x,mature} = 0.015k_{lat,x,immature}$ for our modelling study.

Appendix I: Calibration of the soil carbon dynamic

This section describes the method used to calibrate the soil C dynamic. The objective was to implement a simple method allowing us to select sets representing different dynamics. A summary of the characteristics of each of the three selected microbial parameter sets is given in table 1.

1095 I1 Selection of the TraiRhizo parameter sets

In their study, Sircan et al. (2025) defined 1650 parameter sets for TraiRhizo model according to a series of parameter and process constraints, which are given in appendix G. The 1650 parameter sets were divided in three groups according to the resulting gradients of C_L^l directly at the root surface—small, medium, or strong gradient. [a] We randomly selected 33 sets in each of the three gradient categories. Then, we ran the coupled model on the (adapted) parameterised plant of Giraud et al.
1100 (2023) between days 10 and 14 of growth (with dynamic soil water and C flows). [b] Sets that did not respect the process constraints defined by Sircan et al. (2025) were removed—see Table G2. [c] From the 12 remaining sets, we selected three sets representing different soil C dynamics. For step [a], we ran the simulation without water scarcity effect—meaning, without implementing the effect of water on microbial (de)activation (Eq. (D29), (D30)) and access to soil solutes (Eq. (D10)). For step [b], following the method of (Sircan et al., 2025) and the analysis of Kuzyakov and Razavi (2019), we defined the rhizosphere
1105 as the soil volume up to 3 mm from the root surface. The baseline soil (soil outside of the rhizosphere) values were taken from the macroscale voxel data at the bottom of the soil column. We retained the sets that respected all the constraints for all the rhizosphere units at the end of the simulation. In some cases, some perirhizal zone units were slightly outside the constraints' bounds. To retain those sets, some constraint bounds were enlarged by 10%. These bounds-relaxations are indicated in table G2.
1110 Figure I1 gives the concentration of different C pools along the soil depth. The first set led to a high CO_2 production in spite of a low microbial development, and was named *highCO2*. The second set led to a high development of the microbial biomass and was named *highMB*. The last set led to low solute mineralisation and microbial development. It was named *lowMUptake*.

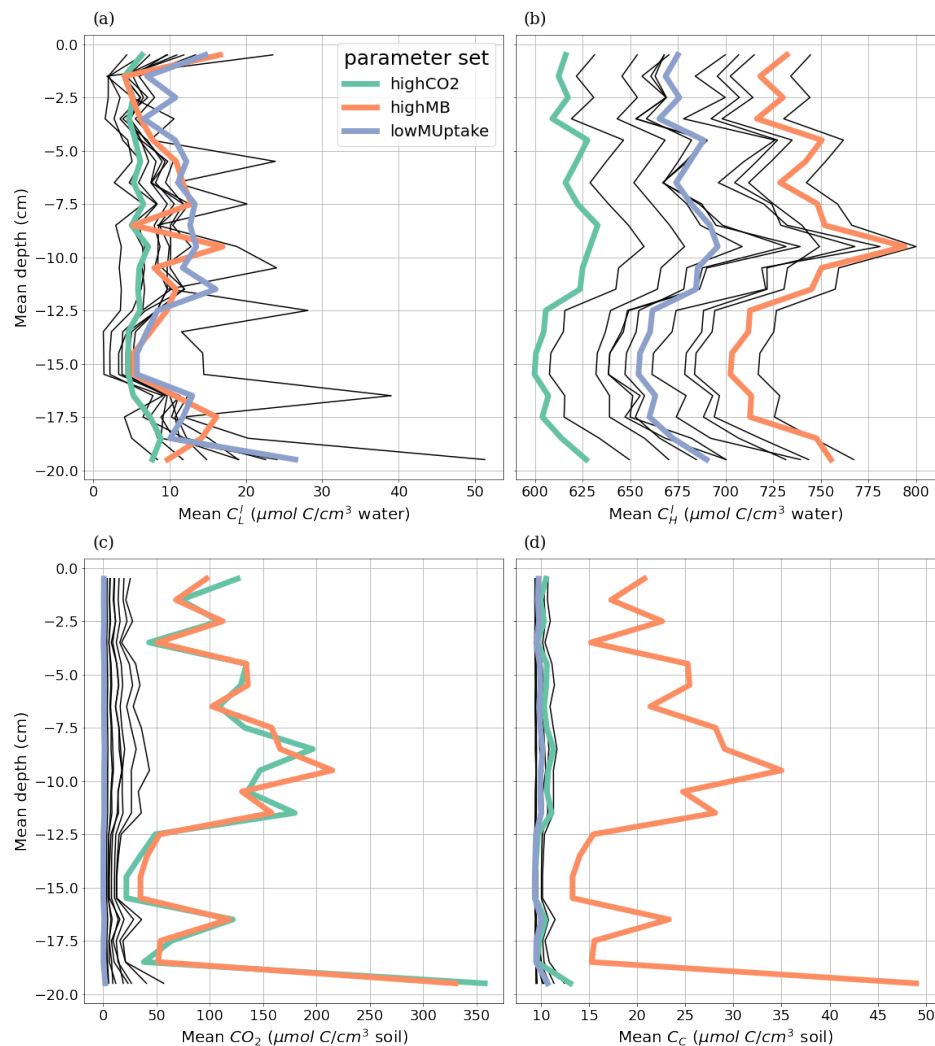


Figure 11. Mean carbon concentration per soil after four days of simulation (day 10 to 14) for concentrations of carbon from high (C_H^l) and dissolved low (C_L^l) molecular weight organic compounds, emitted CO_2 , and copiotroph carbon (C_C), in the 3D soil voxels which contain at least one root segment (perirhizal zone). The line colour gives the index of the parameter set. Only parameter sets that respect the process constraints defined by Sircan et al. (2025) after four simulation days are represented. The selected sets are *highCO2* (green line), *highMB* (orange line) and *lowMUptake* (purple line).

12 Description of the selected TraiRhizo parameter sets

12.1 Distribution of the parameter values

1115 Figs. 12 and 13 present frequency histograms for each of the parameters in the 1650 sets. The parameters pointed by the numbered arrows correspond to the parameters of the three selected sets (*highCO2*, *highMB*, *lowMUptake*). As we can see,



several of the parameter distributions are strongly skewed to the right, making some of the higher values outliers. Therefore, the sets containing the higher parameter values are more likely to give different outputs when compared with the other sets.

From the parameter values, we can give a description of the selected sets:

- 1120 All three parameter sets offer low β_C (activity of dormant copiotrophs), $k_{C,S}$ (copiotroph affinity to dissolved low molecular weight organic C compounds), $k_{d,C}$, $k_{d,O}$ (deactivation rates), $k_{max,C}$, $k_{max,O}$ (maintenance rates), $\mu_{max,C}$, $\mu_{max,O}$ (growth rates), $v_{max,depoly}$ (depolymerisation rates of high molecular weight organic C compounds) values. This follows the average values of the 1650 sets and lead to a lower microbial activity and slower deactivation. Moreover, the sets have higher than average D_{LW} values, which should smooth the distribution of C_L^l . As can be seen more clearly in Fig. I3, we have an
- 1125 equilibrium between $k_{d,O}$ and $k_{r,O}$: the sets with higher $k_{d,O}$ also have higher $k_{r,O}$. All sets have a higher $k_{r,C}$ leading to a quick reactivation rate of the copiotrophs. Finally, the three sets have similar C_{init}^l values, and, in particular, a higher than average $C_{L,init}^l$.
- highCO2* stands out by its higher β_O value, leading to a higher activity for dormant oligotrophs. Moreover, this sets has the higher D_{LW} values. Finally, the low growth yield (Y_C , Y_O) may lead to higher C usage and CO₂ emission rates.
- 1130 *highMB* has higher activation rate parameters ($k_{r,O}$, $k_{r,C}$) linked with low C_{thres} parameters, which should lead to a high activated-to-total microbial biomass, although the deactivation parameter for oligotrophs ($k_{d,O}$) is also high. The relatively higher affinity parameters ($k_{C,S}$, $k_{O,S}$) and growth parameters ($\mu_{max,C}$, $\mu_{max,O}$) should lead to a quicker increase of the microbial biomass. The low Y (yield parameters) should also lead to higher C usage and CO₂ emissions.
- lowMUptake* stands out for its low activation rate parameters ($k_{r,O}$, $k_{r,C}$) linked with high C_{thres} parameters, which should lead
- 1135 to a high activated-to-total microbial biomass, although the deactivation parameters ($k_{d,C}$, $k_{d,O}$) are also low. Low maintenance need for dormant microbes (β_C , $\beta_{d,O}$) and high yield parameters (Y , Y_C , Y_O) should also lead to a lower C usage and CO₂ emissions.

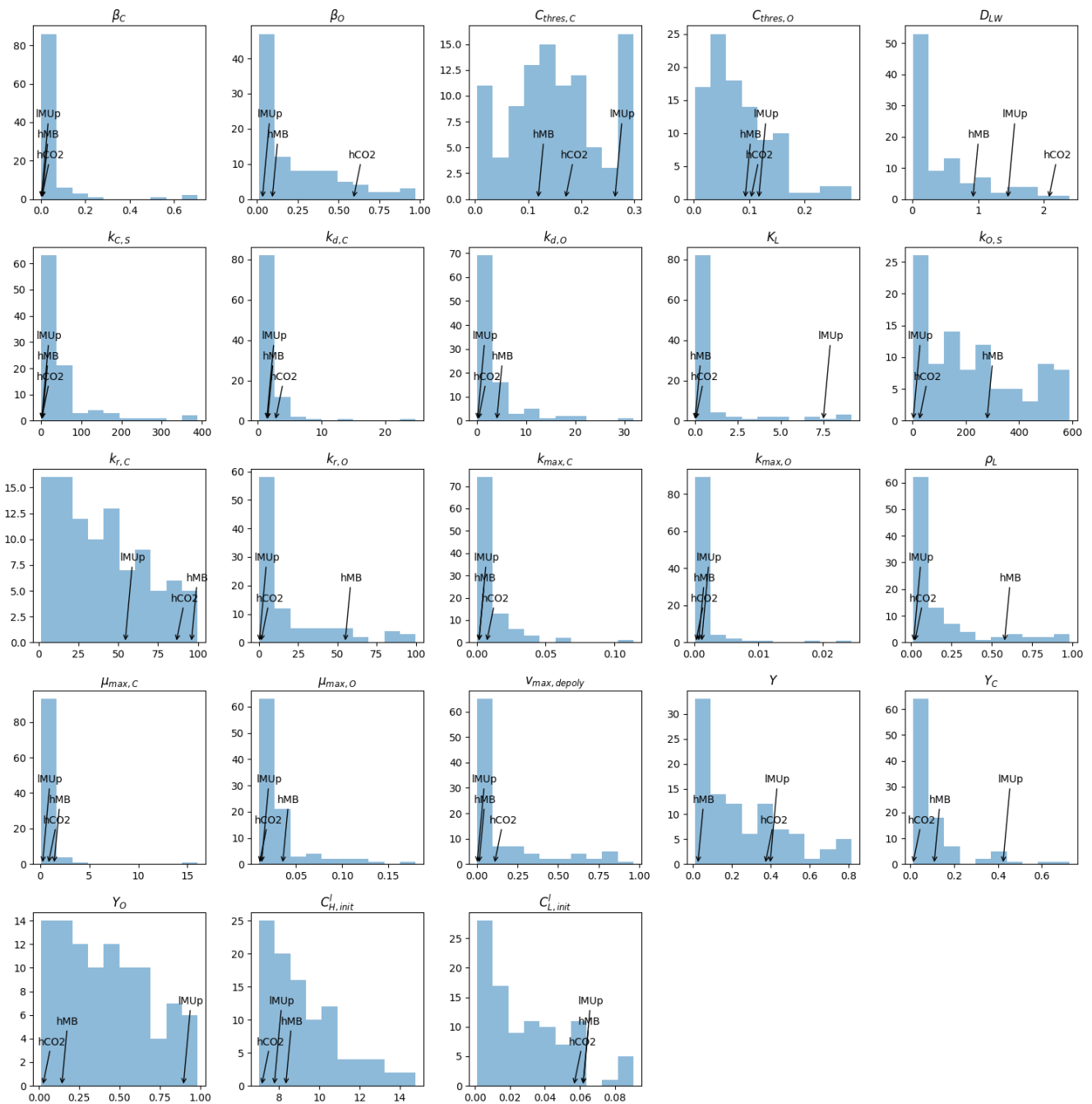


Figure I2. Histogram of the TraiRhizo input parameters. The parameters pointed by the numbered arrows correspond to the parameters of the three selected sets, *highCO2*, *highMB*, *lowMUptake*, respectively called *hCO2*, *hMB*, *IMUp*.

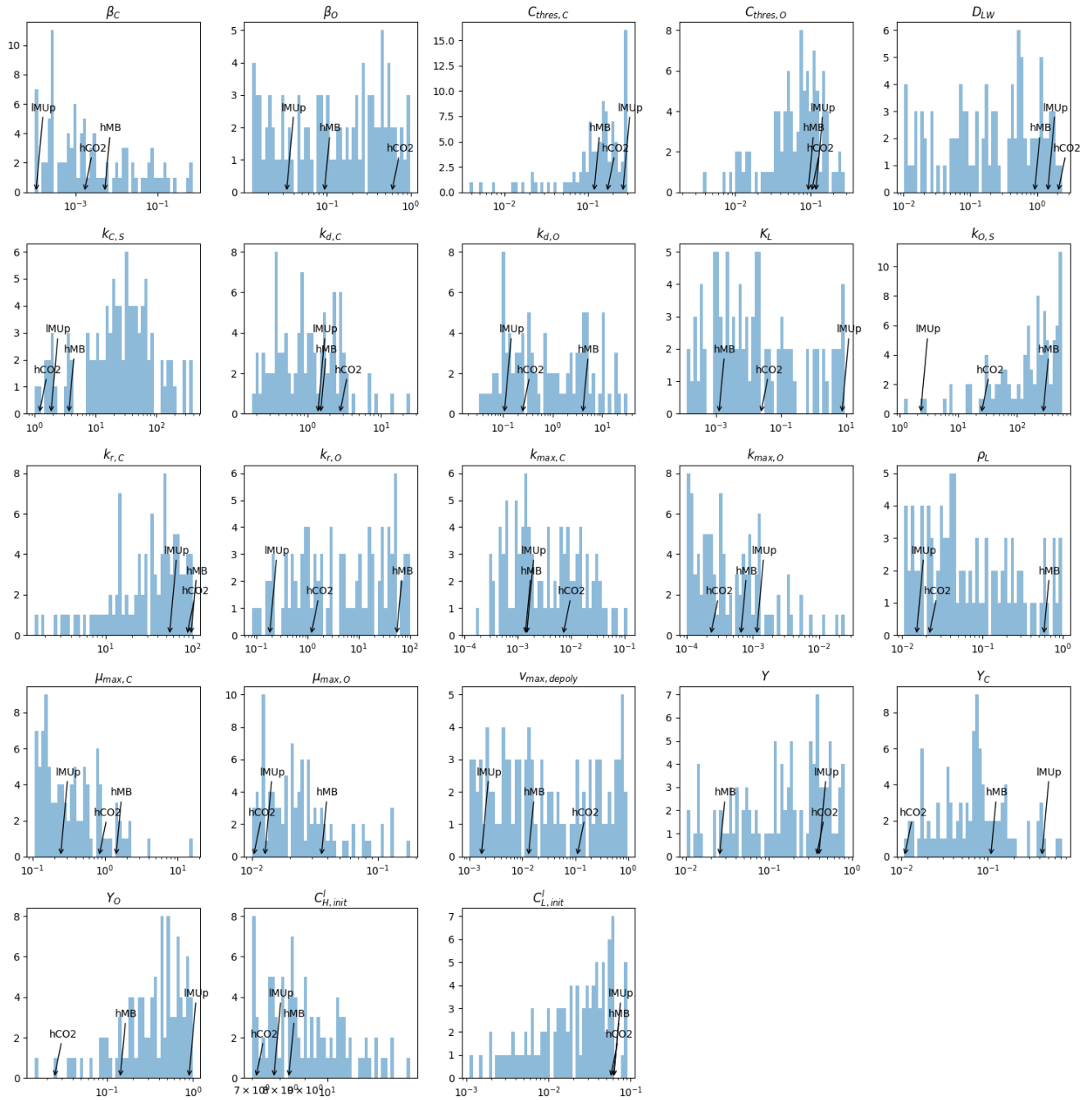


Figure I3. Logarithmic histogram of the TraiRhizo input parameters. The parameters pointed by the numbered arrows correspond to the parameters of the three selected sets, *highCO2*, *highMB*, *lowMUptake*, respectively called *hCO2*, *hMB*, *IMUp*.



12.2 Distribution of output variables under different values of dissolved low molecular weight organic carbon

We computed for a range of C_L^l values intermediary outputs describing the microbial dynamic:

- 1140 – ϕ_O (ϕ_C), –: ratio of oligotrophs (copiotrophs) which will be activated
- S_{decay} , $\text{mol C cm}^{-3} \text{ d}^{-1}$: decay rate
- S_{growth} , $\text{mol C cm}^{-3} \text{ d}^{-1}$: growth rate
- S_{deact} , $\text{mol C cm}^{-3} \text{ d}^{-1}$: deactivation rate of active microbes
- S_{react} , $\text{mol C cm}^{-3} \text{ d}^{-1}$: reactivation rate of dormant microbes
- 1145 – dCO_2dt , $\text{mol C cm}^{-3} \text{ d}^{-1}$: production rate of CO_2
- $dMBdt$, $\text{mol C cm}^{-3} \text{ d}^{-1}$: total absolute amount of change in the mass of microbial biomass C per unit of time

Fig.I4 give the ratio between the related intermediary variables for all the parameter sets with the selected sets being colored. Fig. I5 shows the same data but only for the selected sets. Subgraphics d to i use a logarithmic scale on the y-axis. As we can observe, *highCO2* led to a higher relative advantage of the oligotroph compared with the copiotroph regarding their fitness (decay-to-growth rate ratio). This was driven by the higher copiotroph decay-to-growth rate ratio. This was partly compensated by the lower ratio $\frac{S_{growthC} + S_{decayC}}{S_{deactC} + S_{reactC}}$ indicating that the copiotroph dynamic was more driven by (de)activation than by growth and decay. Moreover, we can note a higher CO_2 emission rate per unit of transformed microbial C.

- 1150 *highMB* had lower ϕ values for both copiotrophs and oligotrophs, indicating that lower C_L^l values was necessary for an activation of the microbial community. This led in part to the lower $\frac{S_{deact}}{S_{react}}$ for both microbial group, causing a quicker reactivation compared with the deactivation. *highMB* also led to relatively low decay-to-growth ratio when compared with the other two sets. Finally, for lower C_L^l values, *highMB* had the highest relative importance of (de)activation on the copiotroph dynamic, when compared with the other two sets. *lowMUptake* offered the highest copiotroph fitness and the lowest oligotroph-to-copiotroph fitness ratio, giving a relative advantage to the copiotrophs. However, this set had the highest ϕ and $\frac{S_{deact}}{S_{react}}$ values, leading to a stronger deactivation of the microbes. For this set, we have a higher importance of the growth and decay over the
- 1160 (de)activation when comparing with the other two sets.

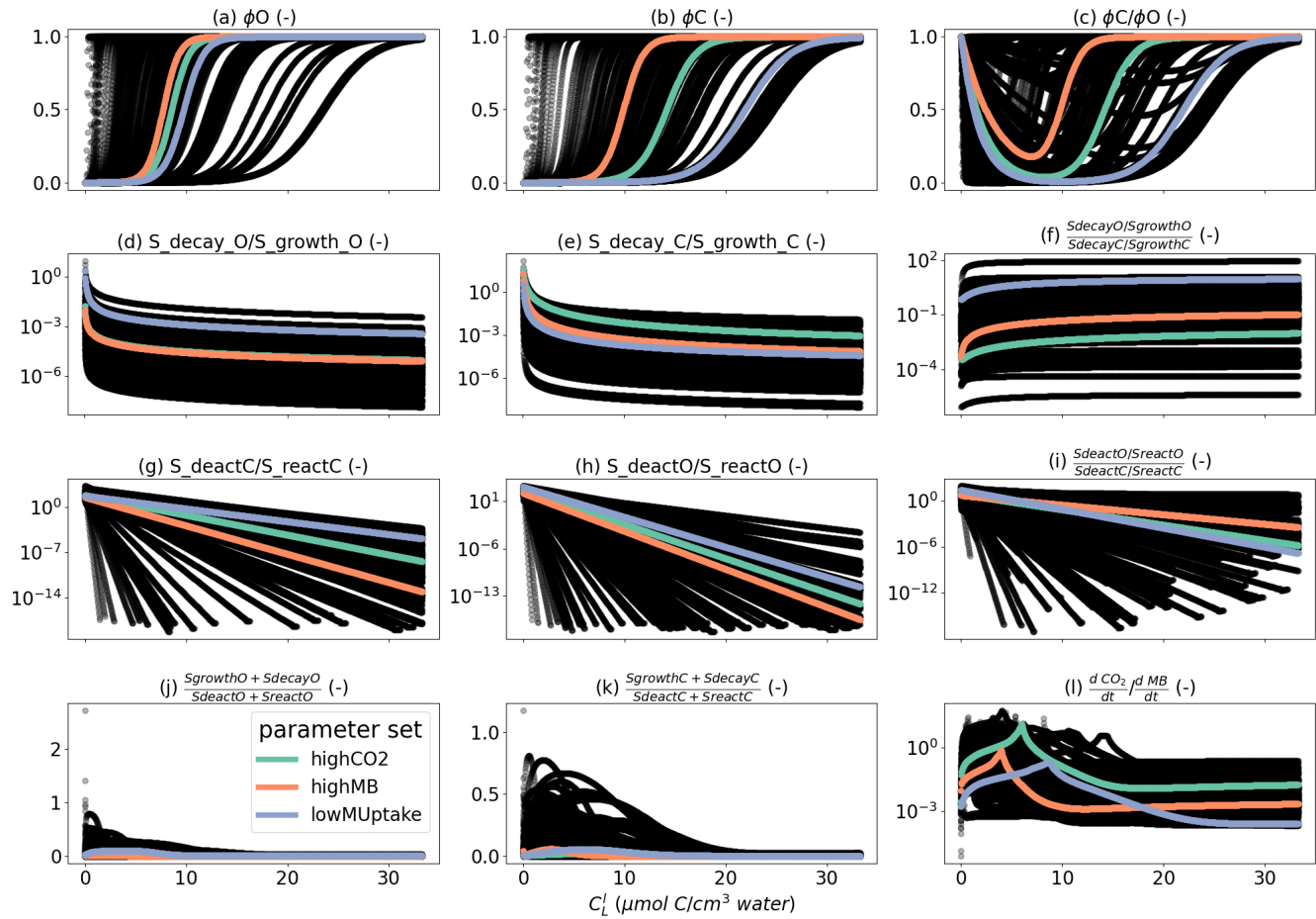


Figure I4. Distribution of specific microbial-related reaction rate for a range of C_L^l for all 99 parameter sets. The coloured values correspond to the three selected sets: *highCO2* (green line), *highMB* (orange line) and *lowMUptake* (purple line). Graphics d to i use a logarithmic scale for the y-axis.

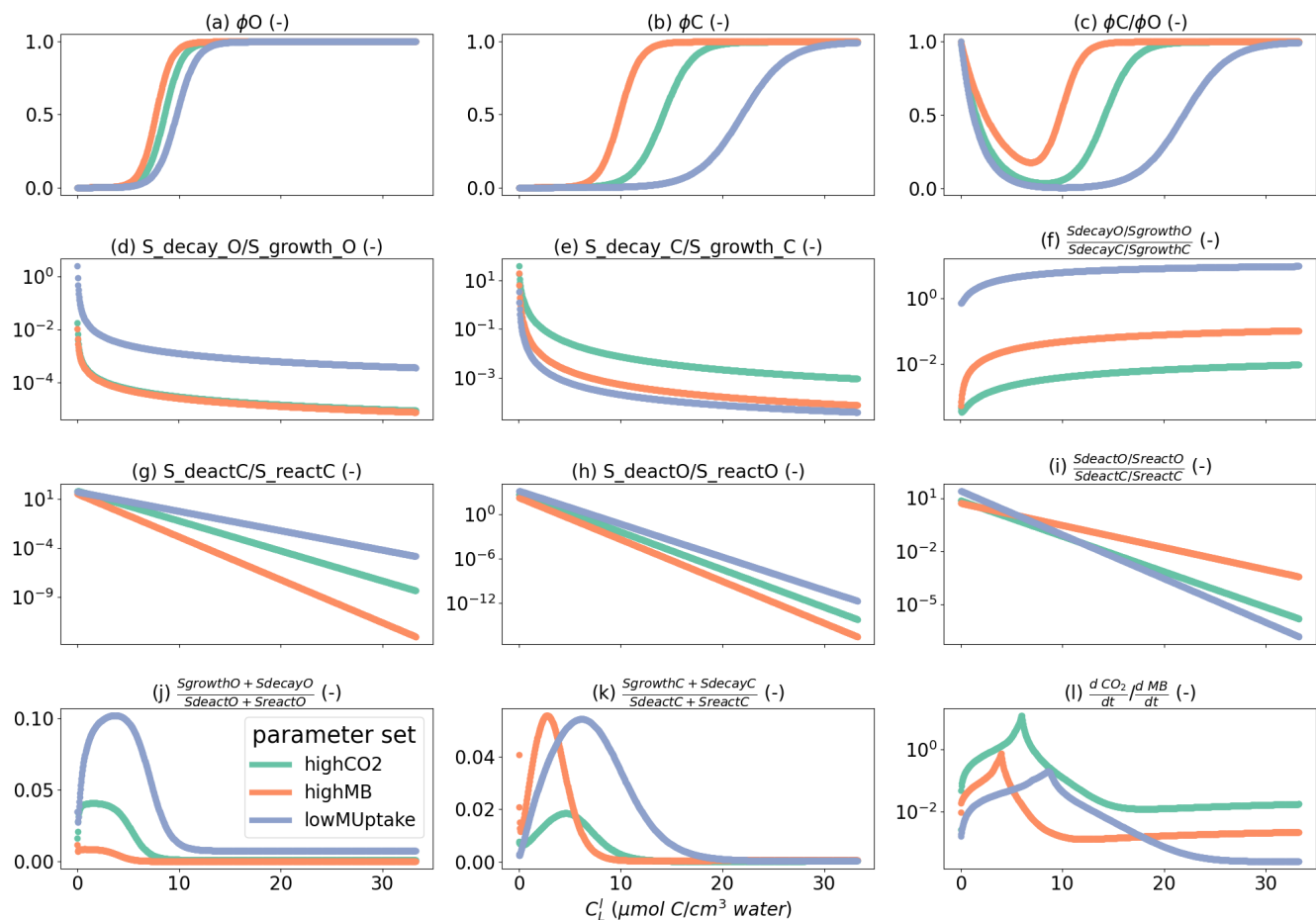


Figure 15. Distribution of specific microbial-related reaction rate for a range of C_L^l for the selected parameter sets. The coloured values correspond to the three selected sets: *highCO2* (green line), *highMB* (orange line) and *lowMUptake* (purple line). Graphics d to i use a logarithmic scale for the y-axis.

Appendix J: Complementary results

J1 Model runtime

The model was implemented on the Institute of Bio- and Geosciences (IBG-3) computer cluster, Forschungszentrum Jülich. Each simulation was run on one node (shared memory) and 32 cores (Mainboard Supermicro H12DSU-iN), using all 32 cores for the simulation of the 1D and 3D soil domains (respectively the micro- and macroscale) and one core for the plant domain. The run-time of the simulation lasted between 9 h (*baseline* with *highSolutes*) and 13 h (*lateDry* with *highCO2*). The time step of the fixed point iteration remained at 20 mn for the baseline scenarios, went several times down to 7 mn for the *earlyDry* and *lateDry* scenarios. The computation of the water flows and content was the main bottleneck for the convergence of the



iteration loop. For *baseline*, respectively 17%, 10%, and 27% of the runtime was spent solving the 3D soil domain, 1D soil
 1170 domain, and plant models. For *earlyDry*, on average, 36%, 9%, and 14% of the runtime was spent solving the 3D soil domain,
 1D soil domains, and plant models. For *lateDry*, on average, 38%, 11%, and 15% of the runtime is spent solving the 3D soil
 domain, 1D soil domain, and plant model. In total, between 54% and 64% of the runtime was dedicated to solving the models.

J2 Normalised root length density

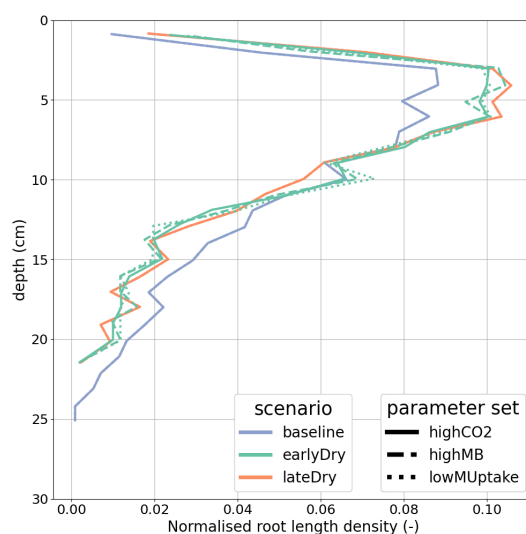


Figure J1. Normalised root length density at the end of the simulation. Line colours indicate the weather scenarios: baseline (blue) against
 an early (green) and late (red) dry spell. Line types represent different biokinetic parameter sets.

1175 Appendix K: Radial carbon concentration profiles

To evaluate how C_L^l is linked with the development and activation of the most important microbial pool (copiotrophs), Fig.
 K1 presents the radial concentration profile of the C_C and $C_C^a:C_C$ ratio at the end of the simulations. We observed a very
 steep gradient of C_C according to the distance from the root surface for *highMB* and *highCO2*. Indeed, the microbes developed
 around the C source. As they were not motile, they remained on this segment even once the root segment had become older and
 1180 its C releases and water uptake decreased. For *lowMUptake*, the C_C gradient (like the C_L^l gradient, see Fig. 12) was smoother
 than the other two parameter sets for all weather scenarios. Therefore, even though C_C directly at the root-soil interface is
 higher with *highCO2* than with *lowMUptake*, we observed similar C_C at the bulk soil and perirhizal_{trunc} scales (Figs. 8(e) and
 9(d)).

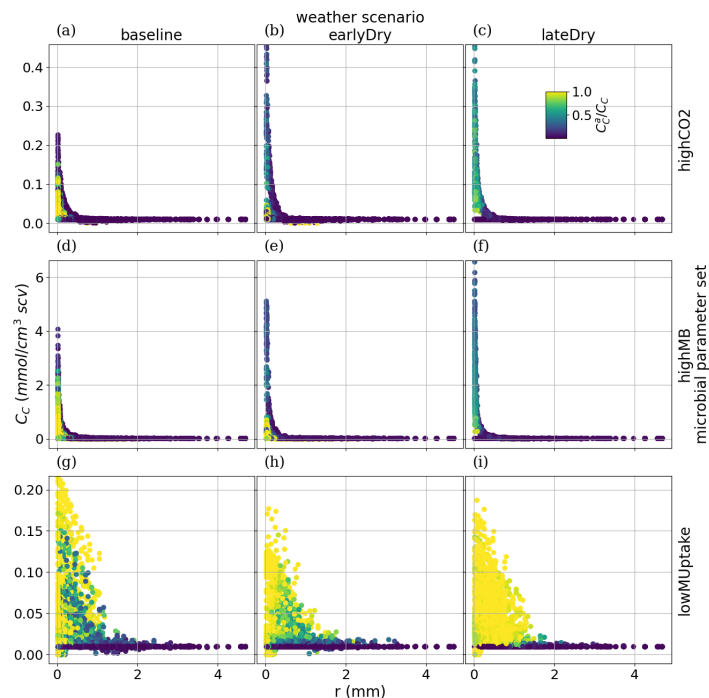


Figure K1. radial concentration profile of copiotroph carbon at the end of the simulation for each plant perirhizal zone. r (mm) corresponds to the distance to the root surface. The colour gives the ratio of active-to-total oligotroph biomass. Each column corresponds to a specific weather scenario and each row corresponds to a specific biokinetic parameterisation. We have a different y-axis for each row.

. Author contribution

1185 MG: Development and implementation of the new modules, Output visualization, Writing – original draft, Writing – review and editing.
AKS: Definition of the parameter space. MG, AKS: Setup of the equation set, Output analysis, Writing – review and editing. AS, GL, HP,
TS: Output analysis, Setup equation set, Writing – review and editing, Setup of the project and Funding acquisition, Supervision. GL, AS,
HP: Support with the model development. MG and AKS contributed equally to the study. AS and HG supervised equally this study.

. Competing interests

1190 The authors declare that they have no conflict of interest.



. Acknowledgement

The model was implemented on the Institute of Bio- and Geosciences (IBG-3) computer cluster, Forschungszentrum Jülich. The authors acknowledge the DuMu^x developers for answering the DuMu^x-related questions, as well as Dr. Magdalena Landl for her help during this study.

1195 Financial support

The authors acknowledge funding by the German Federal Ministry of Education and Research (BMBF) in the framework of the funding measure "Plant roots and soil ecosystems, significance of the rhizosphere for the bio-economy" (Rhizo4Bio), subproject CROP phase I (FKZ 031B0909). Further funding is appreciated from the German Research Foundation (DFG) within the priority program 2322 "Soil Systems" (STR 481/12-1) and under Germany's Excellence Strategy (EXC 2070-1200 390732324).



References

- Ahrens, B., Guggenberger, G., Rethemeyer, J., John, S., Marschner, B., Heinze, S., Angst, G., Mueller, C. W., Kögel-Knabner, I., Leuschner, C., Hertel, D., Bachmann, J., Reichstein, M., and Schrumpf, M.: Combination of energy limitation and sorption capacity explains 14C depth gradients, *Soil Biology and Biochemistry*, 148, <https://doi.org/10.1016/j.soilbio.2020.107912>, 2020.
- 1205 Ahusborde, E., Kern, M., and Vostrikov, V.: Numerical simulation of two-phase multicomponent flow with reactive transport in porous media: application to geological sequestration of CO₂, *ESAIM: Proceedings and surveys*, 49, 21–39, <https://doi.org/10.1051/proc/201550002>, 2015.
- Badri, D. V. and Vivanco, J. M.: Regulation and function of root exudates, *Plant, Cell & Environment*, 32, 666–681, <https://doi.org/10.1111/j.1365-3040.2009.01926.x>, 2009.
- 1210 Bardgett, R. D. and Caruso, T.: Soil microbial community responses to climate extremes: resistance, resilience and transitions to alternative states, *Philosophical Transactions of the Royal Society B: Biological Sciences*, 375, <https://doi.org/10.1098/rstb.2019.0112>, 2020.
- Bardgett, R. D., Manning, P., Morriën, E., and De Vries, F. T.: Hierarchical responses of plant–soil interactions to climate change: consequences for the global carbon cycle, *Journal of Ecology*, 101, 334–343, <https://doi.org/10.1111/1365-2745.12043>, 2013.
- Barillot, R., De Swaef, T., Combes, D., Durand, J.-L., Escobar-Gutiérrez, A. J., Martre, P., Perrot, C., Roy, E., and Frak, E.: Leaf elongation
1215 response to blue light is mediated by stomatal-induced variations in transpiration in *Festuca arundinacea*, *Journal of Experimental Botany*, 72, 2642–2656, <https://doi.org/10.1093/jxb/eraa585>, 2020.
- Bazot, S., Mikola, J., Nguyen, C., and Robin, C.: Defoliation-induced changes in carbon allocation and root soluble carbon concentration in field-grown *Lolium perenne* plants: do they affect carbon availability, microbes and animal trophic groups in soil?, *Functional Ecology*, 19, 886–896, <https://doi.org/10.1111/j.1365-2435.2005.01037.x>, 2005.
- 1220 Blum, A.: Osmotic adjustment is a prime drought stress adaptive engine in support of plant production, *Plant, Cell & Environment*, 40, 4–10, <https://doi.org/10.1111/pce.12800>, 2017.
- Bonkowski, M., Tarkka, M., Razavi, B., Schmidt, H., Blagodatskaya, E., Koller, R., Yu, P., Knief, C., Hochholdinger, F., and Vetterlein, D.: Spatiotemporal Dynamics of Maize (*Zea mays* L.) Root Growth and Its Potential Consequences for the Assembly of the Rhizosphere Microbiota, *Frontiers in Microbiology*, 12, <https://doi.org/10.3389/fmicb.2021.619499>, 2021.
- 1225 Borken, W. and Matzner, E.: Reappraisal of drying and wetting effects on C and N mineralization and fluxes in soils, *Global Change Biology*, 15, 808–824, <https://doi.org/10.1111/j.1365-2486.2008.01681.x>, 2009.
- Braghiere, R. K., Gérard, F., Evers, J. B., Pradal, C., and Pagès, L.: Simulating the effects of water limitation on plant biomass using a 3D functional-structural plant model of shoot and root driven by soil hydraulics, *Ann Bot*, 126, 713–728, <https://doi.org/10.1093/aob/mcaa059>, 2020.
- 1230 Bramley, H., Turner, D., Tyerman, S., and Turner, N.: Water Flow in the Roots of Crop Species: The Influence of Root Structure, Aquaporin Activity, and Waterlogging, in: *Advances in Agronomy*, vol. 96 of *Advances in Agronomy*, pp. 133–196, Academic Press, [https://doi.org/10.1016/S0065-2113\(07\)96002-2](https://doi.org/10.1016/S0065-2113(07)96002-2), 2007.
- Brown, R. W., Chadwick, D. R., Bending, G. D., Collins, C. D., Whelton, H. L., Daulton, E., Covington, J. A., Bull, I. D., and Jones, D. L.: Nutrient (C, N and P) enrichment induces significant changes in the soil metabolite profile and microbial carbon partitioning, *Soil Biology and Biochemistry*, 172, <https://doi.org/10.1016/j.soilbio.2022.108779>, 2022.
- 1235 Canarini, A., Kaiser, C., Merchant, A., Richter, A., and Wanek, W.: Root Exudation of Primary Metabolites: Mechanisms and Their Roles in Plant Responses to Environmental Stimuli, *Front Plant Sci*, 10, 157, <https://doi.org/10.3389/fpls.2019.00157>, 2019.



- Coussement, J., Swaef, T., Lootens, P., Roldán-Ruiz, I., and Steppe, K.: Introducing turgor-driven growth dynamics into functional-structural plant models, *Annals of botany*, 121, <https://doi.org/10.1093/aob/mcx144>, 2018.
- 1240 Damour, G., Simonneau, T., Cochard, H., and Urban, L.: An overview of models of stomatal conductance at the leaf level, *Plant, Cell and Environment*, 33, 1419–1438, <https://doi.org/10.1111/j.1365-3040.2010.02181.x>, 2010.
- Darrah, P. R.: Models of the rhizosphere, *Plant and Soil*, 133, 187–199, <https://doi.org/10.1007/BF00009191>, 1991.
- de la Fuente Cantó, C., Simonin, M., King, E., Moulin, L., Bennett, M., Castrillo, G., and Laplace, L.: An extended root phenotype: the rhizosphere, its formation and impacts on plant fitness, *The Plant Journal*, 103, <https://doi.org/10.1111/tpj.14781>, 2020.
- 1245 De Swaef, T., Pieters, O., Appeltans, S., Borra-Serrano, I., Coudron, W., Couvreur, V., Garré, S., Lootens, P., Nicolaï, B., Pols, L., Saint Cast, C., Šalagovič, J., Van Haeverbeke, M., Stock, M., and wyffels, F.: On the pivotal role of water potential to model plant physiological processes, in *silico Plants*, 4, <https://doi.org/10.1093/insilicoplants/diab038>, 2022.
- Debnath, L.: *Linear Partial Differential Equations*, pp. 1–148, Birkhäuser Boston, Boston, MA, ISBN 978-0-8176-4418-5, https://doi.org/10.1007/0-8176-4418-0_1, 2005.
- 1250 Deng, L., Peng, C., Kim, D.-G., Li, J., Liu, Y., Hai, X., Liu, Q., Huang, C., Shangguan, Z., and Kuzyakov, Y.: Drought effects on soil carbon and nitrogen dynamics in global natural ecosystems, *Earth-Science Reviews*, 214, <https://doi.org/10.1016/j.earscirev.2020.103501>, 2021.
- Dilkes, N. B., Jones, D. L., and Farrar, J.: Temporal Dynamics of Carbon Partitioning and Rhizodeposition in Wheat, *Plant Physiology*, 134, 706–715, <https://doi.org/10.1104/pp.103.032045>, 2004.
- Drake, J. E., Darby, B. A., Giasson, M.-A., Kramer, M. A., Phillips, R. P., and Finzi, A. C.: Stoichiometry constrains microbial response to root exudation- insights from a model and a field experiment in a temperate forest, *Biogeosciences*, 10, 821–838, <https://doi.org/10.5194/bg-10-821-2013>, 2013.
- 1255 Dupuy, L. X. and Silk, W. K.: Mechanisms of Early Microbial Establishment on Growing Root Surfaces, *Vadose Zone Journal*, 15, <https://doi.org/10.2136/vzj2015.06.0094>, 2016.
- Farquhar, G. D., von Caemmerer, S., and Berry, J. A.: A biochemical model of photosynthetic CO₂ assimilation in leaves of C₃ species, *Planta*, 149, 78–90, <https://doi.org/10.1007/BF00386231>, 1980.
- 1260 Galindo-Castañeda, T., Lynch, J., Six, J., and Hartmann, M.: Improving Soil Resource Uptake by Plants Through Capitalizing on Synergies Between Root Architecture and Anatomy and Root-Associated Microorganisms, *Frontiers in Plant Science*, 13, <https://doi.org/10.3389/fpls.2022.827369>, 2022.
- Galindo-Castañeda, T., Hartmann, M., and Lynch, J. P.: Location: root architecture structures rhizosphere microbial associations, *Journal of Experimental Botany*, 75, 594–604, <https://doi.org/10.1093/jxb/erad421>, 2023.
- 1265 Gaudio, N., Louarn, G., Barillot, R., Meunier, C., Vezy, R., and Launay, M.: Exploring complementarities between modelling approaches that enable upscaling from plant community functioning to ecosystem services as a way to support agroecological transition, in *silico Plants*, 4, <https://doi.org/10.1093/insilicoplants/diab037>, 2021.
- George, T. S., Bulgarelli, D., Carminati, A., Chen, Y., Jones, D., Kuzyakov, Y., Schnepf, A., Wissuwa, M., and Roose, T.: Bottom-up perspective – The role of roots and rhizosphere in climate change adaptation and mitigation in agroecosystems, *Plant and Soil*, <https://doi.org/10.1007/s11104-024-06626-6>, 2024.
- 1270 Giraud, M., Le Gall, S., Harings, M., Javaux, M., Leitner, D., Meunier, F., Rothfuss, Y., van Dusschoten, D., Vanderborght, J., Vereecken, H., Lobet, G., and Schnepf, A.: CPlantBox: a fully coupled modeling platform for the water and carbon fluxes in the Soil-Plant-Atmosphere-Continuum, in *silico Plants*, <https://doi.org/10.1093/insilicoplants/diad009>, 2023.



- 1275 Gérard, F., Blitz-Frayret, C., Hinsinger, P., and Pagès, L.: Modelling the interactions between root system architecture, root functions and reactive transport processes in soil, *Plant and Soil*, 413, 161–180, <https://doi.org/10.1007/s11104-016-3092-x>, 2017.
- Hartmann, H., Bahn, M., Carbone, M., and Richardson, A. D.: Plant carbon allocation in a changing world – challenges and progress: introduction to a Virtual Issue on carbon allocation, *New Phytologist*, 227, 981–988, <https://doi.org/10.1111/nph.16757>, 2020.
- Helmig, R.: *Multiphase Flow and Transport Processes in the Subsurface: A Contribution to the Modeling of Hydrosystems*, Springer, <https://doi.org/http://dx.doi.org/10.1007/978-3-642-60763-9>, 1997.
- 1280 Heppell, J., Payvandi, S., Talboys, P., Zygalkis, K. C., Langton, D., Sylvester-Bradley, R., Edwards, A. C., Walker, R., Withers, P., Jones, D. L., and Roose, T.: Use of a coupled soil-root-leaf model to optimise phosphate fertiliser use efficiency in barley, *Plant and Soil*, 406, 341–357, <https://doi.org/10.1007/s11104-016-2883-4>, 2016.
- Hirschberg, K., Miller, C. M., Ellenberg, J., Presley, J. F., Siggia, E. D., Phair, R. D., and Lippincott-Schwartz, J.: Kinetic analysis of secretory protein traffic and characterization of golgi to plasma membrane transport intermediates in living cells, *J Cell Biol*, 143, <https://doi.org/10.1083/jcb.143.6.1485>, 1998.
- 1285 Hobbie, J. E. and Hobbie, E. A.: Microbes in nature are limited by carbon and energy: the starving-survival lifestyle in soil and consequences for estimating microbial rates, *Frontiers in Microbiology*, 4, <https://doi.org/10.3389/fmicb.2013.00324>, 2013.
- Jiang, C., Séquaris, J.-M., Wacha, A., Bóta, A., Vereecken, H., and Klumpp, E.: Effect of metal oxide on surface area and pore size of water-dispersible colloids from three German silt loam topsoils, *Geoderma*, 235–236, 260–270, <https://doi.org/10.1016/j.geoderma.2014.07.017>, 2014.
- 1290 Jorda Guerra, H., Huber, K., Kunkel, A., Vanderborght, J., Javaux, M., Oberdörster, C., Hammel, K., and Schnepf, A.: Mechanistic modeling of pesticide uptake with a 3D plant architecture model, *Environmental Science and Pollution Research*, 28, <https://doi.org/10.1007/s11356-021-14878-3>, 2021.
- 1295 Khare, D., Selzner, T., Leitner, D., Vanderborght, J., Vereecken, H., and Schnepf, A.: Root System Scale Models Significantly Overestimate Root Water Uptake at Drying Soil Conditions, *Frontiers in Plant Science*, 13, <https://doi.org/10.3389/fpls.2022.798741>, 2022.
- Koch, T., Glaser, D., Weishaupt, K., Ackermann, S., Beck, M., Becker, B., Burbulla, S., Class, H., Coltman, E., Emmert, S., Fetzner, T., Grüniger, C., Heck, K., Hommel, J., Kurz, T., Lipp, M., Mohammadi, F., Scherrer, S., Schneider, M., Seitz, G., Stadler, L., Utz, M., Weinhardt, F., and Flemisch, B.: DuMux 3 – an open-source simulator for solving flow and transport problems in porous media with a focus on model coupling, *Computers & Mathematics with Applications*, 81, 423–443, <https://doi.org/10.1016/j.camwa.2020.02.012>, 2021.
- 1300 Kravchenko, L. V., Strigul, N. S., and Shvytov, I. A.: Mathematical Simulation of the Dynamics of Interacting Populations of Rhizosphere Microorganisms, *Microbiology*, 73, 189–195, <https://doi.org/10.1023/B:MICI.0000023988.11064.43>, 2004.
- Kuppe, C. W., Schnepf, A., von Lieres, E., Watt, M., and Postma, J. A.: Rhizosphere models: their concepts and application to plant-soil ecosystems, *Plant and Soil*, 474, 17–55, <https://doi.org/10.1007/s11104-021-05201-7>, 2022.
- 1305 Kutschera-Mitter, L., Barmicheva, K. M., and Sobotik, M.: The Importance of Root-Cap Mucilage for Plant And Soil, pp. 673–683, Springer Netherlands, Dordrecht, ISBN 978-94-011-5270-9, https://doi.org/10.1007/978-94-011-5270-9_60, 1998.
- Kuzyakov, Y. and Cheng, W.: Photosynthesis controls of CO₂ efflux from maize rhizosphere, *Plant and Soil*, 263, 85–99, <https://doi.org/10.1023/B:PLSO.0000047728.61591.fd>, 2004.
- 1310 Kuzyakov, Y. and Razavi, B. S.: Rhizosphere size and shape: Temporal dynamics and spatial stationarity, *Soil Biology and Biochemistry*, 135, 343–360, <https://doi.org/10.1016/j.soilbio.2019.05.011>, 2019.



- Lacointe, A. and Minchin, P. E. H.: A Mechanistic Model to Predict Distribution of Carbon Among Multiple Sinks, pp. 371–386, Springer New York, New York, NY, https://doi.org/10.1007/978-1-4939-9562-2_28, 2019.
- Landl, M., Haupenthal, A., Leitner, D., Kroener, E., Vetterlein, D., Bol, R., Vereecken, H., Vanderborght, J., and Schnepf, A.: Simulating rhizodeposition patterns around growing and exuding root systems, in silico *Plants*, 3, <https://doi.org/10.1093/insilicoplants/diab028>, 2021a.
- Landl, M., Phalempin, M., Schlüter, S., Vetterlein, D., Vanderborght, J., Kroener, E., and Schnepf, A.: Modeling the Impact of Rhizosphere Bulk Density and Mucilage Gradients on Root Water Uptake, *Frontiers in Plant Science*, 3, <https://doi.org/10.3389/fagro.2021.622367>, 2021b.
- 1315 Leuning, R.: A critical appraisal of a combined stomatal-photosynthesis model for C₃ plants, *Plant, Cell and Environment*, 18, 339–355, <https://doi.org/10.1111/j.1365-3040.1995.tb00370.x>, 1995.
- Lynch, J.: Harnessing root architecture to address global challenges, *The Plant Journal*, 109, <https://doi.org/10.1111/tpj.15560>, 2021.
- Lynch, J. M. and Whipps, J. M.: Substrate flow in the rhizosphere, *Plant and Soil*, 129, 1–10, <https://doi.org/10.1007/BF00011685>, 1990.
- Lynch, J. P., Strock, C. F., Schneider, H. M., Sidhu, J. S., Ajmera, I., Galindo-Castañeda, T., Klein, S. P., and Hanlon, M. T.: Root anatomy and soil resource capture, *Plant and Soil*, 466, 21–63, <https://doi.org/10.1007/s11104-021-05010-y>, 2021.
- 1325 Ma, W., Tang, S., Dengzeng, Z., Zhang, D., Zhang, T., and Ma, X.: Root exudates contribute to belowground ecosystem hotspots: A review, *Frontiers in Microbiology*, 13, <https://doi.org/10.3389/fmicb.2022.937940>, 2022.
- Mai, T. H., Schnepf, A., Vereecken, H., and Vanderborght, J.: Continuum multiscale model of root water and nutrient uptake from soil with explicit consideration of the 3D root architecture and the rhizosphere gradients, *Plant and Soil*, 439, 273–292, <https://doi.org/10.1007/s11104-018-3890-4>, 2019.
- 1330 McDougall, B. M. and Rovira, A. D.: Sites of exudation of ¹⁴C-labelled compounds from wheat roots, *New Phytologist*, 69, 999–1003, <https://doi.org/10.1111/j.1469-8137.1970.tb02479.x>, 1970.
- Meunier, F., Draye, X., Vanderborght, J., Javaux, M., and Couvreur, V.: A hybrid analytical-numerical method for solving water flow equations in root hydraulic architectures, *Applied Mathematical Modelling*, 52, 648–663, <https://doi.org/10.1016/j.apm.2017.08.011>, 2017.
- 1335 Millington, R. J. and Quirk, J. P.: Permeability of porous solids, *Transactions of the Faraday Society*, 57, 1200–1207, <https://doi.org/10.1039/TF9615701200>, 1961.
- Morandage, S., Laloy, E., Schnepf, A., Vereecken, H., and Vanderborght, J.: Bayesian inference of root architectural model parameters from synthetic field data, *Plant and Soil*, 467, 1–23, <https://doi.org/10.1007/s11104-021-05026-4>, 2021.
- 1340 Morandage, S., Schnepf, A., Leitner, D., Javaux, M., Vereecken, H., and Vanderborght, J.: Correction to: Parameter sensitivity analysis of a root system architecture model based on virtual field sampling, *Plant and Soil*, 477, 849–850, <https://doi.org/10.1007/s11104-021-05089-3>, 2022.
- Moyano, F. E., Manzoni, S., and Chenu, C.: Responses of soil heterotrophic respiration to moisture availability: An exploration of processes and models, *Soil Biology and Biochemistry*, 59, 72–85, <https://doi.org/10.1016/j.soilbio.2013.01.002>, 2013.
- 1345 Mualem, Y.: A new model for predicting the hydraulic conductivity of unsaturated porous media, *Water Resources Research*, 12, 513–522, <https://doi.org/10.1029/WR012i003p00513>, 1976.
- Neumann, G. and Römheld, V.: The release of root exudates as affected by the plant’s physiological status, pp. 23–54, CRC Press, 2009.
- Nguyen, C.: Rhizodeposition of Organic C by Plant: Mechanisms and Controls, vol. 23, pp. 97–123, Springer Netherlands, ISBN 978-90-481-2665-1, https://doi.org/10.1007/978-90-481-2666-8_9, 2009.



- 1350 Pagel, H., Kriesche, B., Uksa, M., Poll, C., Kandeler, E., Schmidt, V., and Streck, T.: Spatial Control of Carbon Dynamics in Soil by Microbial Decomposer Communities, *Frontiers in Environmental Science*, 8, <https://doi.org/10.3389/fenvs.2020.00002>, 2020.
- Personeni, E., Nguyen, C., Marchal, P., and Pagès, L.: Experimental evaluation of an efflux–influx model of C exudation by individual apical root segments, *Journal of Experimental Botany*, 58, 2091–2099, <https://doi.org/10.1093/jxb/erm065>, 2007.
- Poeplau, C. and Don, A.: A simple soil organic carbon level metric beyond the organic carbon to clay ratio, *Soil Use and Management*, 39, <https://doi.org/10.1111/sum.12921>, 2023.
- 1355 Pot, V., Portell, X., Otten, W., Garnier, P., Monga, O., and Baveye, P. C.: Accounting for soil architecture and microbial dynamics in microscale models: Current practices in soil science and the path ahead, *European Journal of Soil Science*, 73, <https://doi.org/10.1111/ejss.13142>, 2022.
- Prescott, C. E., Grayston, S. J., Helmisaari, H.-S., Kaštovská, E., Körner, C., Lambers, H., Meier, I. C., Millard, P., and 1360 Ostonen, I.: Surplus Carbon Drives Allocation and Plant–Soil Interactions, *Trends in Ecology & Evolution*, 35, 1110–1118, <https://doi.org/10.1016/j.tree.2020.08.007>, 2020.
- Putten, W., Bardgett, R., Bever, J., Bezemer, T., Casper, B., Fukami, T., Kardol, P., Klironomos, J., Kulmatiski, A., Schweitzer, J., Suding, K., Voorde, T., and Wardle, D.: Plant-Soil Feedbacks: the past, the present and future challenges., *Journal of Ecology*, 101, 265–276, <https://doi.org/10.1111/1365-2745.12054>, 2013.
- 1365 Přikryl, Z. and Vančura, V.: Root exudates of plants, *Plant and Soil*, 57, 69–83, <https://doi.org/10.1007/BF02139643>, 1980.
- Rakshit, A., Singh, S., Abhilash, P. C., and Biswas, A., eds.: *Soil Science: Fundamentals to Recent Advances*, Springer, Singapore, <https://doi.org/10.1007/978-981-16-0917-6>, 2021.
- Rees, F., Richard-Molard, C., Chenu, C., and Andrieu, B.: Modelling Rhizodeposition with Functional-Structural Plant Models, in: 10th International Society on Root Research Conference (ISRR-10), 2018.
- 1370 Rees, F., Barillot, R., Gauthier, M., Pagès, L., Pradal, C., and Andrieu, B.: Simulating rhizodeposition as a function of shoot and root interactions within a new 3D Functional-Structural Plant Model, in: *FSPM 2020 - 9th International Conference on Functional-Structural Plant Models*, pp. 22–23, Hanover / Virtual, Germany, <https://hal.inrae.fr/hal-02964060>, 2020.
- Rees, F., Gauthier, M., Barillot, R., Richard-Molard, C., Jullien, A., Chenu, C., Pradal, C., and Andrieu, B.: Quantitative importance of various rhizodeposition processes: lessons from a mechanistic functional-structural root model, in: *FSPM 2023 - 10th International Conference on Functional-Structural Plant Models*, Berlin, Germany, <https://hal.inrae.fr/hal-04098521>, 2023.
- 1375 Richards, L. A.: Capillary conduction of liquids through porous mediums, *Physics*, 1, 318–333, <https://doi.org/10.1063/1.1745010>, 1931.
- Roose, T., Keyes, S., Daly, K., Carminati, A., Otten, W., Vetterlein, D., and Peth, S.: Challenges in imaging and predictive modeling of rhizosphere processes, *Plant and Soil*, 407, <https://doi.org/10.1007/s11104-016-2872-7>, 2016.
- Rougier, M.: Secretory Activity of the Root Cap, vol. 13/B of *Encyclopedia of Plant Physiology*, p. 772, Springer, Berlin, Heidelberg, ISBN 978-3-642-68234-6, <https://doi.org/10.1007/978-3-642-68234-6>, 1981.
- 1380 Ruiz, S., McKay Fletcher, D., Williams, K., and Roose, T.: *Plant–Soil Modelling*, vol. 4, pp. 127–198, John Wiley & Sons, Ltd, ISBN 9781119312994, <https://doi.org/10.1002/9781119312994.apr0755>, 2021.
- Schnepf, A., Huber, K., Landl, M., Meunier, F., Petrich, L., and Schmidt, V.: Statistical Characterization of the Root System Architecture Model CRootBox, *Vadose Zone Journal*, 17, <https://doi.org/10.2136/vzj2017.12.0212>, 2018a.
- 1385 Schnepf, A., Leitner, D., Landl, M., Lobet, G., Mai, T. H., Morandage, S., Sheng, C., Zörner, M., Vanderborght, J., and Vereecken, H.: CRootBox: a structural–functional modelling framework for root systems, *Annals of Botany*, 121, 1033–1053, <https://doi.org/10.1093/aob/mcx221>, 2018b.



- Schnepf, A., Carminati, A., Ahmed, M., Ani, M., Benard, P., Bentz, J., Bonkowski, M., Knott, M., Diehl, D., Duddek, P., Kroener, E., Javaux, M., Landl, M., Lehdorff, E., Lippold, E., Lieu, A., Mueller, C., Oburger, E., Otten, W., and Vetterlein, D.: Linking rhizosphere processes across scales: Opinion, *Plant and Soil*, 478, <https://doi.org/10.1007/s11104-022-05306-7>, 2022.
- 1390 Schnepf, A., Leitner, D., Landl, M., Khare, D., Heck, A., Giraud, M., Selzner, T., Helmrich, D., Lobet, G., Zhou, X., Bouvri, A., Ullah, S., Feron, T., Heymans, A., and Koch, T.: CPlantBox, branch Giraud2025_CarbonStabilisation, <https://doi.org/10.5281/zenodo.14809628>, zenodo [code], 2025a.
- Schnepf, A., Leitner, D., Landl, M., Khare, D., Heck, A., Giraud, M., Selzner, T., Helmrich, D., Lobet, G., Zhou, X., Bouvri, A., Ullah, S., Feron, T., Heymans, A., and Koch, T.: dumux-rosi, branch Giraud2025_CarbonStabilisation, <https://doi.org/10.5281/zenodo.14809414>, zenodo [code], 2025b.
- 1395 Schröder, N., Lazarovitch, N., Vanderborght, J., Vereecken, H., and Javaux, M.: Linking transpiration reduction to rhizosphere salinity using a 3D coupled soil-plant model, *Plant and Soil*, 377, 277–293, <https://doi.org/10.1007/s11104-013-1990-8>, 2014.
- Schwartz, N., Carminati, A., and Javaux, M.: The impact of mucilage on root water uptake—A numerical study, *Water Resources Research*, 52, 264–277, <https://doi.org/10.1002/2015WR018150>, 2016.
- 1400 Silva, L. C. R. and Lambers, H.: Soil-plant-atmosphere interactions: structure, function, and predictive scaling for climate change mitigation, *Plant and Soil*, 461, 5–27, <https://doi.org/10.1007/s11104-020-04427-1>, 2021.
- Sircan, A. K., Streck, T., Schnepf, A., Giraud, M., Lattacher, A., Kandeler, E., Poll, C., and Pagel, H.: Trait-based Modeling of Microbial Interactions and Carbon Turnover in the Rhizosphere, *Soil Biology and Biochemistry*, <https://doi.org/10.1016/j.soilbio.2024.109698>, 2025.
- 1405 Thorpe, M. R., Lacoite, A., and Minchin, P. E. H.: Modelling phloem transport within a pruned dwarf bean: a 2-source-3-sink system, *Functional Plant Biology*, 38, 127–138, <https://doi.org/10.1071/fp10156>, 2011.
- Tixier, A., Forest, M., Prudent, M., Durey, V., Zwieniecki, M., and Barnard, R. L.: Root exudation of carbon and nitrogen compounds varies over the day–night cycle in pea: The role of diurnal changes in internal pools, *Plant, Cell & Environment*, 46, 962–974, <https://doi.org/10.1111/pce.14523>, 2023.
- 1410 Trofymow, J. A., Coleman, D. C., and Cambardella, C.: Rates of rhizodeposition and ammonium depletion in the rhizosphere of axenic oat roots, *Plant and Soil*, 97, 333–344, <https://doi.org/10.1007/BF02383223>, 1987.
- van Genuchten, M. T.: A Closed-form Equation for Predicting the Hydraulic Conductivity of Unsaturated Soils, *Soil Science Society of America Journal*, 44, 892–898, <https://doi.org/10.2136/sssaj1980.03615995004400050002x>, 1980.
- Van Rossum, G. and Drake Jr, F. L.: Python tutorial, Centrum voor Wiskunde en Informatica Amsterdam, The Netherlands, 1995.
- 1415 Verbančič, J., Lunn, J. E., Stitt, M., and Persson, S.: Carbon Supply and the Regulation of Cell Wall Synthesis, *Molecular Plant*, 11, 75–94, <https://doi.org/10.1016/j.molp.2017.10.004>, 2018.
- Wang, G., Li, W., Wang, K., and Huang, W.: Uncertainty quantification of the soil moisture response functions for microbial dormancy and resuscitation, *Soil Biology and Biochemistry*, 160, <https://doi.org/10.1016/j.soilbio.2021.108337>, 2021.
- Wang, J., Bogen, H. R., Vereecken, H., and Brüggemann, N.: Characterizing Redox Potential Effects on Greenhouse Gas Emissions Induced by Water-Level Changes, *Vadose Zone Journal*, 17, <https://doi.org/10.2136/vzj2017.08.0152>, 2018.
- 1420 Wiesenbauer, J., König, A., Gorka, S., Marchand, L., Nunan, N., Kitzler, B., Inselsbacher, E., and Kaiser, C.: A pulse of simulated root exudation alters the composition and temporal dynamics of microbial metabolites in its immediate vicinity, *Soil Biology and Biochemistry*, 189, <https://doi.org/10.1016/j.soilbio.2023.109259>, 2024.



1425 Zhou, X.-R., Schnepf, A., Vanderborght, J., Leitner, D., Lacointe, A., Vereecken, H., and Lobet, G.: CPlantBox, a whole-plant modelling
framework for the simulation of water- and carbon-related processes, in *silico Plants*, 2, <https://doi.org/10.1093/insilicoplants/diaa001>,
2020.